AD-A225 086

DTIC FILE COPY

Center for Night Vision and Electro-Optics

CONTRACT NUMBER

DAAB07-87-C-F094

REPORT NUMBER

NV-90-14

Title: Two-Photon Absorption Characterization of HgCdTe

Author(s): Professor Chris L. Littler

Address: University of North Texas

Type of Report (Final, Interim, etc.): Final

Date: 7/90

DTIC
ELECTE
AUG 0 8 1990
S B D

FORT BELVOIR, VA 22060-5677

DISTRIBUTION STATEMENT A
Approved for public release;
Distribution Unlimited

Unclassified
SECURITY CLASSIFICATION OF THIS PAGE

REPORT DOCUMENTATION PAGE

Form Approved OMB No 0704-0188

1a. REPORT SECURITY CLASSIFICATION Unclassified	1b. RESTRICTIVE MARKINGS
2a. SECURITY CLASSIFICATION AUTHORITY	3. DISTRIBUTION/AVAILABILITY OF REPORT Approved for public release: Distribution is Unlimited
2b. DECLASSIFICATION/DOWNGRADING SCHEDULE	
4. PERFORMING ORGANIZATION REPORT NUMBER(S) NA	5. MONITORING ORGANIZATION REPORT NUMBER(S) NA
6a. NAME OF PERFORMING ORGANIZATION Univ. of North Texas 6b. OFFICE SYMBOL (If applicable)	7a. NAME OF MONITORING ORGANIZATION Center for Night Vision and Electro-Optics
6c. ADDRESS (City, State, and ZIP Code)	7b. ADDRESS (City, State, and ZIP Code) ATTN: AMSEL-RD-NV-IRT Fort Belvoir, VA 22060-5677
8a. NAME OF FUNDING/SPONSORING ORGANIZATION CNVEO 8b. OFFICE SYMBOL (If applicable) AMSEL-RD-NV-IT	9. PROCUREMENT INSTRUMENT IDENTIFICATION NUMBER DAAB07-87-C-F094
8c. ADDRESS (City, State, and ZIP Code) Fort Belvoir, VA 22060-5677	10. SOURCE OF FUNDING NUMBERS PROGRAM ELEMENT NO. 661102A; PROJECT NO. 1L16110 2A31B; TASK NO HO; WORK UNIT ACCESSION NO. 007-CJ

11. TITLE (Include Security Classification)
~~Two Photon Characterization~~ See Cover

12. PERSONAL AUTHOR(S)
Chris Littler

13a. TYPE OF REPORT	13b. TIME COVERED	14. DATE OF REPORT (Year, Month, Day)	15. PAGE COUNT
Final	FROM 8/87 TO 6/90	90/7/30	101

16. SUPPLEMENTARY NOTATION

17. COSATI CODES			18. SUBJECT TERMS (~~Continue on reverse if necessary and identify by block number~~)
FIELD	GROUP	SUB-GROUP	Defect characterization, Magneto-Optical measurements, Two Photon Spectroscopy, Narrow band gap semiconductors, ~~II-VI compounds~~.
17	05		

19. ABSTRACT (Continue on reverse if necessary and identify by block number)

Magneto-Optical measurements of $Hg_{1-x}Cd_xTe$ alloys have provided a new means of studying impurities and defects in this important II-VI material. Two-photon magnetoabsorption (TMPA) has been used to accurately determine the temperature dependence of the energy gap of various HgCdTe alloys, revealing behavior that deviates from currently accepted models. In addition, magneto-optical techniques have been used to detect the presence of both shallow and deep impurities/defects and accurately determine their activation energies, thus providing information necessary for understanding the electrical and optical properties of the material.

20. DISTRIBUTION/AVAILABILITY OF ABSTRACT ☐ UNCLASSIFIED/UNLIMITED ☒ SAME AS RPT. ☐ DTIC USERS	21. ABSTRACT SECURITY CLASSIFICATION Unclassified	
22a. NAME OF RESPONSIBLE INDIVIDUAL Frederick F. Carlson	22b. TELEPHONE (Include Area Code) 703-664-5036	22c. OFFICE SYMBOL AMSEL-RD-NV-IT

DD Form 1473, JUN 86 Previous editions are obsolete.

SECURITY CLASSIFICATION OF THIS PAGE
Unclassified

Final Report

August 28, 1987 - June 27, 1990

Contract DAAB07-87-C-FO94

With the U.S. Army CECOM Center for Night Vision and Electro-Optics

Fort Belvoir, Virginia 22060-5677

Contract Monitor: Mr. Fred Carlson

"Two-Photon Absorption Characterization"

Principal Investigators:

Dr. Chris L. Littler

Dr. David G. Seiler

Department of Physics

University of North Texas

Denton Texas, 76203

The views, opinions, and/or findings contained in this report are those of the authors and should not be construed as an official Department of the Army position, policy, or decision, unless designated by other documentation.

TWO-PHOTON ABSORPTION CHARACTERIZATION OF HgCdTe

I. Summary of Program Goals 4

II. Discussion of Tasks

Task (a). Experimental Facility 5

Task (b). Investigation of Two-Photon Absorption 5

Task (c). Identification of Impurity Levels 36

Task (d) Investigation of Time-Resolved Behavior 50

Task (e) Investigation of Lifetimes 50

Other Areas Phonon-Assisted Magneto-Optical Effects 58

QUALITY INSPECTED 4

Availability Codes
Dist | Avail and/or Special
A-1

III. **References** 62

IV. **Tables** 65

V. **Appendix** 70

Final Report

August 28, 1988 - June 27, 1990

Contract DAAB07-87-C-FO94

"Two-Photon Absorption Characterization"

Principal Investigators:

Dr. Chris L. Littler

Dr. David G. Seiler

University of North Texas

The principal goal of the program was to develop two-photon absorption spectroscopy (TPAS) as a tool for characterizing HgCdTe, to identify impurity and defect levels in the forbidden energy gap of HgCdTe, and determine the effect of these impurities on the lifetime of minority carriers by the use of time-resolved spectroscopic studies. The specific tasks that were performed from section 3.0 of the statement of work are:

a. Build an experimental facility specifically designed for the characterization of HgCdTe, with special emphasis given to infrared laser systems, variable low temperature apparatus, and high magnetic fields.

b. Investigate TPAS at energies below the bandgap for HgCdTe and identify all observable sub-band gap energy levels.

c. Identify impurity related energy levels and correlate with specific impurities.

d. Investigate the time-resolved behavior of HgCdTe to two-photon absorption excitation. Use information obtained to estimate the "generic lifetime" of the charge carriers.

e. Analyze "lifetime" data to determine surface and bulk recombination

probabilities.

As a result of this program significant results were obtained in each task. Specifically, the highlights of the program are summarized by task as follows:

Task (a) An experimental facility specifically designed to study HgCdTe has been completed and is fully operational. A schematic diagram of the experimental layout is detailed in Figure 1. The specific equipment purchased and installed during the first year were: an Apollo model 150 CO_2 laser, an Apollo model 125 far infrared laser system, and a 120 kG superconducting solenoid mounted in a Janis 16CNDT supervaritemp dewar. The solenoid has magnetic field modulation coils capable of producing AC magnetic fields of ± 500 gauss peak-to-peak. The CO_2 laser is grating tunable and is capable of producing continuous wave powers greater than 100 watts for any of the available laser frequencies. The laser can be operated in any one of four modes: continuous wave, electronically pulsed, electronically chopped, and Q-switched. The variable temperature cryostat containing the superconducting solenoid is capable of producing sample temperatures between 1.8 K and 300 K, controllable to ± 0.5K.

Sample holders for the low temperature cryostat have been designed to allow for rapid sample change and cooldown. The sample is mounted in an integrated circuit chip carrier which is non-magnetic and mates to a socket permanently attached to the sample holder. A detailed description of the carrier is shown in Figure 2. Twelve leads are available to bring out the sample signals. This flexibility permits the measurement of several samples during a single low temperature run.

During the first quarter of the program, all features of the UNT Infrared Laser and High Magnetic Field Facility were put into working order. The magnetic field modulation coils were tested by studying the Shubnikov de-Haas effect in a number of different samples: (1) GaSb, (2) MBE-grown HgTe, and (3) superlattices of HgCdTe. The results of the HgTe study were reported at the 1987 U. S. Workshop on the Physics and Chemistry of HgCdTe and in the two published articles[1,2].

Task (b) Two-photon magnetoabsorption (TPMA) spectra have been obtained for the first

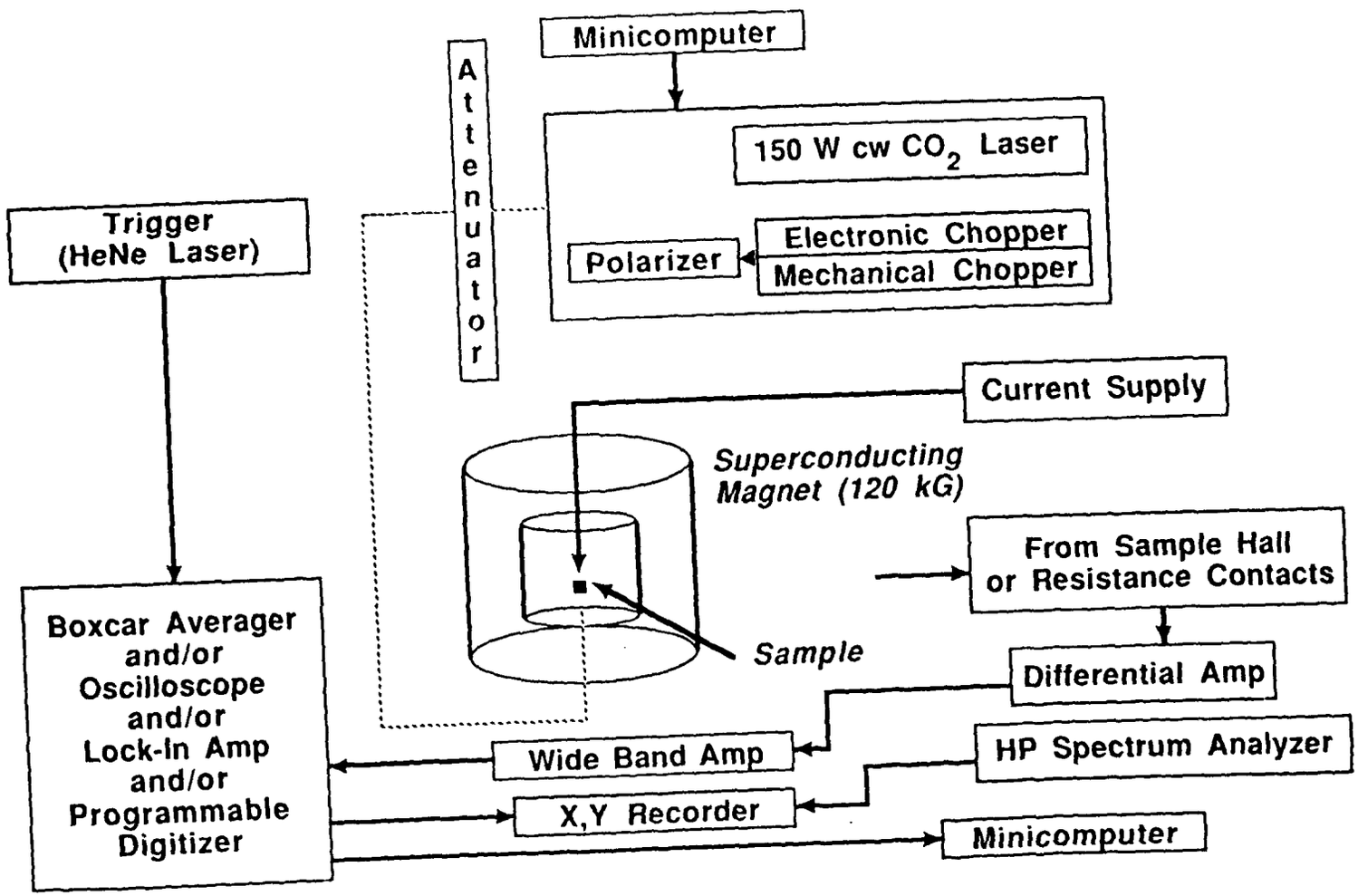

Figure 1. Schematic diagram of experimental apparatus.

University of North Texas
High Magnetic Field Facility

Sample Holder

AUGAT type 528-AG10D PC terminal connector cut in half

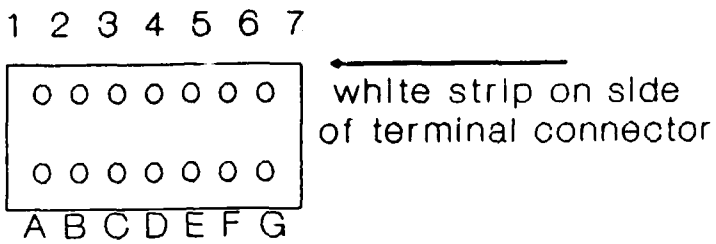

Dimensions: 1" by 1" diagonal

SAMPLE CONFIGURATIONS:

Sample connections	Use contact pair
current	(1&7) or (A&G)
resistivity	(2&6) or (B&F)
resistivity (2nd pair)	(3&5) or (C&E)
Hall	(2&B) or (3&C) or (5&E) or (6&F)

no contacts on 4 and D

Figure 2: Sample Holder Diagram

time for samples of p- and n-type HgCdTe. A variety of samples with x-values between 0.20 and 0.31 were studied and the results analyzed to extract the energy band structure and temperature dependence of the energy gap of HgCdTe. Detailed information on the samples studied during this program is given in Table I. Figure 3 shows typical TPMA spectra (high field region) obtained as a function of laser wavelength for sample #4, along with one-photon (OPMA) and impurity (IMO) data seen at lower magnetic fields. The two strong TPMA peaks seen here between 80 kG and 120 kG have also been observed in every sample of HgCdTe with $x \geq 0.23$ studied and are identified as the two photon transitions denoted by L1 and L2 in Table II. Theoretical calculations of transition energies versus magnetic field are shown in Figure 4 for each of the magneto-optical effects mentioned above. The magnetic field induced or Landau level energies were calculated using a modified Pidgeon-Brown (P-B) energy band model and the following set of energy band parameters[3]: E_p = 19 eV, Δ = 1.0 eV, γ_1 = 3.3, γ_2 = 0.1, γ_3 = 0.9, κ = -0.8, F = -0.8, q = 0.0, and N_1 = 0.0, and the appropriate one- or two-photon selection rules. The value of the energy gap (E_g) was determined by fitting the theoretical energies to the OPMA and TPMA data using E_g as an adjustable parameter. The transition energy for TPMA are given by

$$2\hbar\omega = E_c^{a,b}(n_c, B) - E_v^{a,b}(n_v, B) \tag{1}$$

where $\hbar\omega$ is the photon energy of the laser, $E_c^{a,b}(n_c, B)$ represents the energies of the conduction band Landau Levels of spin state a or b, $E_v^{a,b}(n_v, B)$ represents the energies of the valence band Landau levels, n is the Landau quantum number, B is the magnetic field, and the zero of energy is defined at the top of the valence band. For a consistent description of both the OPMA and TMPA data, an exciton binding energy correction was added to the OPMA data. The TPMA selection rule dependence was tested by obtaining TPMA spectra using left circularly (σ_L) and right circularly polarized (σ_R) laser light. An example of the spectra is shown in Figure 5. According to second order perturbation theory, two-photon absorption transition probablities are proportional to the product of two matrix elements. In the "intra-interband" transition picture, one matrix element

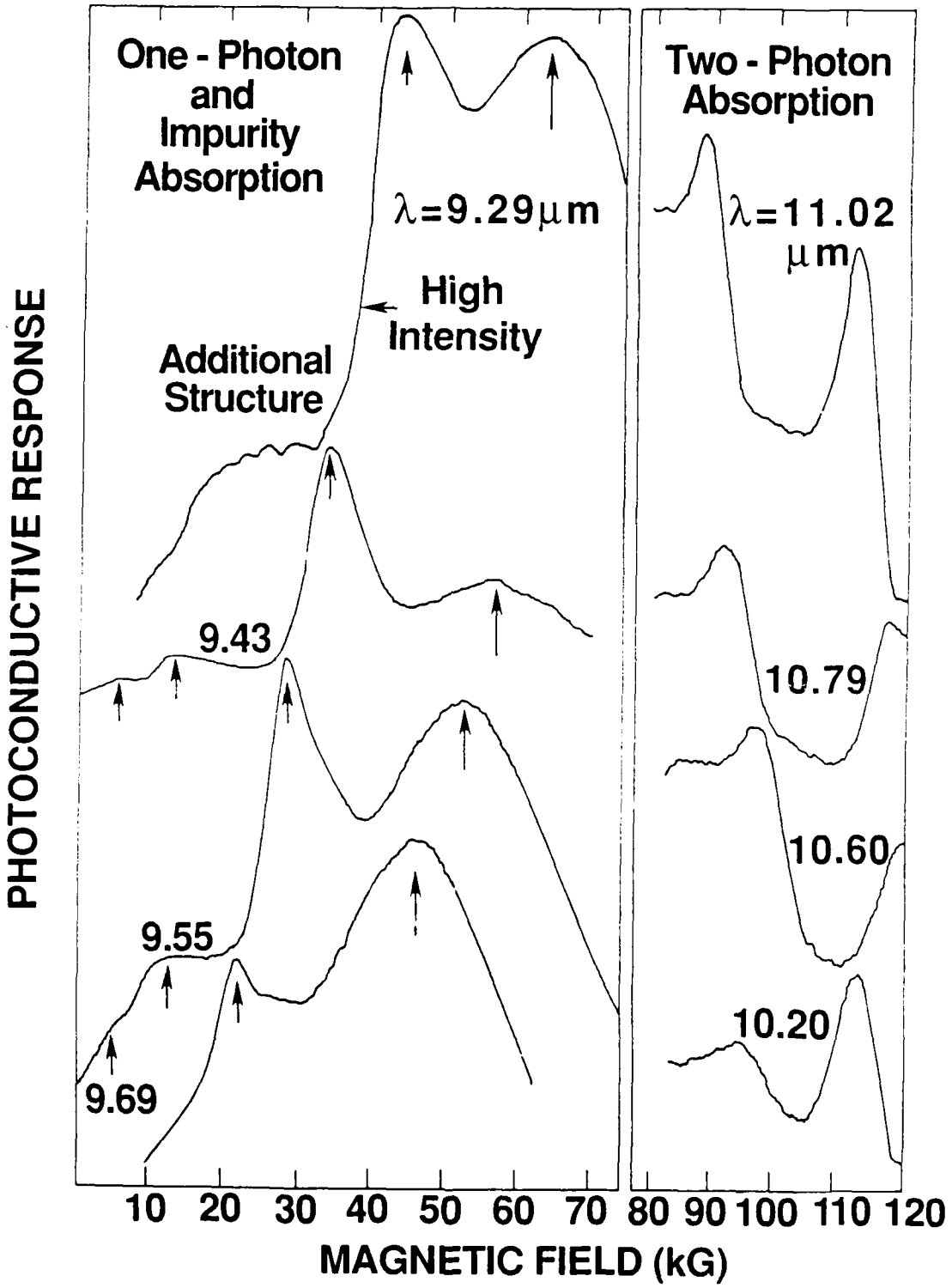

Figure 3. Magneto-Optical spectra at various CO_2 laser wavelengths for sample #4.

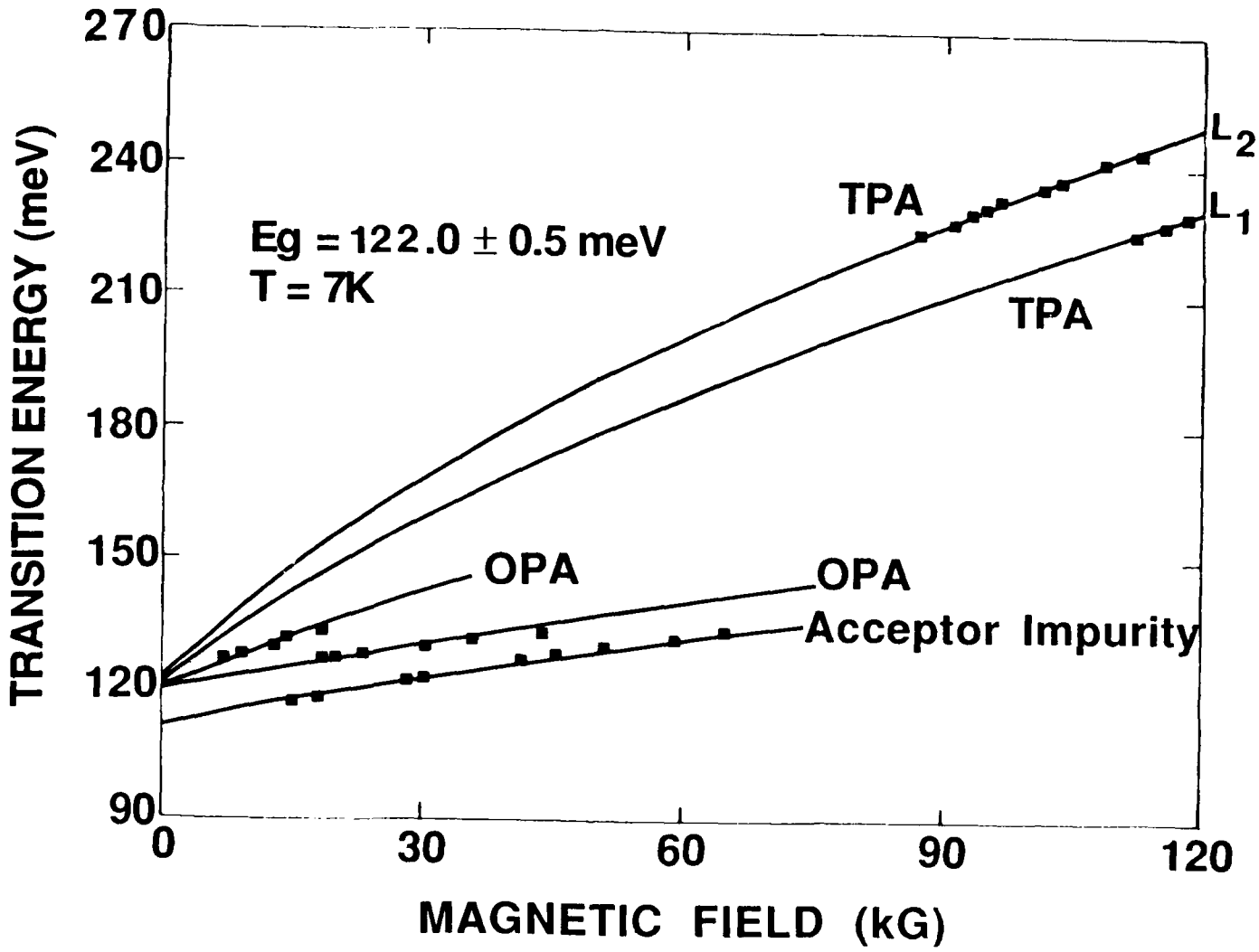

Figure 4. Transition Energy versus Magnetic field showing one-photon absorption (OPA), two-photon absorption (TPA), and acceptor impurity absorption behavior for sample #4.

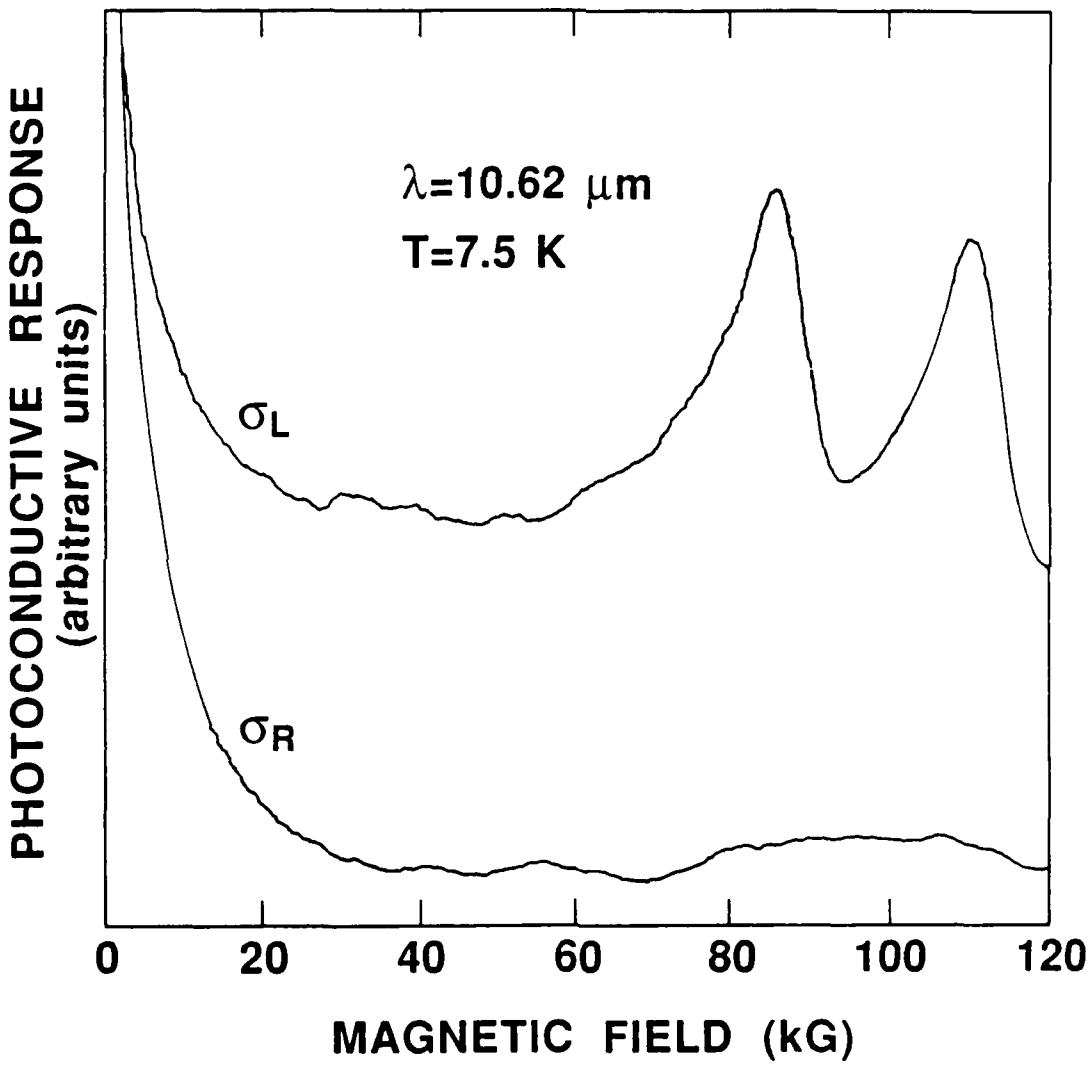

Figure 5. Polarization dependence of TMPA spectra.

represents an intraband transition while the other represents an interband one. Thus, two-photon absorption is predicted to be strongest using σ_L polarized light since the controlling intraband transition is cyclotron resonance. It is seen in Figure 5 that the TPMA selection rule $\Delta n = +2$ for σ_L polarization is confirmed by the clear dependence of the TPMA spectra on polarization.

Finally, the broad peak (long arrows) observed on the high field side of the last OPMA peak is identified as an arising from electron transitions from a shallow acceptor to the lowest conduction band Landau level. Comparison of this IMO data with the theoretical predictions yields an acceptor binding energy of 9.8 meV. This energy is consistent with that for Cu acceptors in HgCdTe[4]. A major significance of this result is that IMO spectra provides a new means of detecting the presence of compensating acceptors in n-type material.

Figures 6, 8, 10, 11, and 12 show examples of TPMA spectra obtained for sample #7, #8, #9, #10 and #12, respectively. In each case the two strong TPMA resonances L1 and L2 are observed. In addition, samples #4, #6, and #11 show TPMA structure whose identification are given in Table II. Figures 7, 9, and 13 show the comparison of theoretical predictions to the TPMA data for samples #7, #8, and #12. In addition, a comparison for samples #4, #9 , #10, and #12 are shown in Figure 14, along with a summary of other results. In each case the TPMA data provides a very accurate measure of the energy gap of each sample. As a result, TPMA measurements have been used to investigate the temperature dependence of the energy gap of HgCdTe. Examples of the temperature dependence of the TPMA spectra are shown for sample #4 in Figure 15 and sample #8 in Figure 16. Also shown in Figure 15 is the temperature dependence of the OPMA spectra. The magnetic field positions of the two strong TPMA resonances are seen to be relatively independent of temperature between 2K and 15K, then shift to lower magnetic field at higher temperatures. The data was analyzed by calculating the TPMA transition energies using the Pidgeon-Brown model with E_g as the only parameter adjusted in order to fit the experimental data.

During this program, the results of two-photon magnetoabsorption in various alloys of HgCdTe were complied in order to determine an accurate relationship for the energy gap as a function of

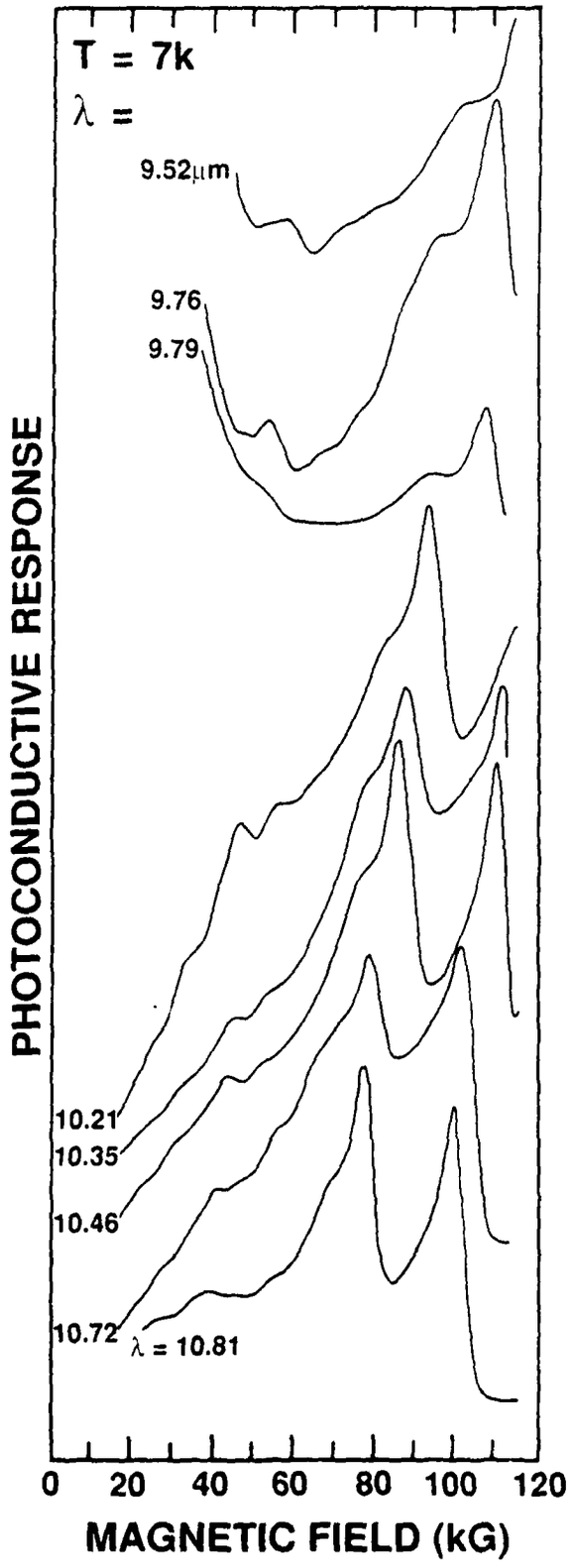

Figure 6. Wavelength dependence of the photoconductive response of sample #7.

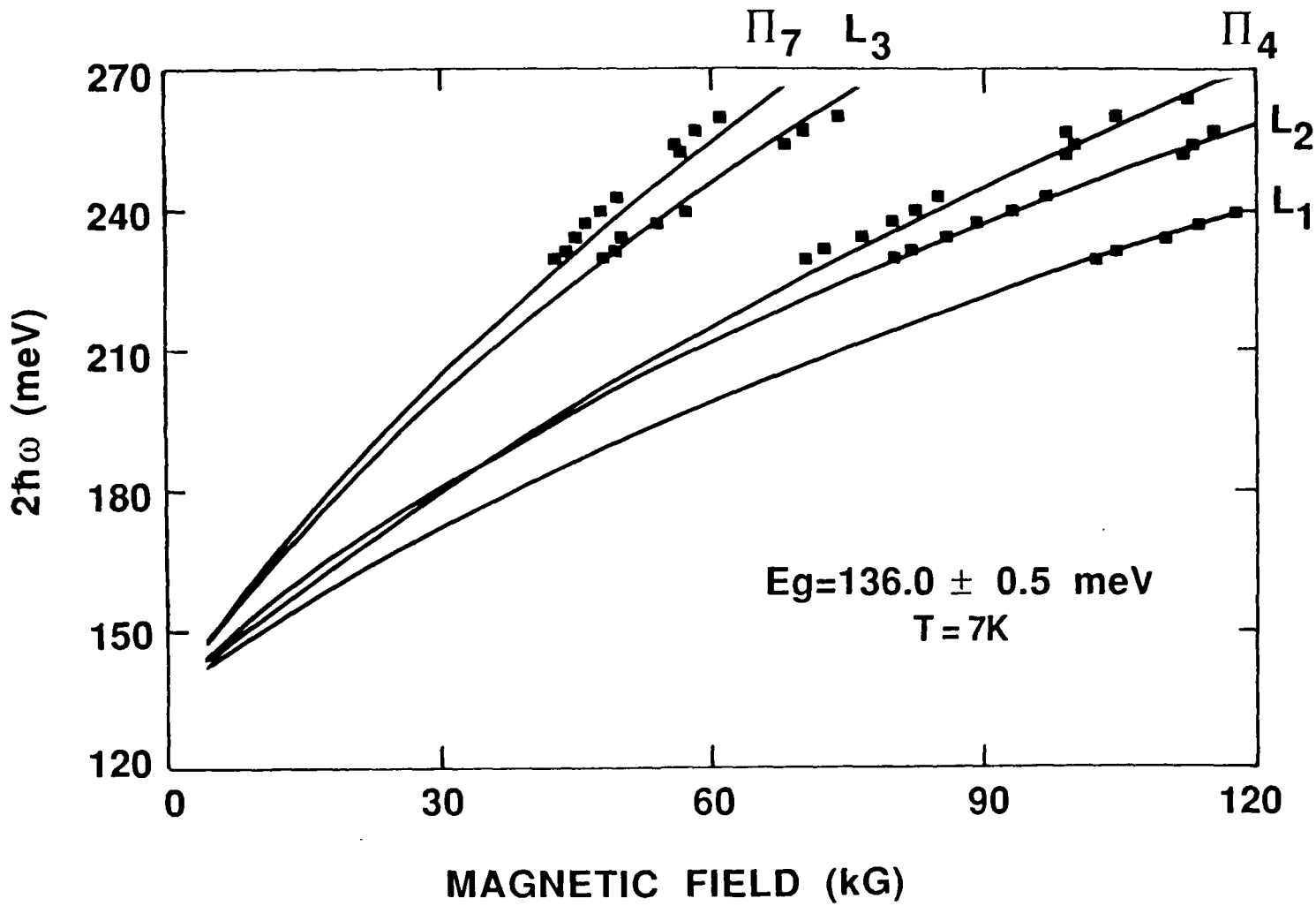

Figure 7. Transition Energy versus magnetic field for sample 7.

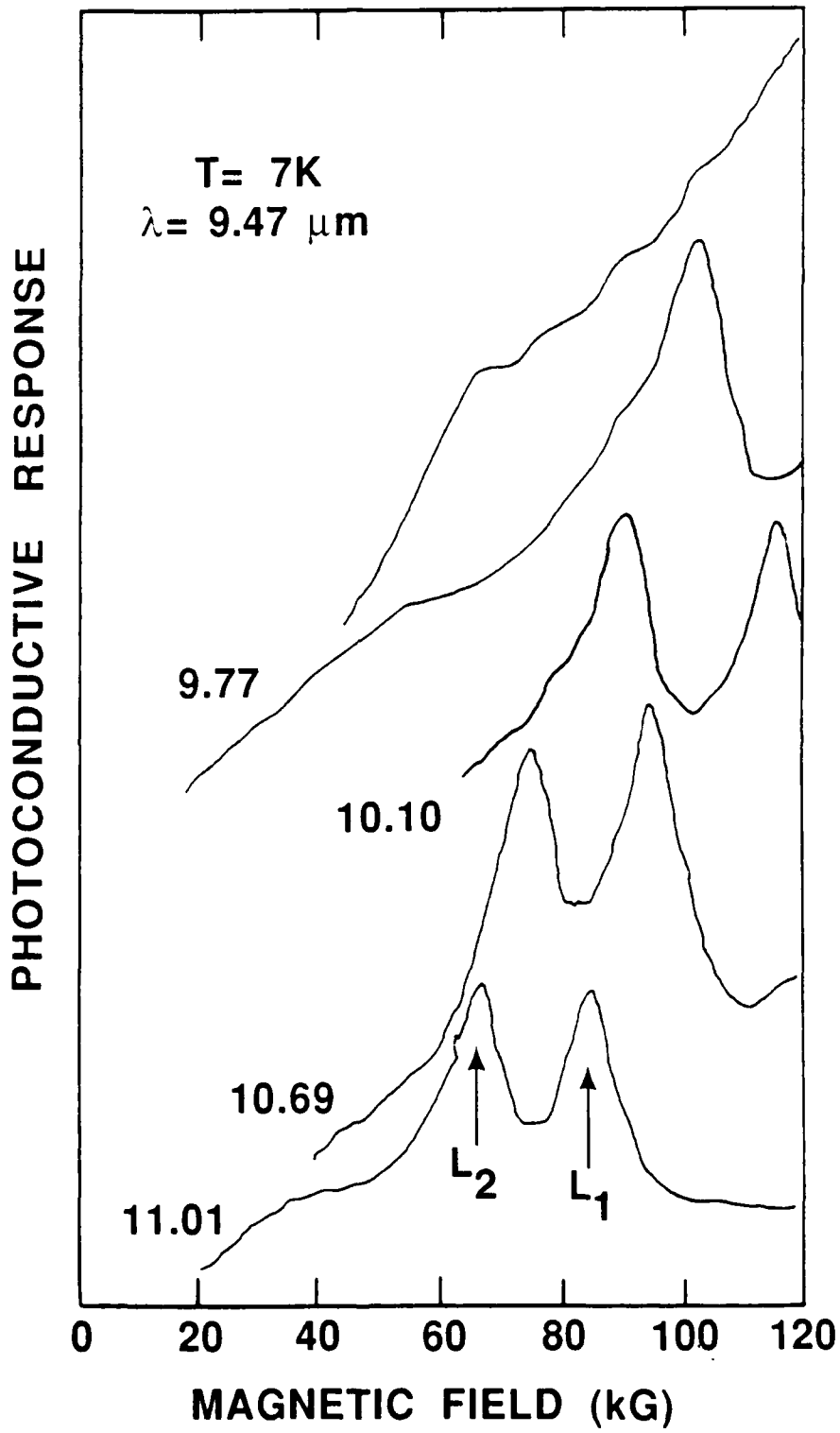

Figure 8. Wavelength dependence of photoconductive response for sample #8.

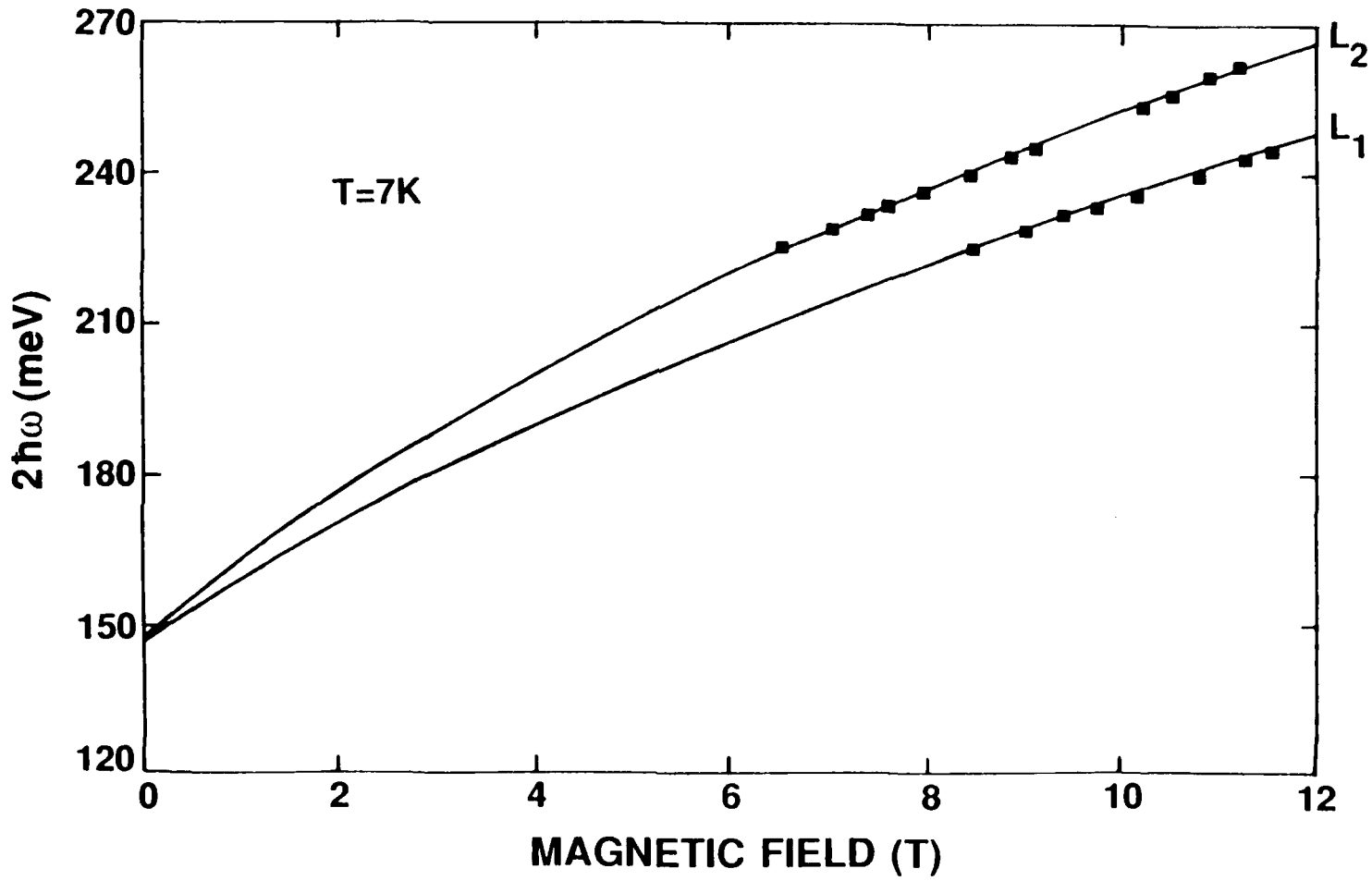

Figure 9. Transition energy vs. magnetic field for the TPMA spectra from the TI thm sample. The 7K energy gap from the fit of theory (solid lines) to data (solid boxes) is 146.5 meV.

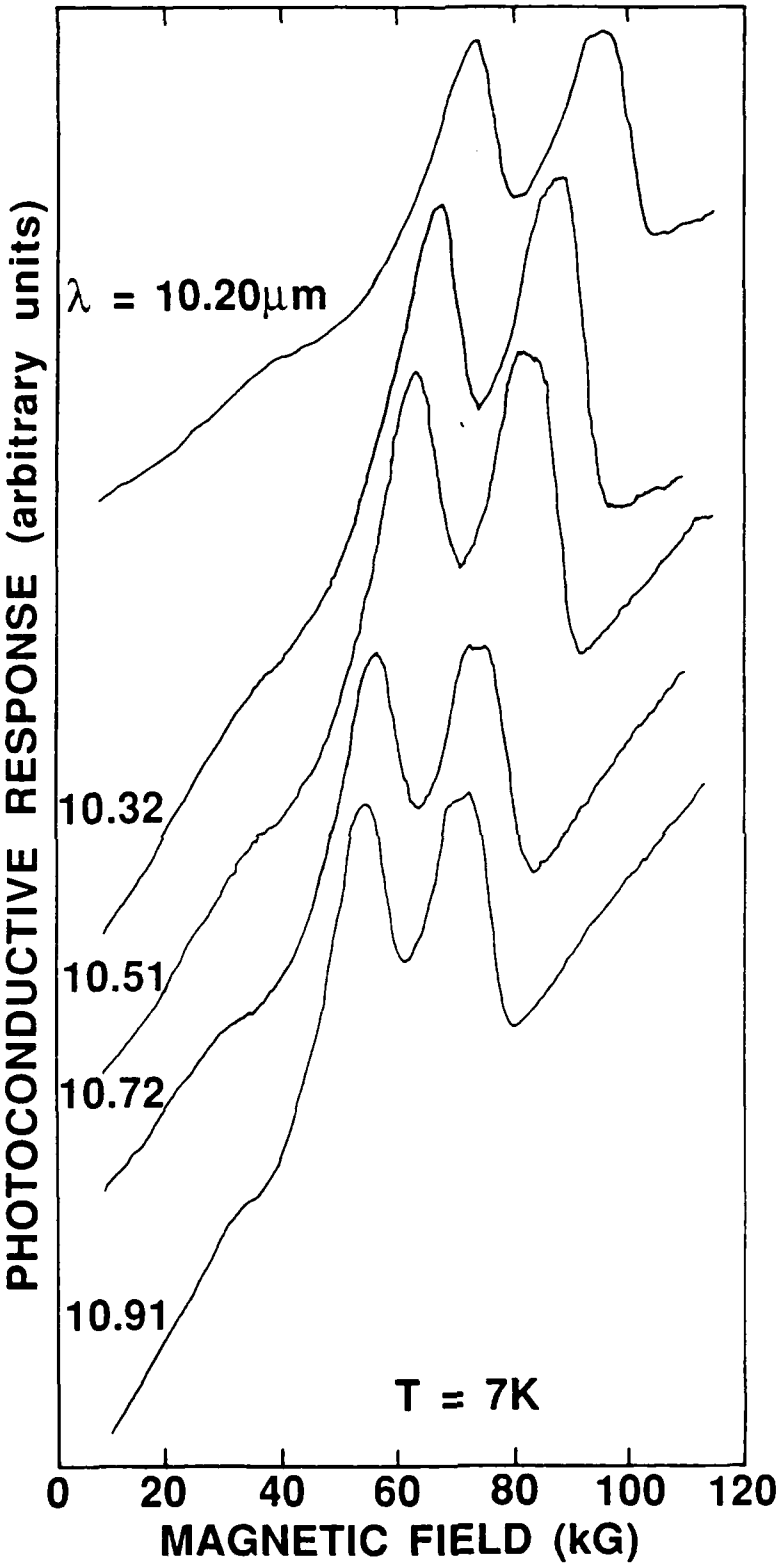

Figure 10. Photoconductive response vs. magnetic field for x = 0.26 sample. Note the two-photon absorption peaks.

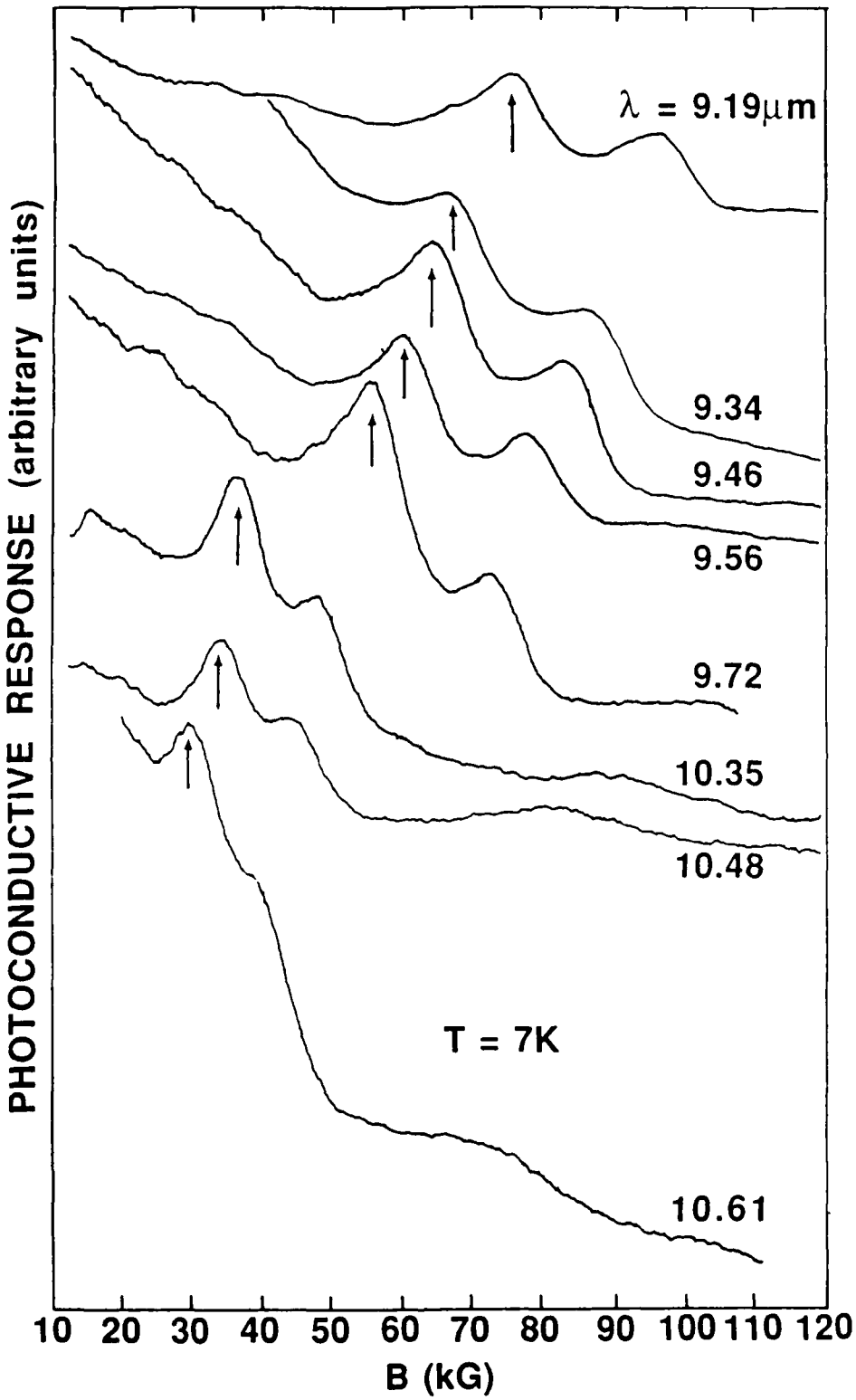

Figure 11. Photoconductive response vs. magnetic field for x = 0.278 sample. Note the two-photon absorption peaks.

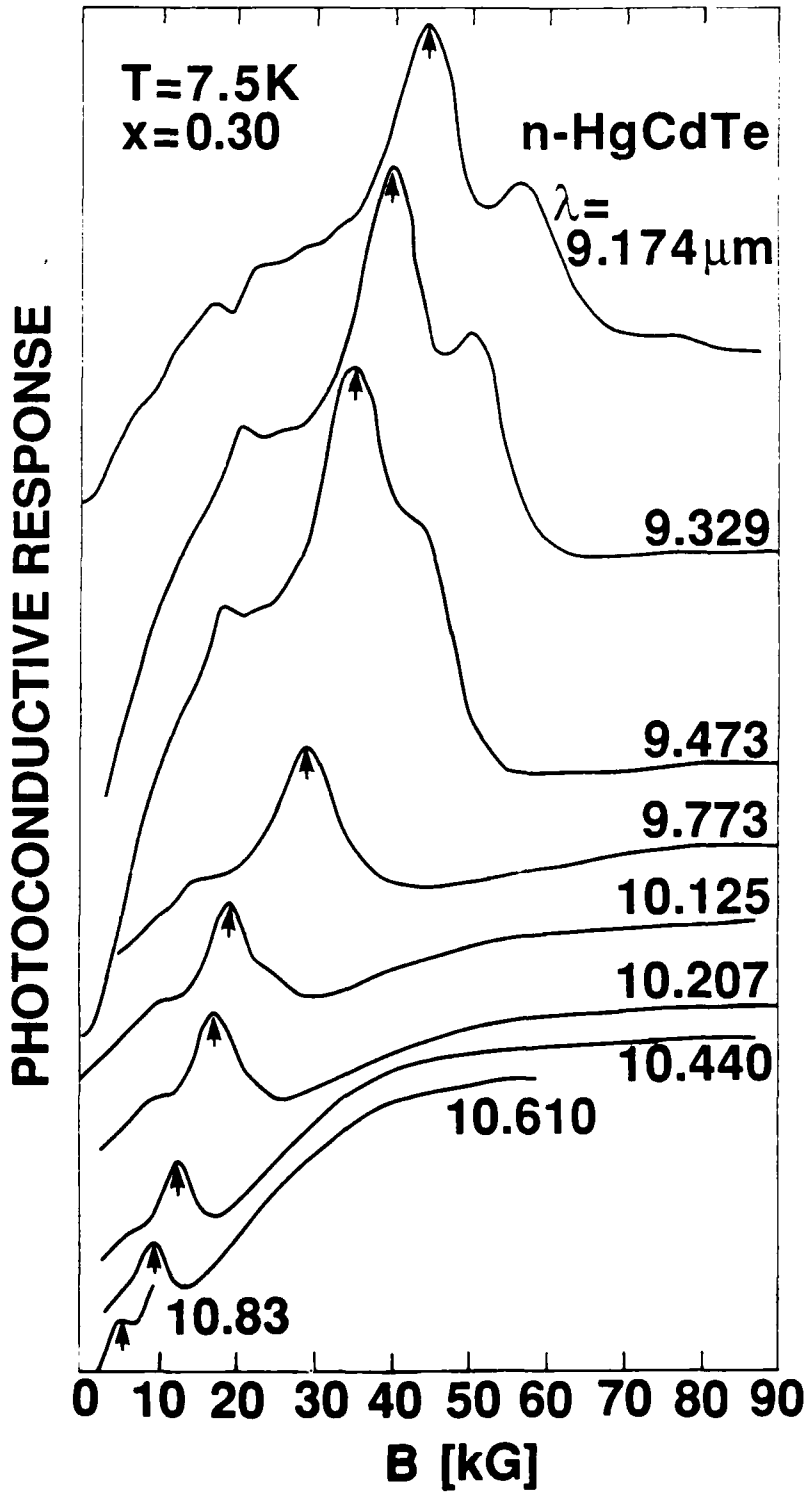

Figure 12. Wavelength dependence of the photoconductive response for sample #12.

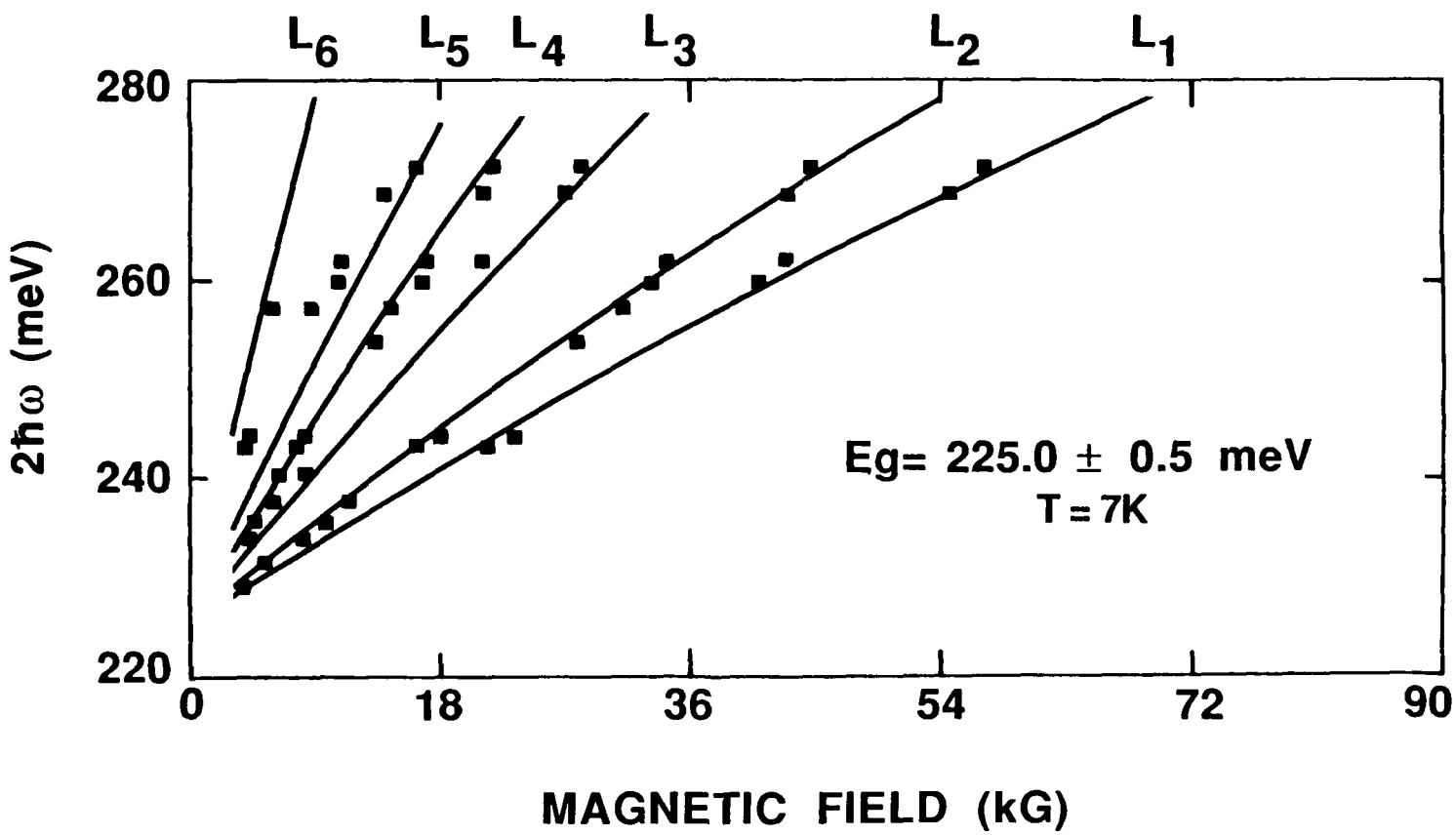

Figure 13. Transition energy versus magnetic field behavior for sample #12.

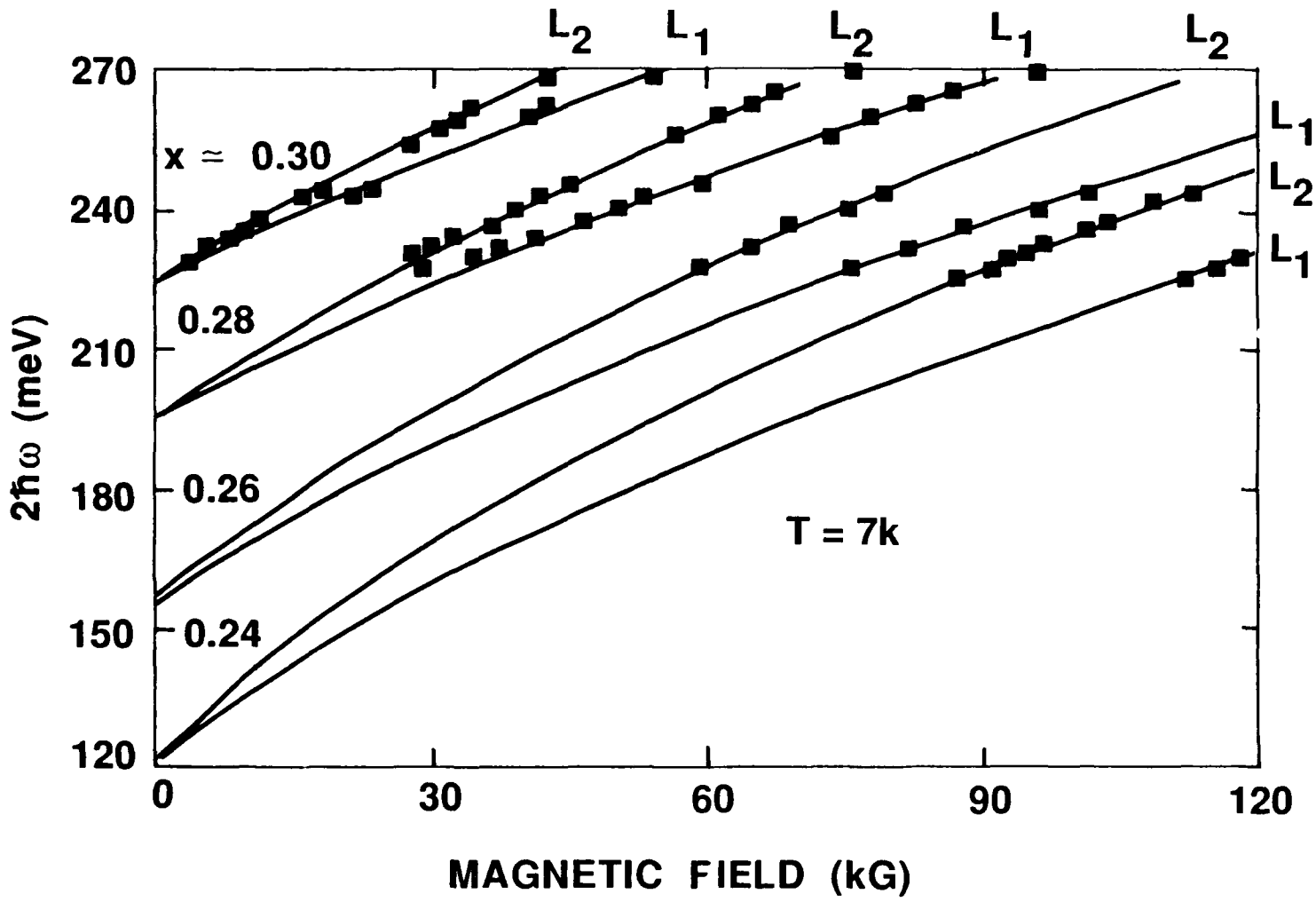

Figure 14. Fan chart plots of two-photon data for samples #4, #9, #10, and #12.

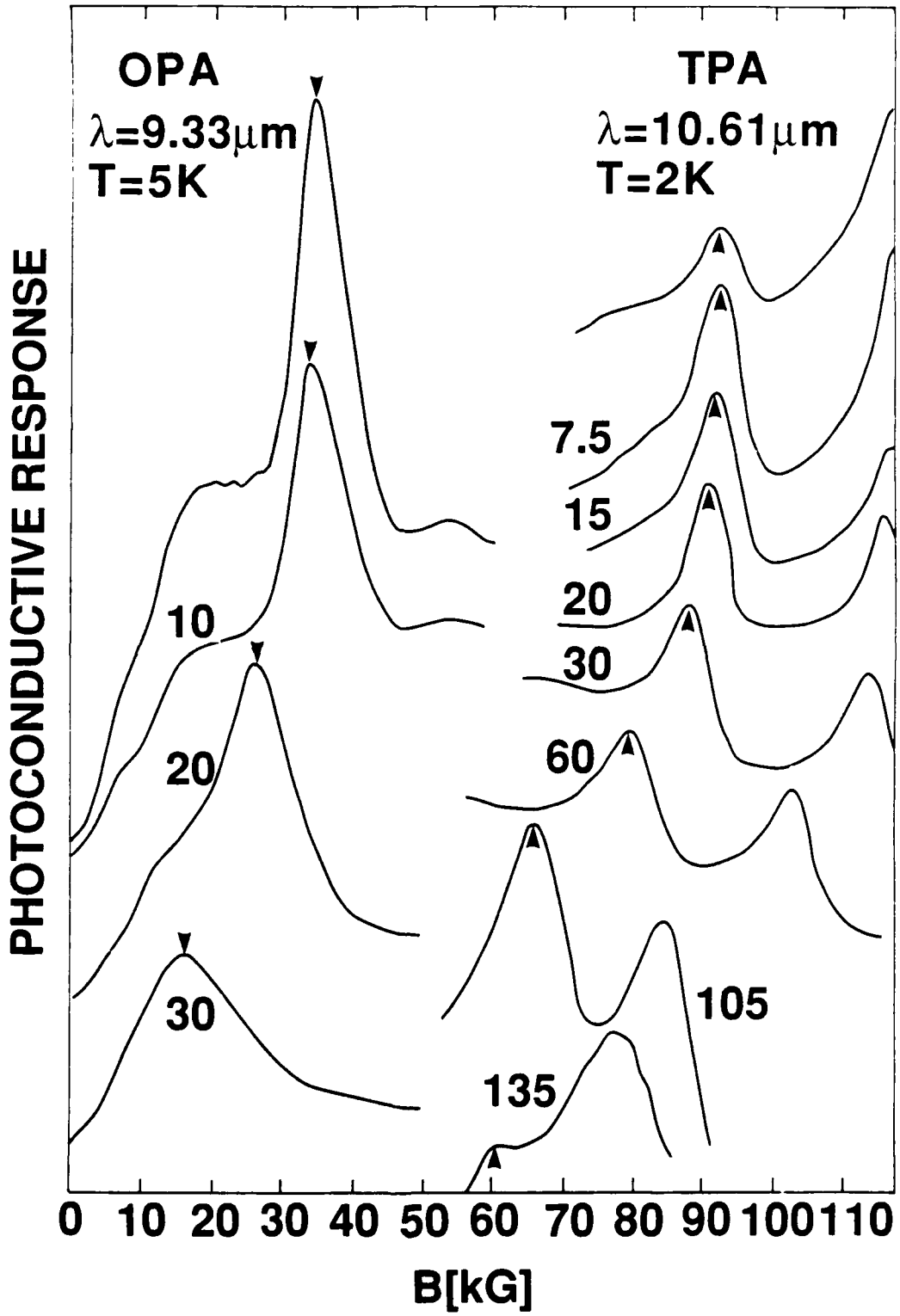

Figure 15. Temperature dependence of the OPA and TPA magneto-optical spectra for sample #4.

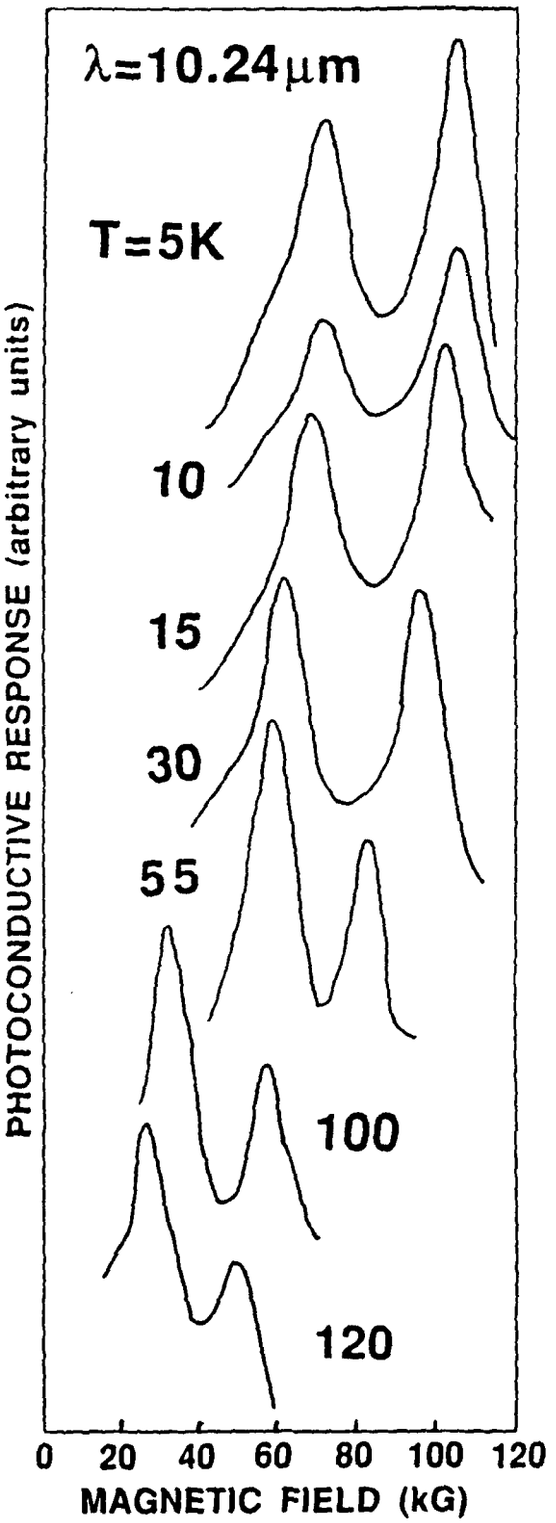

Figure 16. Temperature dependence of the photoconductive spectra for the TI THM sample.

temperature ($E_g(x,T)$). The most frequent methods for determining the MCT energy gap are usually based on either detector cut-off wavelength or optical absorption cut-on. However, the definition of the energy gap from these types of measurements is ambiguous. The absorption edge is not infinitely sharp because of free carrier and phonon absorption along with band tailing effects. An example of the variability of defining E_g from an optical absorption measurement is (1) using the photon energy value at which α = 500 cm^{-1} as opposed to (2) using the energy at the turning point where the sharply rising region of the absorption curve crosses the comparatively smooth region of intrinsic absorption (usually observed for α = 3000 to 4000 cm^{-1}. Photoluminescence experiments have also proven difficult to perform in the smaller band gap materials. The use of two-photon magnetoabsorption (TPMA) has provided a much more sensitive measure of E_g, revealing a nonlinear temperature dependence of E_g at temperatures below 40K. Through the use of TPMA measurements an empirical relationship that properly accounts for this nonlinear temperature dependence while still accurately describing the x dependence for $0 \leq x \leq 0.3$ has been obtained.

Figure 17 shows a plot of $E_g(x,T)$ for several sets of magneto-optically derived E_g values for very low temperatures (< 10 K), along with our TPMA-deduced values of E_g. Table III gives the values of E_g and x used in the graphs of Figs. 17 and 18 (Ref.s 5-10) along with the magneto-optical technique used to obtain them. The variations of two empirical relationships that represent the most extreme behavior also area shown in Fig. 17 by the solid lines (Weiler's[3] and the HSC relationship[11]). It is immediately clear that the biggest differences in these two relationships occur in the x = 0.2 - 0.3 region. Thus in order to test which relationship is most accurate, the magneto-optical data in the range 0.2 to 0.3 is replotted in Fig. 18. For completeness the variations of three additional empirical relationships that have also been reported in the literature: Nemirovsky and Finkman (NF)[12], Chu, Xu, and Tang (CXT)[13], and Legros and Triboulet (LT)[14] have also been included. In addition two values from the recent EMIS Datareviews Series No. 3[15] have been added. The Schmit and Stelzer[16] relationship was not included because the low value of E_g (-250 meV) obtained from it at x = 0 are in disagreement with the low x-value MCT data of Guldner et al.[5,6] and the HgTe results from

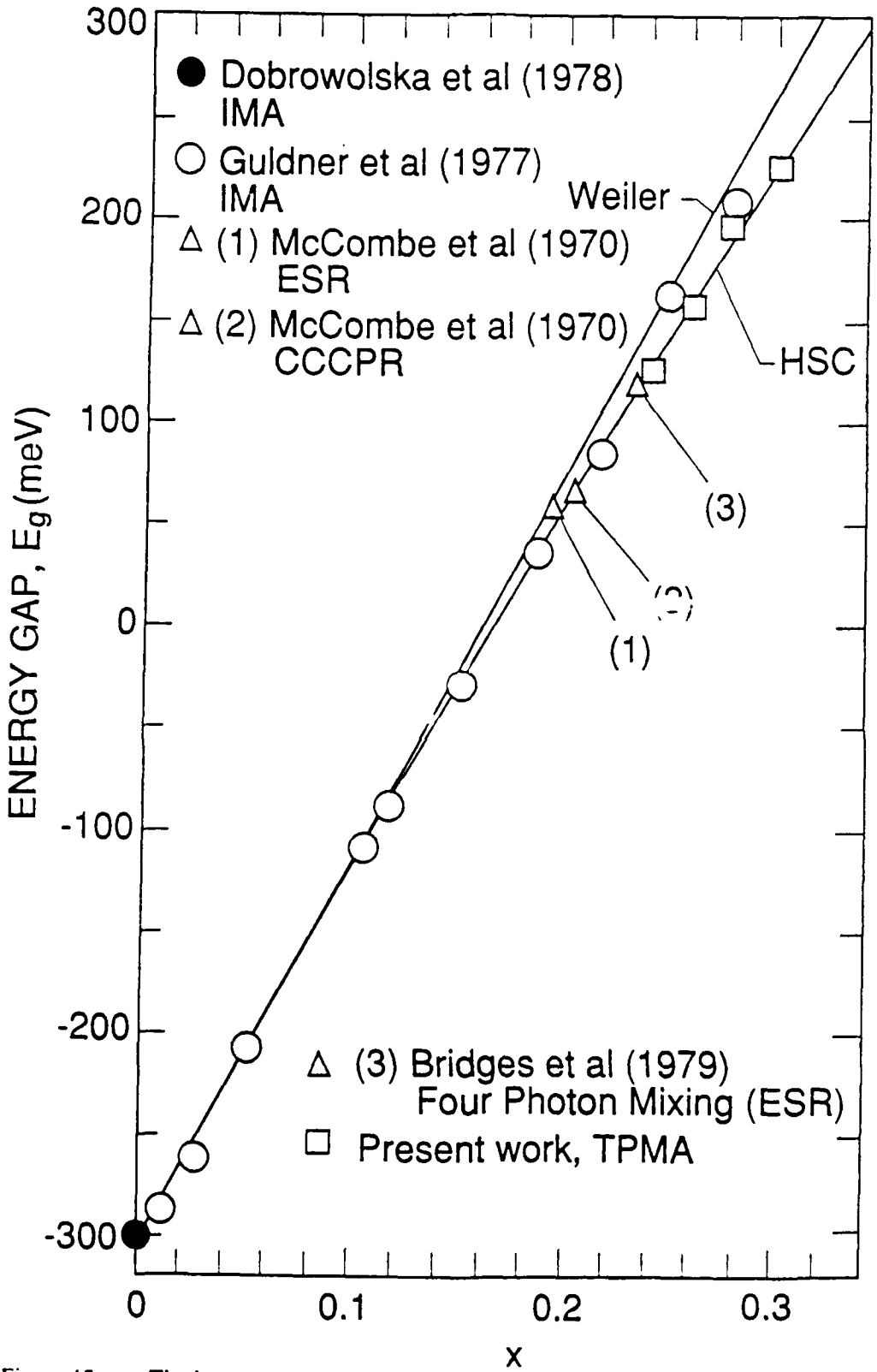

Figure 17. The low-temperature ($\simeq$ 4 K) x-dependence of the energy gap for alloys with $0 \leq x \leq 0.3$. Selected magneto-optical data are presented as identified by the various symbols. The two solid lines represent extremes of the published $E_g(x,T)$ relationship: Weiler (Ref. 3) and HSC (Hansen, Schmit, Casselman, Ref. 11).

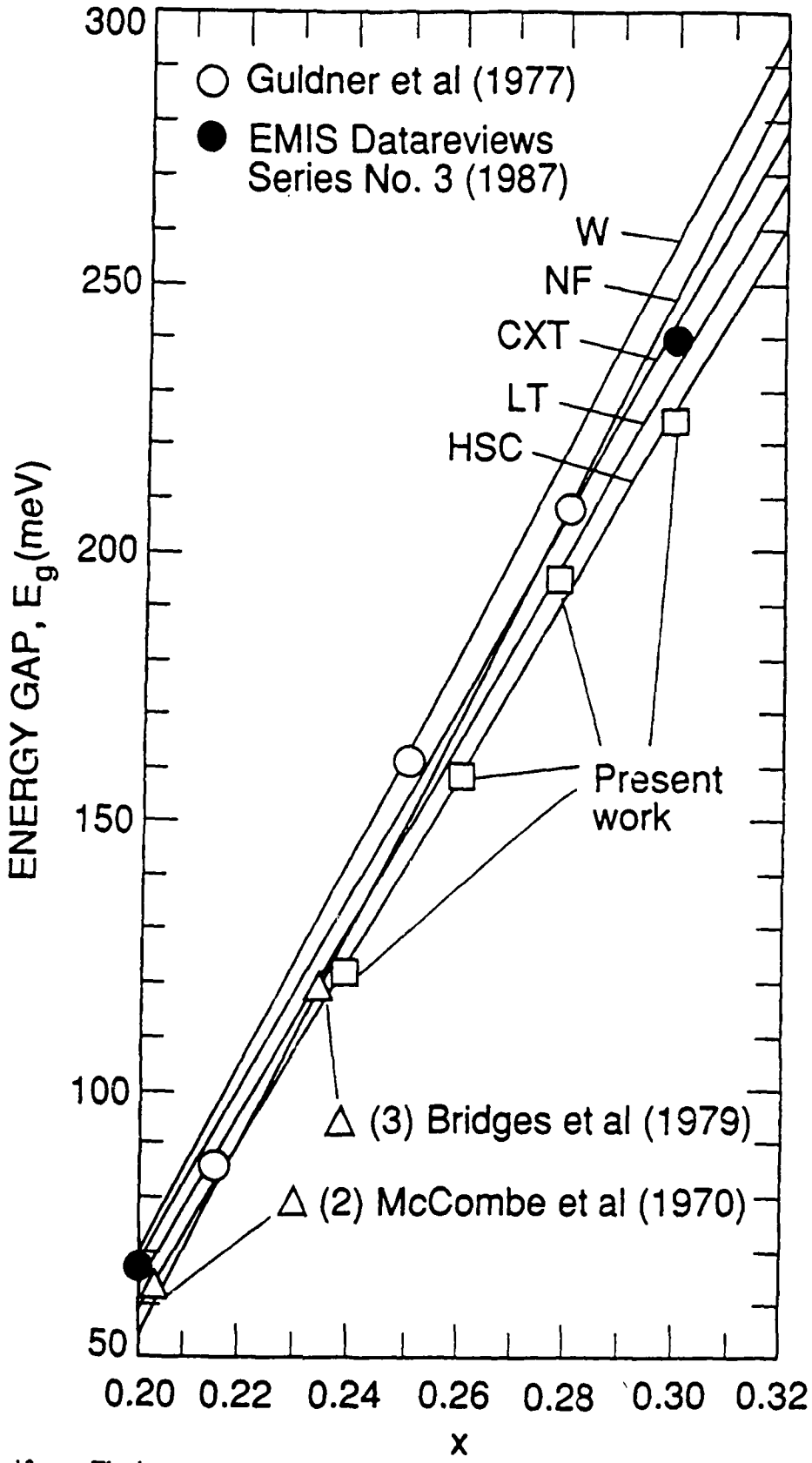

Figure 18. The low-temperature x-dependence of the energy gap for $0.2 \leq x \leq 0.3$. The symbols represent published magneto-optical data and the solid lines published relationships describing $E_g(x,T)$: W[3], NF[12], CXT[13], LT[14], and HSC[11].

Dobrowolska et al.[7] The extremely wide variation in predicted E_g values from these relationships is apparent. The important observation to note is that the present TPMA work verifies the use of the HSC relationship as representing the best value of $E_g(x,T)$ in the range 0.0 to 0.3 at very low temperatures (< 10 K).

Most workers have ignored the fact the $E_g(T)$ should vary nonlinearly with T at low temperatures (see the thermodynamic arguments presented later). Until this study, accurate low temperature $E_g(T)$ data simply did not exist. Figure 16 shows how the TPMA spectra obtained at λ = 10.24 μm depend upon lattice temperature T. A shift in magnetic field positions of the resonant L_1 and L_2 structure is seen to be small for $T \leq 15$ K, but quite noticeable for $T > 15$ K. The shift of the resonant structure to lower magnetic fields for increasing temperatures is a direct consequence of the increasing energy gap, since as E_g becomes larger, the valence- and conduction-band Landau levels become further apart in energy. Thus, smaller values of magnetic field are required to meet the TPMA resonant condition for a given two-photon energy. At each temperature, multiple wavelengths were then used to determine values of E_g.

In order to describe the temperature dependence of E_g, the linear temperature term T in the Hansen-Schmit-Casselman relation has been replaced by the term $\frac{A+T^3}{B+T^2}$. This yields the following expression:

$$E_g(x,T) = -0.302 + 1.93x + 5.35(1-2x)(10^{-4})\left[\frac{A + T^3}{B + T^2}\right] - 0.810x^2 + 0.832x^3. \qquad (2)$$

This functional relationship agrees with the HSC relationship at high temperatures, while allowing for an offset from the HSC relationship at 0 K. It also agrees with the fact that $dE_g/dT = 0$ at 0 K. The size of the 0 K offset is determined by A/B, while the temperature above which agreement with HSC occurs is determined from the inequalities $T \gg \sqrt[3]{A}$ and $T \gg \sqrt{B}$. A composite of three sets of E_g versus T data for the samples with x = 0.239, x = 0.253, and x = 0.2595 have been fitted simultaneously by a nonlinear least squares routine. The first and third values were obtained from

Cominco, while the second was chosen to be consistent with the HSC relationship at high temperatures. The data merge smoothly with the HSC relationship above 100 K. Below 100 K the data lie below the HSC relationship, and become constant before 10 K. Figure 19 shows the composite data rationalized for comparison by subtracting the 0 K energy gap obtained from HSC and dividing by 0.535 (1-2x). Rationalized HSC values are used at high temperature so that a fit was obtained between 0 and 300 K. Figure 20 shows an expansion of Figure 19 for T = 0 to 100 K. The constants A and B that best fit all the data are: A = -1822 K^3 and B = 255.2 K^2. Although A and B can vary with x, no trend was observed by fitting the data individually for each sample, and these A and B values provide a best fit to all of the data. The offsets between our fit and HSC at 0 K are on the order of 2 meV, which is comparable to the value implied by the uncertainty in x values. Even though at 0 K the offsets are small, the differences predicted by the new relationship and associated with the nonlinear temperature dependence of E_g are on the order of 3 to 4 meV at 15 K and should be taken into account in experiments requiring high accuracy.

Figures 21, 22, and 23 show the data for the energy gap as a function of temperature for each sample along with the result of the composite fit. In each case the fit is adequate relative to the $\simeq$ 2 meV uncertainty that arises mainly from the uncertainty in x. Figure 24 shows dE_g/dT, rationalized as in Fig. 19, determined from the data as well as the fit (represented by the line). It is seen that dE_g/dT rises rapidly at low temperatures, reaches a peak at 15-20 K, and then becomes asymptotic to that of HSC. A peak was predicted by Popko and Pawlikowski[17] from the dilatational part of the temperature dependence of the energy gap. Here the calculations are revised by using more recent data obtained by Caporaletti and Graham[18] for the thermal expansion coefficient of HgCdTe alloys. A value for x = 0.25 alloys has been obtained by averaging the values obtained at 0.20 and 0.30 for dE_g/dT in Ref. 15. The 25 percent rise in dE_g/dT above unity at 15-20 K seen in Fig. 24, is found to agree numerically when the new expansion coefficient value is used in the formula of Ref. 14. Figure 25 shows the difference between our new relationship and that of HSC as a function of temperature for x = 0.2, 0.25, and 0.3. The difference peaks near 15 K and becomes negligible above 100 K for each curve. According to the laws of thermodynamics discussed by Thurmond,[19]

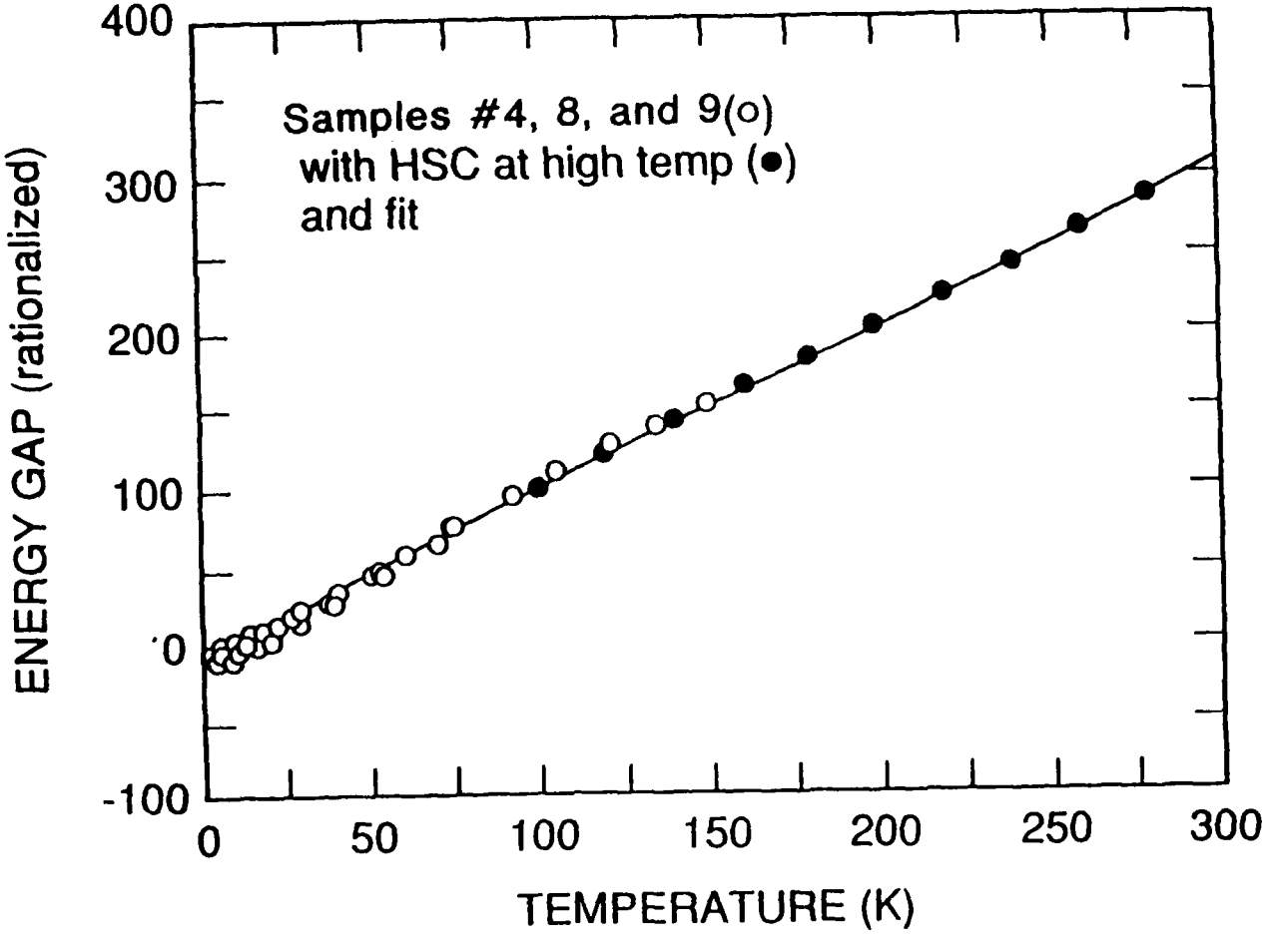

Figure 19. Rationalized energy gaps as a function of temperature for samples #4 (x = 0.239), #8 (x = 0.253), #9 (x = 0.2595). Rationalized values from HSC are used at temperatures above those reached by the data. Fit by the expression $\frac{A + T^3}{B + T^3}$ is the solid line.

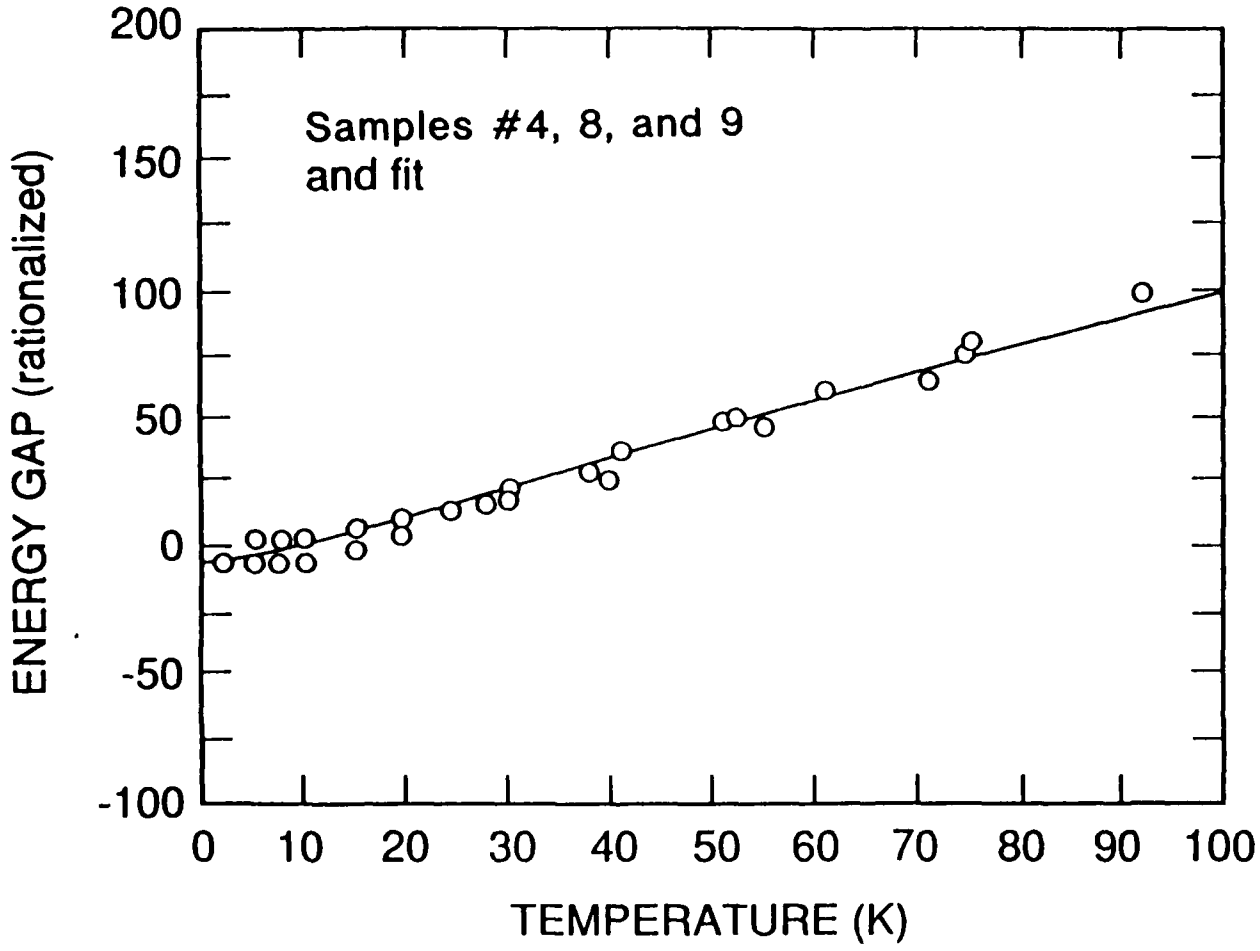

Figure 20. An expansion of Figure 19 between 0 and 100 K.

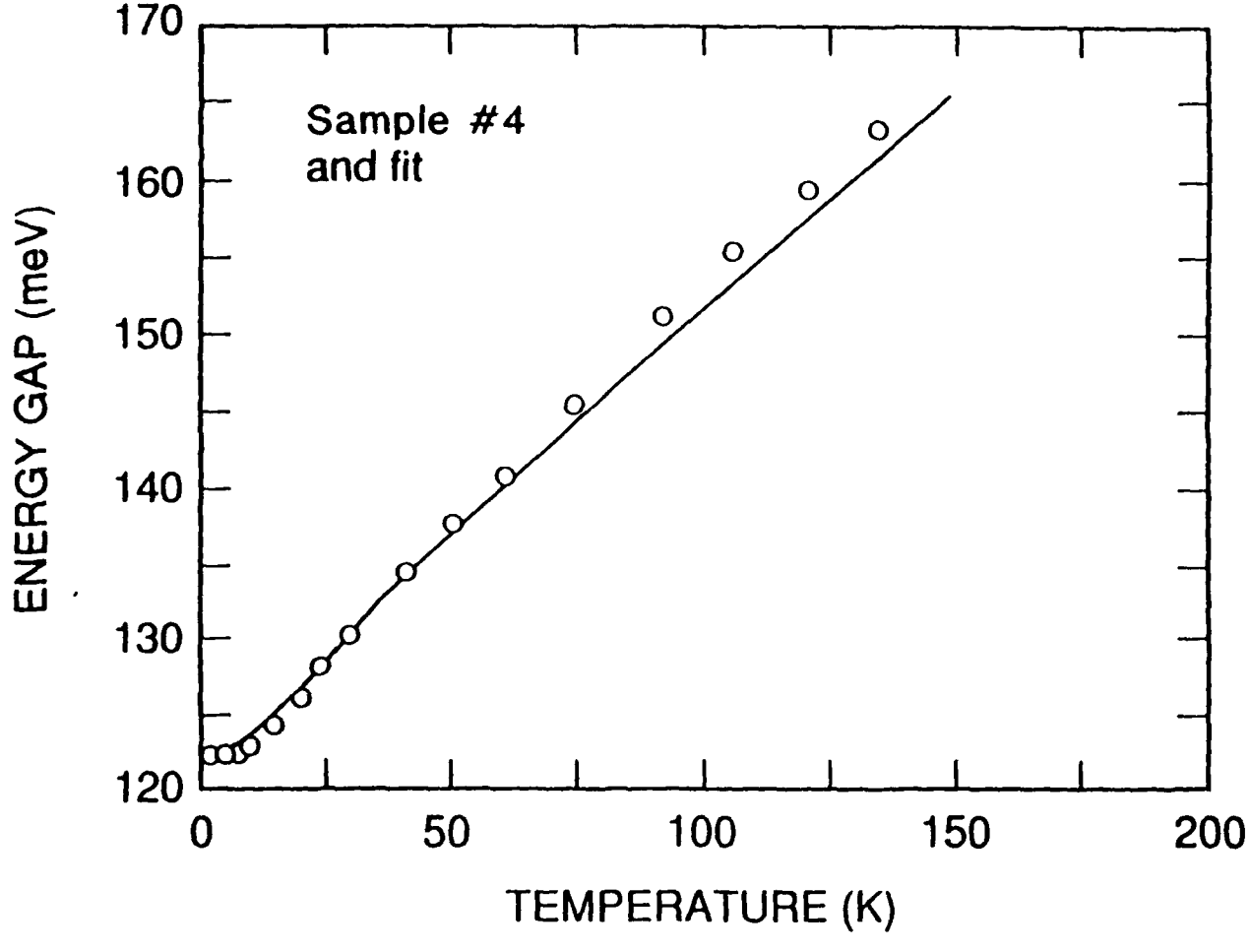

Figure 21. Energy gaps of sample #4 ($x = 0.239$) as a function of temperature. The fit by our new relationship is the solid line.

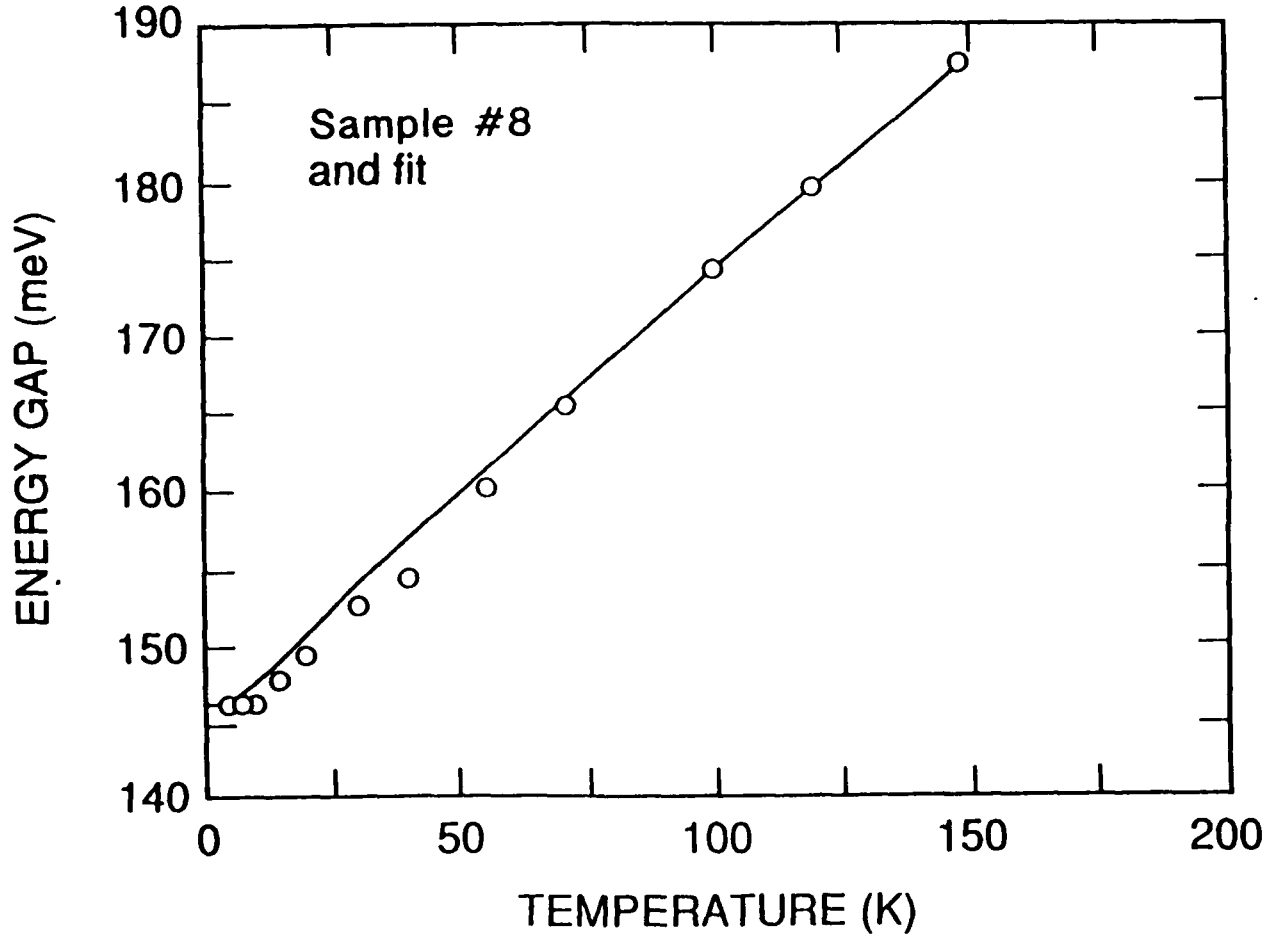

Figure 22. Energy gaps of sample #8 (x = 0.253) as a function of temperature. The fit by our new relationship is the solid line.

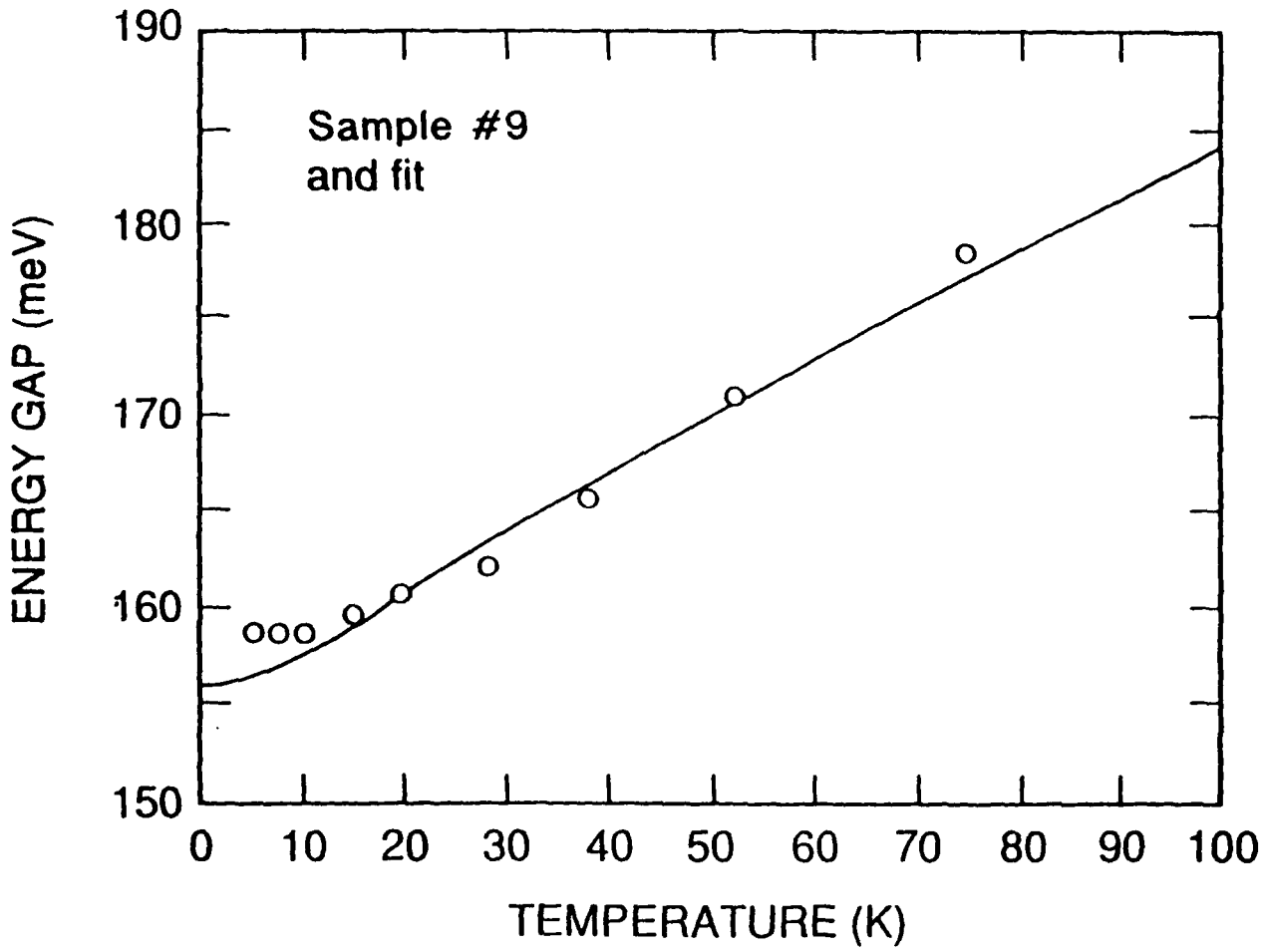

Figure 23. Energy gaps of sample #9 ($x \approx 0.2595$) as a function of temperature. The fit by our new relationship is the solid line.

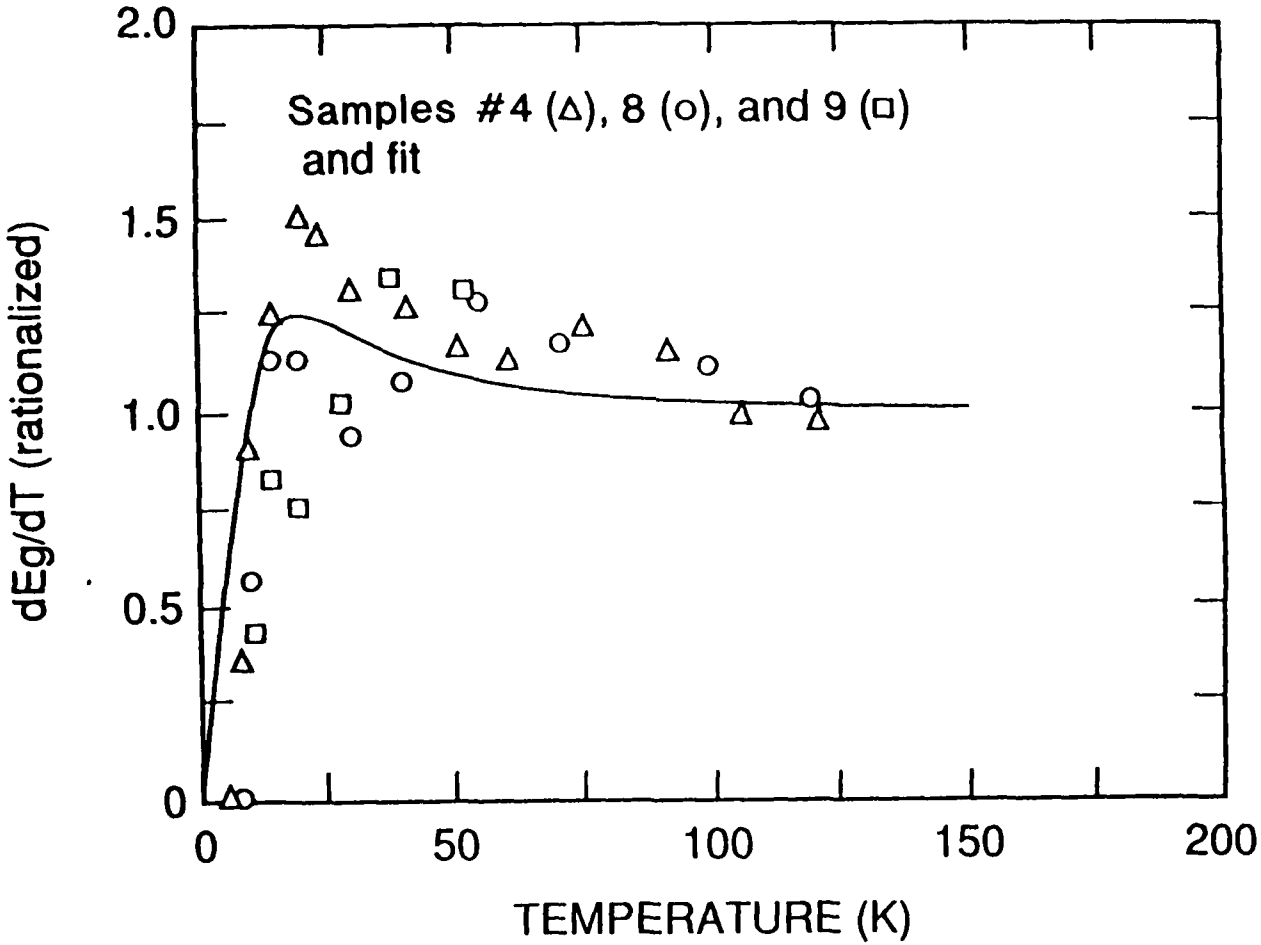

Figure 24. Rationalized derivative of the energy gap with temperature as a function of temperature for the data of samples #4, 8, and 9 (x = 0.239, 0.253, and 0.2592) along with that corresponding to the fit.

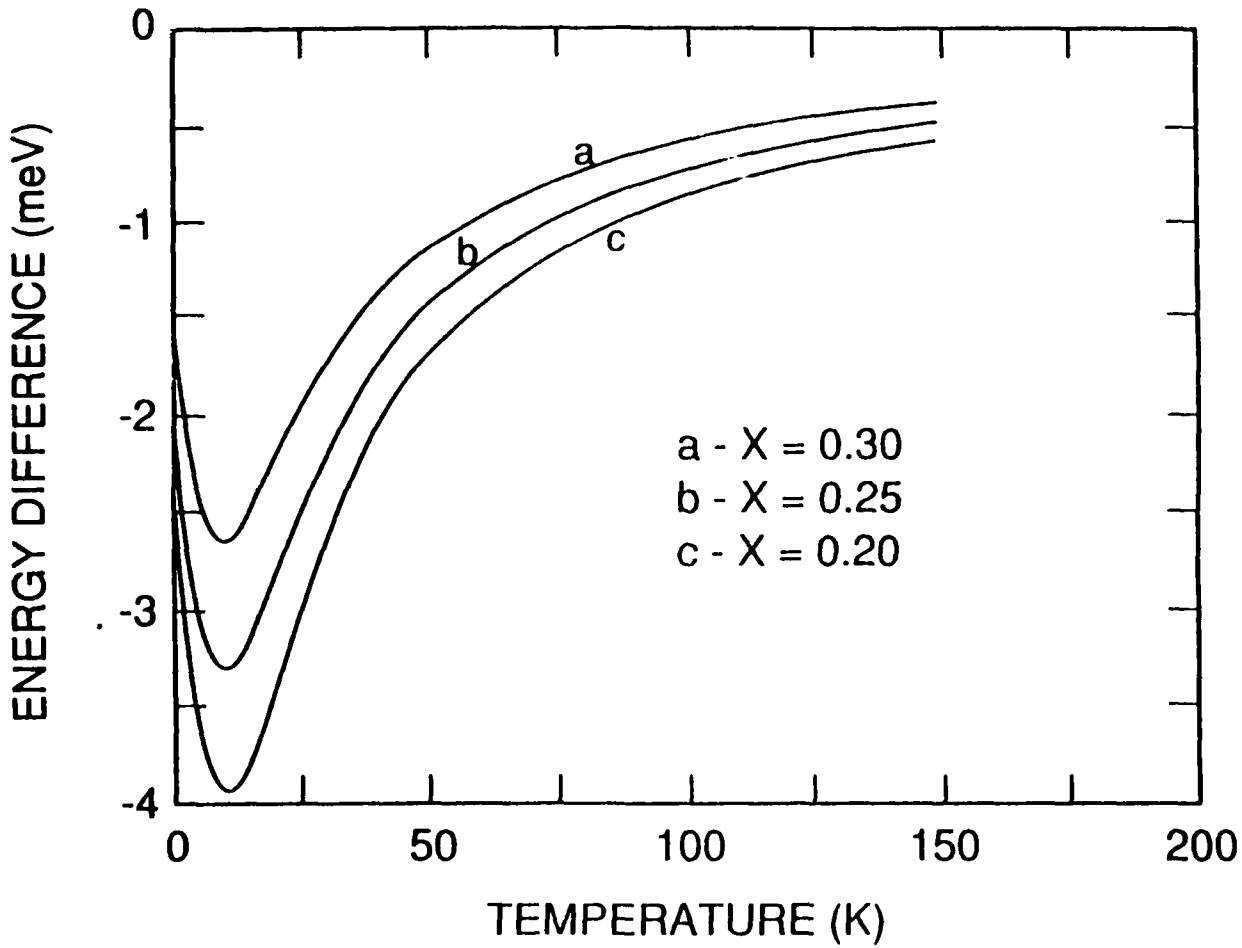

Figure 25. Difference in energy between eq. 2 and HSC as a function of temperature for x = 0.2, 0.25, and 0.3.

the forbidden energy gap, ΔE_{cv} , is the standard Gibbs energy for formation of electrons and holes as a function of temperature. The temperature dependence of ΔE_{cv} may be found from the standard thermodynamic relations:[20]

$$\frac{d(\Delta E_{cv})}{dT} = - \Delta S_{cv} \text{ (fixed pressure)} \tag{3}$$

where ΔS_{cv} is the entropy of formation and T is temperature. By the third law of thermodynamics, $\Delta S_{cv} \rightarrow 0$ as $T \rightarrow 0$, so that $d(\Delta E_{cv})/dT \rightarrow 0$ as $T \rightarrow 0$. The entropy in this case goes to zero physically because all valence states become filled and all conduction states become empty. It is mathematically satisfying that the derivative becomes zero because there is no temperature below absolute zero, which would be needed in the definition of the derivative if it were finite.

Task (c)

In task (b) the observation of magneto-optical resonances due to the presence of impurities and defects was briefly discussed. These results showed that, using magneto-optical techniques, it was possible to measure both shallow acceptor levels and midgap states. During most of this program an emphasis was placed on obtaining sufficient impurity/defect-related magneto-optical data to develop a clearer picture of what levels are present. Consistent use was made of light polarization to determine the origin of the magneto-optical resonances observed. To illustrate the usefulness of light polarization an example of the TPMA and impurity/defect magneto-optical spectra obtained for left circularly polarized (σ_L) and right circularly polarized light (σ_R) are shown in Figure 26 for sample #10. For σ_L two strong TPMA resonances labelled by the solid arrows L_1 and L_2 are seen. The transition assignments for L_1 and L_2 are given in Table II. The two broader absorption peaks, labelled 1 and 2, are ascribed to electron transitions from two closely-spaced impurity/defect levels located at approximately midgap to the lowest-lying conduction band Landau level. The magnetic field positions of all arrows indicate the theoretically expected positions of both the TPMA and the impurity/defect resonances. Upon changing the polarization to σ_R the strong σ_L transitions disappear

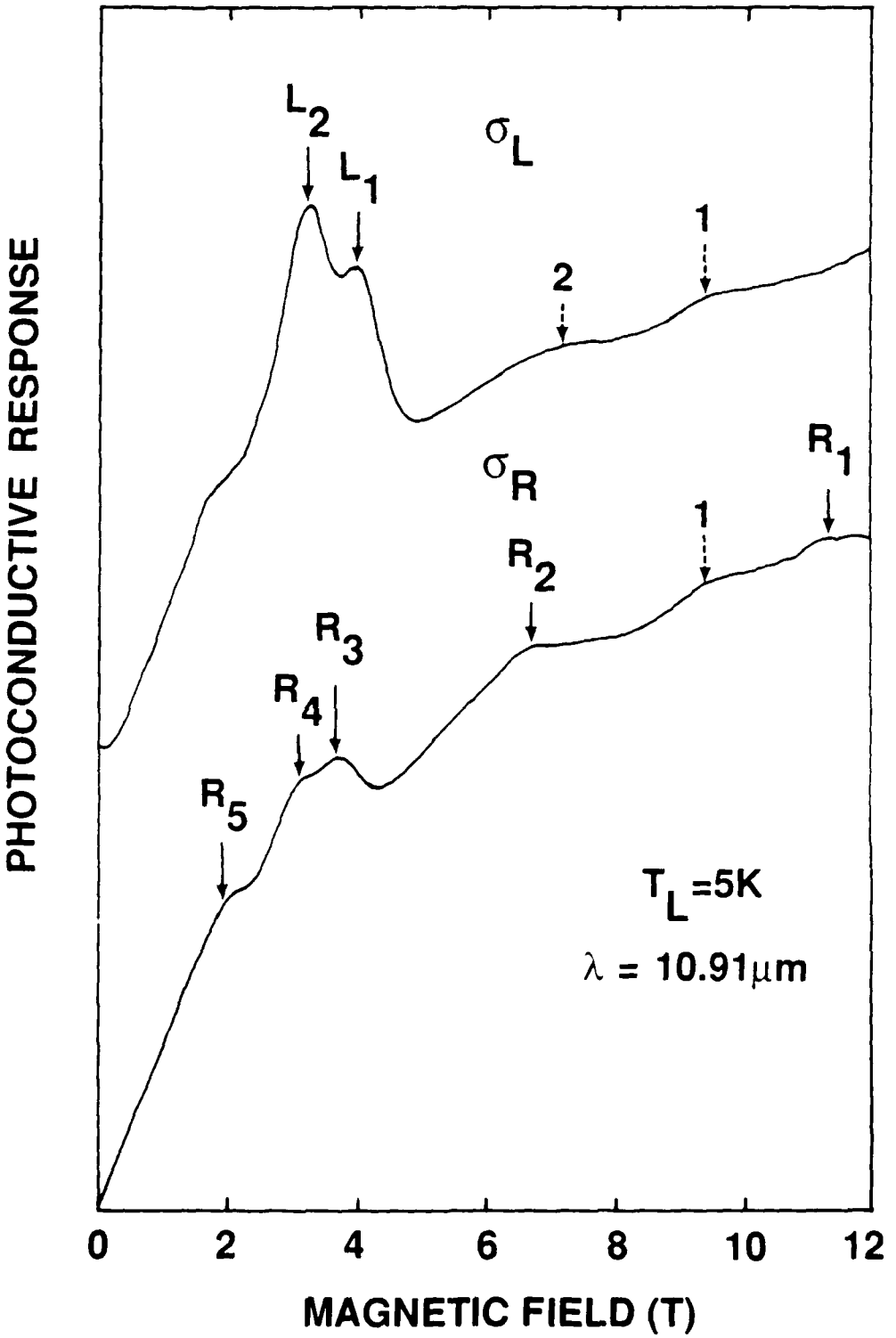

Figure 26. Polarization dependence of the TPMA and impurity/defect transitions. The impurity resonances can be seen for both polarizations, while the TPMA structure obeys two-photon selection rules.

being replaced with weaker TPMA resonances labelled by R_1-R_5. It should be noted that R_1 and R_2 are more widely-spaced in magnetic field than the impurity/defect transitions 1 and 2, and some features of 1 and 2 appear for both polarizations. Thus, by the use of circular polarization, one can separate out the contributions to the magneto-optical spectra from each absorption process mentioned above.

Two-photon interband and impurity-to-band magneto-optical spectra for an n-type sample with x= 0.296 (Sample #11) are shown in Figure 27. The wavelength dependence of the photoconductive response, obtained at 5K, is shown in order of decreasing wavelength or increasing photon energy. The downward-pointing arrows, labelled by the transition assignments L_1, L_2, etc., indicate magneto-optical resonances arising from two-photon magneto-absorption (TPMA), discussed earlier in this report. At higher magnetic fields, beyond the last σ_L TPMA resonance, two magneto-optical resonances are seen. These result from electron transitions from closely spaced impurity/defect levels located at approximately midgap to the lowest-lying conduction band Landau level.

Figure 28 shows a comparison of theoretically calculated and experimentally determined transition energies for both the two-photon and midgap level transitions. The transition energies of the TPMA resonances are described using Equation 1 and the midgap level transitions are given by

$$\hbar\omega = E_c^{a,b}(n_c, B) - E_i, \tag{4}$$

where E_i is the activation energy of the midgap level, as referenced to the valence band edge. Note that as $B \rightarrow 0$, $\hbar\omega \rightarrow E_g - E_i$. The theoretical transition energies shown in Figure 28 were calculated using Weiler's[3] set of energy band parameters in the modified Pigeon-Brown scheme: E_p = 19.0 eV, Δ = 1.0 eV, γ_1 = 3.3, γ_2 = 0.1, γ_3 = 0.9, κ = -0.8, F = -0.8, q =0.0, and N_1 = 0.0. From the TPMA data for sample #11, a value of 222.0 ± 0.5 meV for the energy gap of this sample is obtained. The analysis of the impurity/defect level data yields activation energies of 111.5 meV and 116.0 meV for the two closely spaced midgap levels. It is currently believed that these midgap states result from the formation of cation vacancy, anion impurity complex.

Figure 29 shows the wavelength dependence of PC response of sample # 6. Magneto-optical

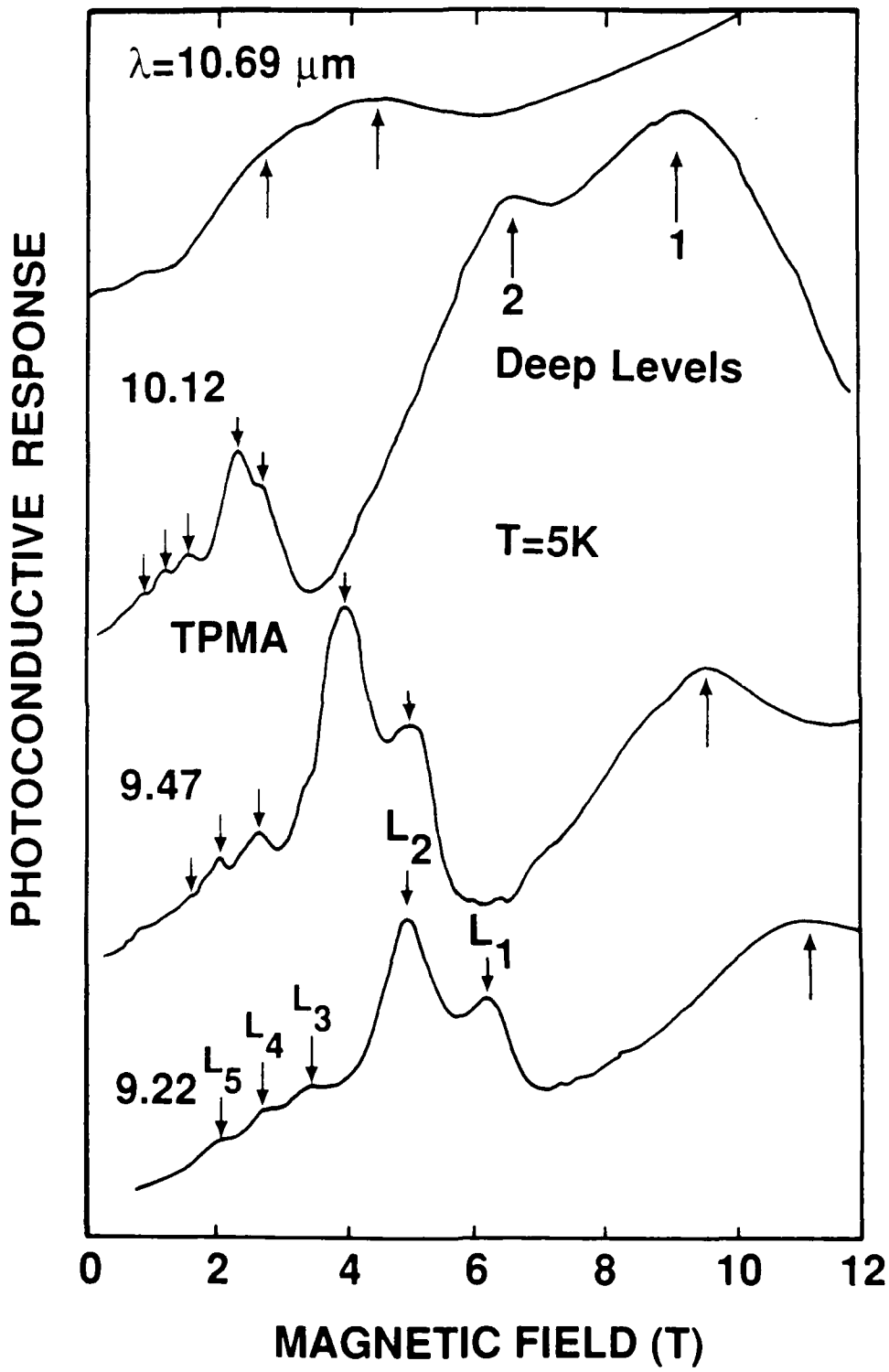

Figure 27. Wavelength dependence for the photoconductive response for sample #11 (x = 0.296), showing both TPMA resonant structure and that arising from impurity/defect-to-band transitions. The transition assignments for the resonances labelled L_1-L_5 are given in Table 1.

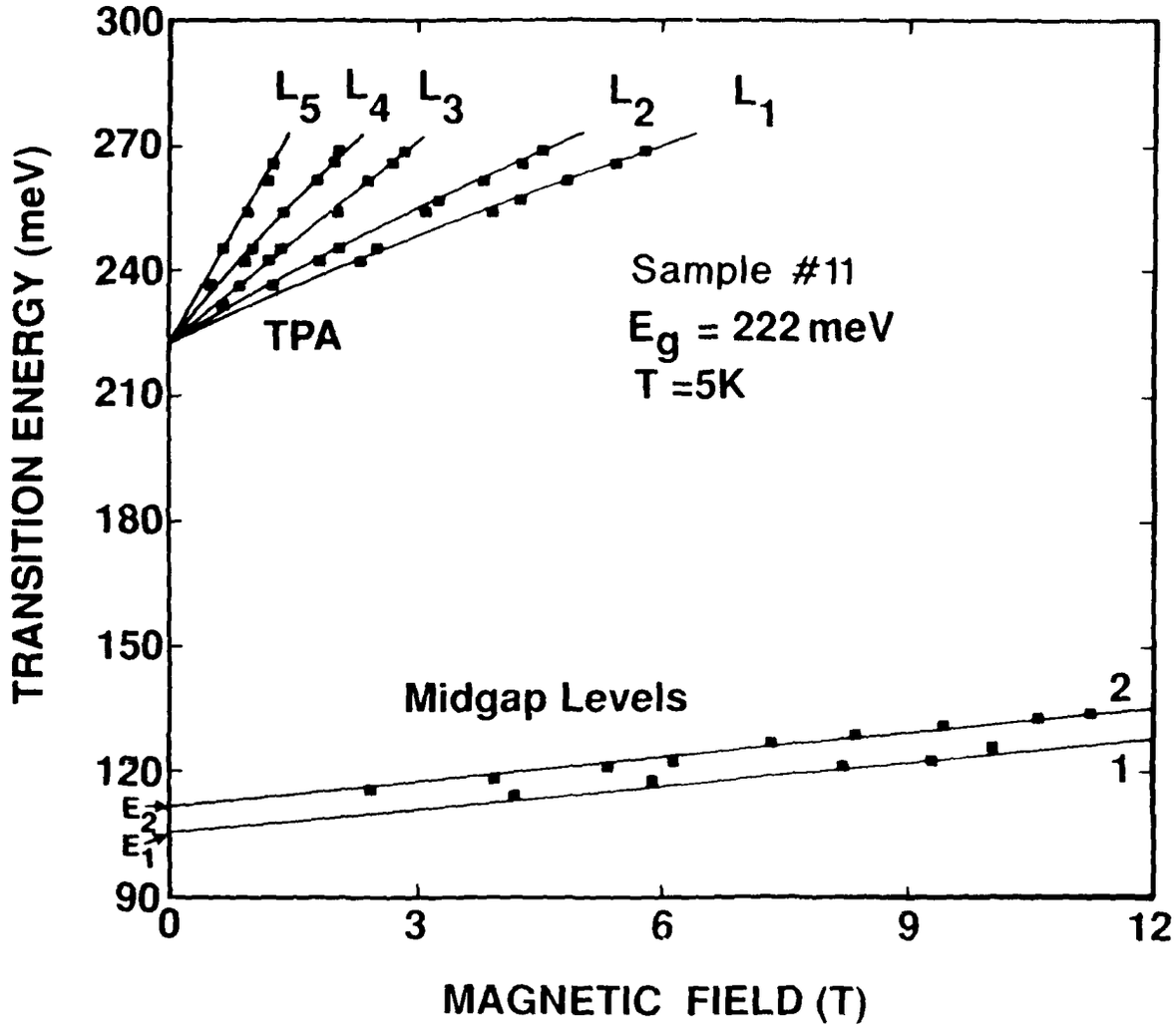

Figure 28. Transition energy versus magnetic field for sample #11. The labels 1 and 2 refer to the near midgap level-to-band transitions $E_1 \rightarrow a^c(0)$ and $E_2 \rightarrow a^c(0)$, where E_1 and E_2 are 111.5 and 116 meV above the valence band edge, respectively.

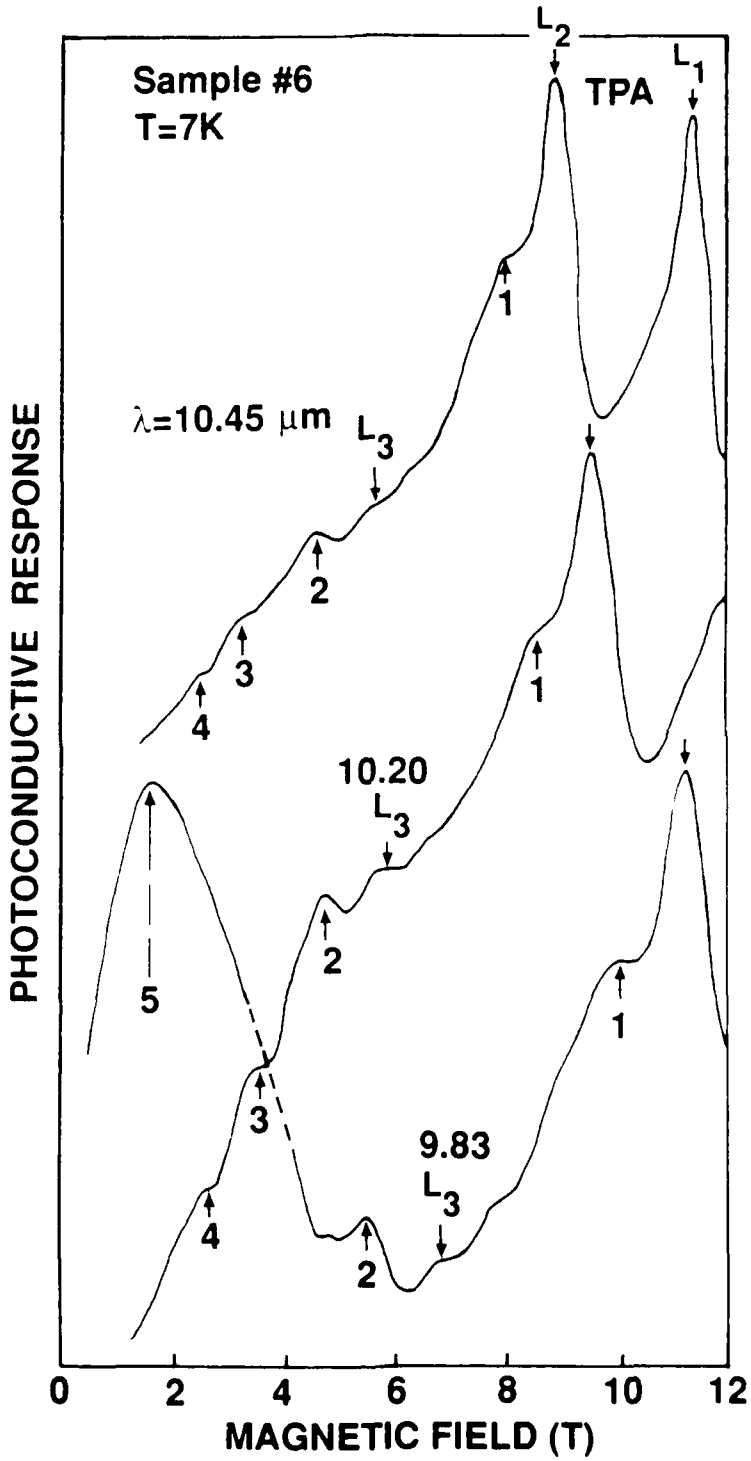

Figure 29. Wavelength dependence for the photoconductive response of sample #6 (x = 0.246), showing both TPMA resonant structure and that arising from impurity/defect-to-band transitions. The labels 1-5 refer to the transitions 1: $E_2 \rightarrow a^c(0)$, 2: $E_1 \rightarrow a^c(0)$, 3: $E_2 \rightarrow b^c(0)$, 4: $E_1 \rightarrow b^c(0)$, and 5: $E_3 \rightarrow b^c(0)$, where E_1, E_2, and E_3 are 63, 68, and 20 meV above the valence band edge, respectively.

structure located at low field are identified as arising from midgap states. Figure 30 shows the comparison between theoretical predictions and magneto-optical absorption data, yielding the energy gap of 136 meV and the activation energies of 63 and 68 meV at T = 7K (reported earlier). In addition, the analysis of the broad resonance labelled 5 in Figure 30 yields an activation energy of 20.0 meV for the shallow acceptor level.

Figure 31 shows impurity magneto-optical (IMO) spectra from sample #3. At low magnetic fields resonant structure (labelled K_1, K_2, K_3 etc.) due to one photon magnetoabsorption (OPMA) are observed. The transition assignments for K_1-K_5 are also given in Table II. The transition energies for OPMA are given by

$$\hbar\omega = E_c^{a,b}(n_c, B) - E_v^{a,b}(n_v, B), \tag{5}$$

where $\hbar\omega$ is the laser photon energy, $E_c^{a,b}(n_c, B)$ represents the energies of the conduction band Landau levels of spin a or b, $E_v^{a,b}(n_v, B)$ represents the energies of the valence band Landau levels, n is the Landau level quantum number, B is the magnetic field strength, and the zero of energy is defined at the zero-field valence band edge. Note that as $B \rightarrow 0$, $\hbar\omega \rightarrow E_g$. Thus, the value of the energy gap can be obtained by fitting the OPMA data using E_g as an adjustable parameter and adding the appropriate exciton correction. From previous studies which compared OPMA and TPMA data obtained on the same sample it was found to be sufficient to add an exciton correction of 2 meV for samples with $E_g \simeq 100$ meV.

At magnetic field beyond which OPMA can be observed, a weak magneto-optical resonance originating from a very shallow acceptor level is seen. The analysis of the OPMA and shallow level data are shown in Figure 32. For the calculation of the activation energy of the shallow level, the transition energies from the impurity or defect levels to the conduction band via one-photon absorption can be described by Equation 5, where E_i is the energy of the identified level (midgap, shallow acceptor, etc.) above the valence band. From the OPMA data an energy gap of 104.0 meV at 5K is extracted and the analysis of the shallow level data yields an activation or binding energy of 7

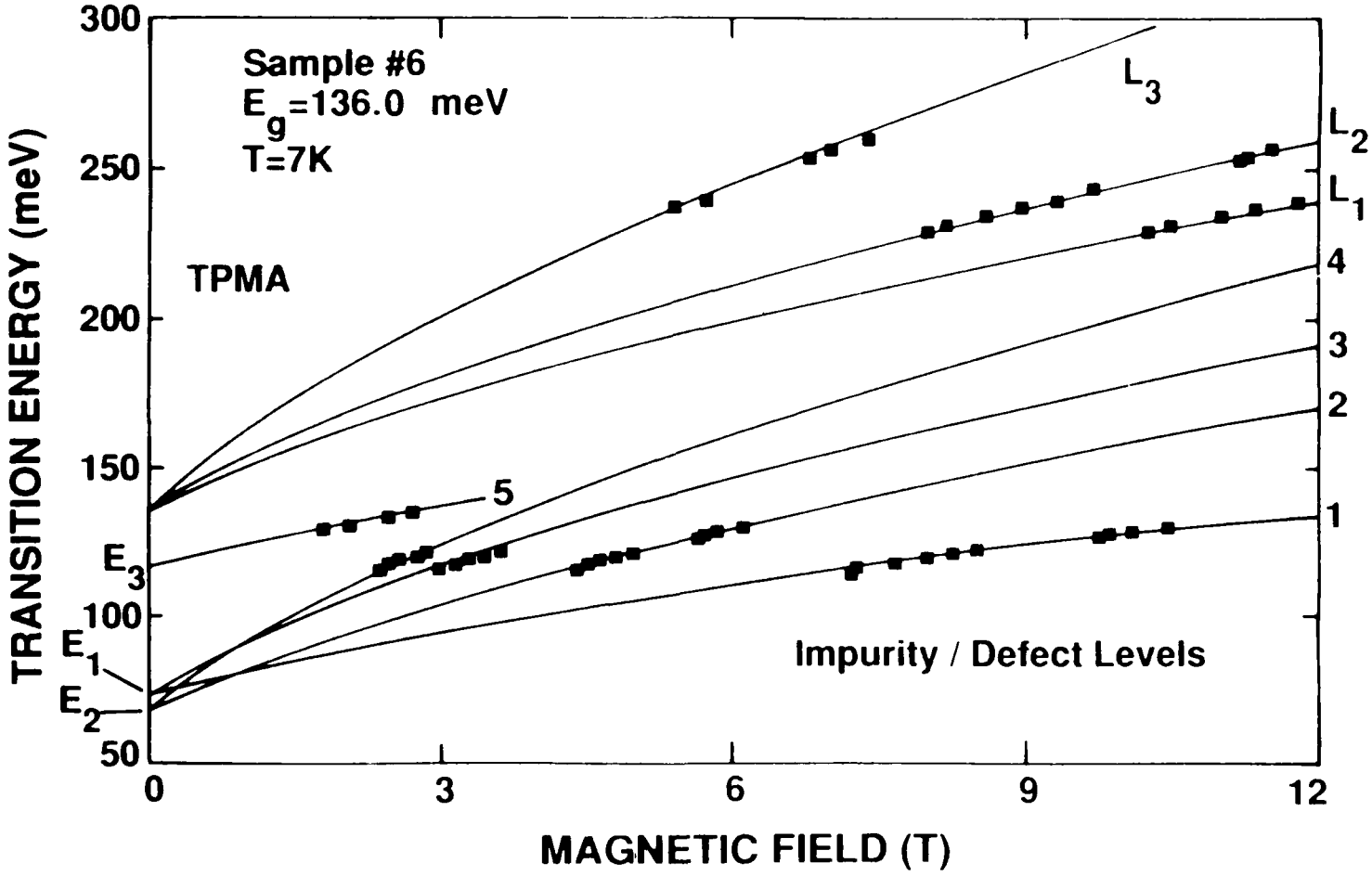

Figure 30. Transition energy versus magnetic field for sample #6. An energy gap of 136.0 meV is obtained from the analysis of the TPMA data, shown by the theoretical lines labelled L_1, L_2 and L_3. The activation energies for the shallow and deep levels E_1, E_2, and E_3. are 63, 68 and 20 meV above the valence band edge, respectively.

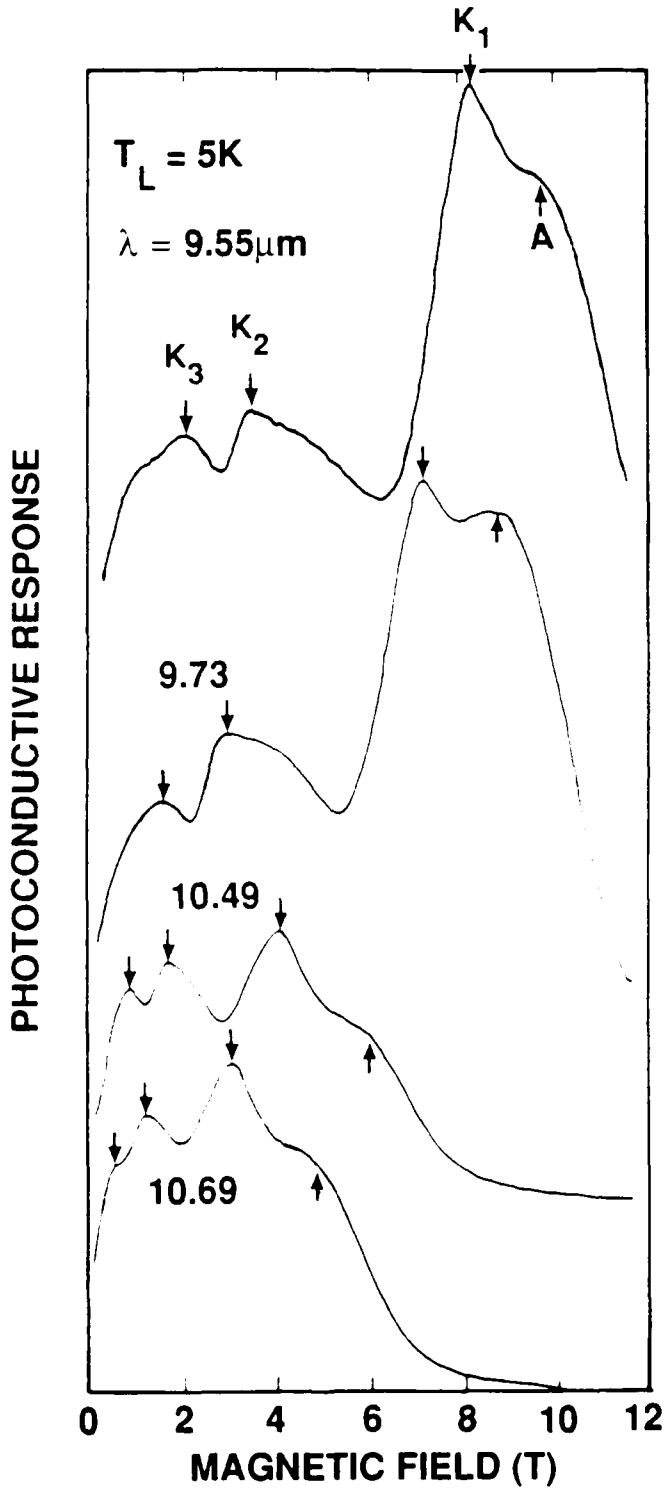

Figure 31. Wavelength dependence for the photoconductive response for sample #3 (x = 0.225), showing both OPMA resonant structure labelled K_1-K_5, and that arising from shallow acceptor impurity-to-conduction band transitions labelled A.

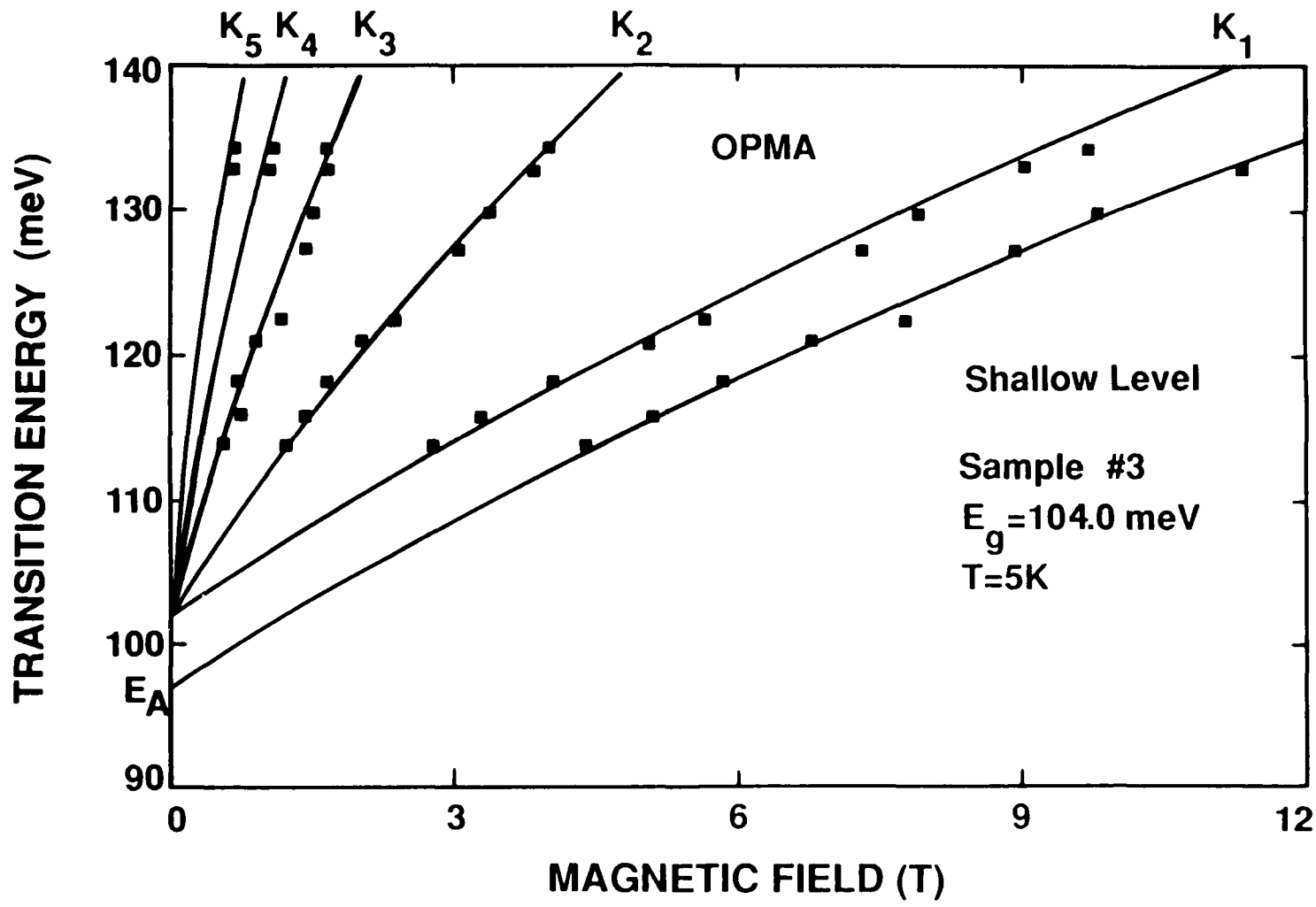

Figure 32. Transition energy versus magnetic field for sample #3. From the fit a value of 7.0 meV is obtained for the acceptor binding energy E_A.

meV. This level is somewhat more shallow than the $\simeq$ 10 meV level observed in the wider gap samples (see Table I), although levels this shallow have been seen in p-type samples with similar x-values (see also Table IV, Bartoli, 1986). The complete results and analysis for 12 samples of different x values are summarized in Table I.

A survey of past work on impurities and defects in HgCdTe is given in Table IV. This table is not meant to be exhaustive, only representative of past work. From this table, several trends emerge: (1) shallow acceptor-like levels with activation energies between $\simeq$ 2 and 20 meV are seen in most samples, (2) near midgap levels are also detected in most samples, and (3) there is evidence for a third level at $\simeq$ 3/4 E_g above the valence band edge. The results of the magneto-optical studies, given in Table I, are in agreement with these conclusions. Thus magneto-optical methods provides a direct, sensitive means of detecting the presence of impurities and defects in HgCdTe alloys.

Finally, new magneto-oscillatory structure has been observed which does not shift with incident photon energy and is thus not magneto-optical in nature. An example of this structure can be seen in Figure #3 and Figure #33 for sample #4. These oscillations are observed only in the photoconductive response at high laser intensities and exhibit a periodicity with inverse magnetic field. Given these features, the following models to explain the data were considered:

(1) Two-dimensional Shubnikov-de-Haas oscillations

(2) Impurity-assisted magnetophonon oscillations.

(3) Magneto-impurity oscillations.

(4) Resonant Impact Ionization of Valence Electrons to Impurity/Defect Levels

After detailed consideration of these models it was determined that either magneto-impurity oscillations or resonant impact ionization could be responsible for the observed oscillations. In order to better interpret the wavelength-independent structure, magnetic field modulation techniques were employed to increase the resolution of the oscillations. An example of the improved resolution is seen in Figure 34. A total of 10 resonances are clearly resolved. To explain the data, models (3) and (4)

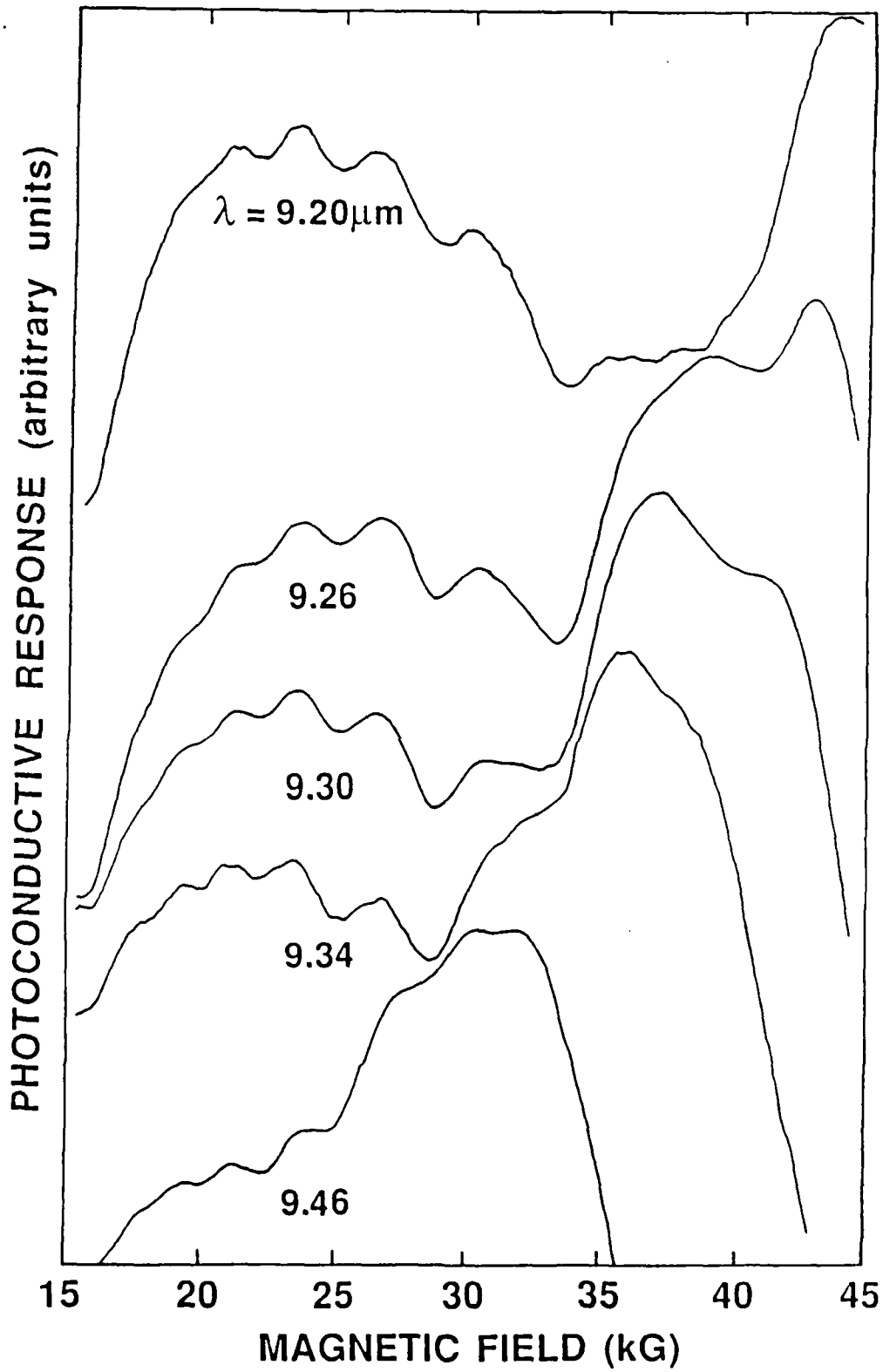

Figure 33. Wavelength dependence of the high intensity structure showing the movement of the one-photon magneto absorption (OPMA) structure against the high intensity structure.

Figure 34. High resolution MI spectra. The data was obtained using magnetic field modulation techniques and represents the 2nd derivative of the photoconductive response vs magnetic field.

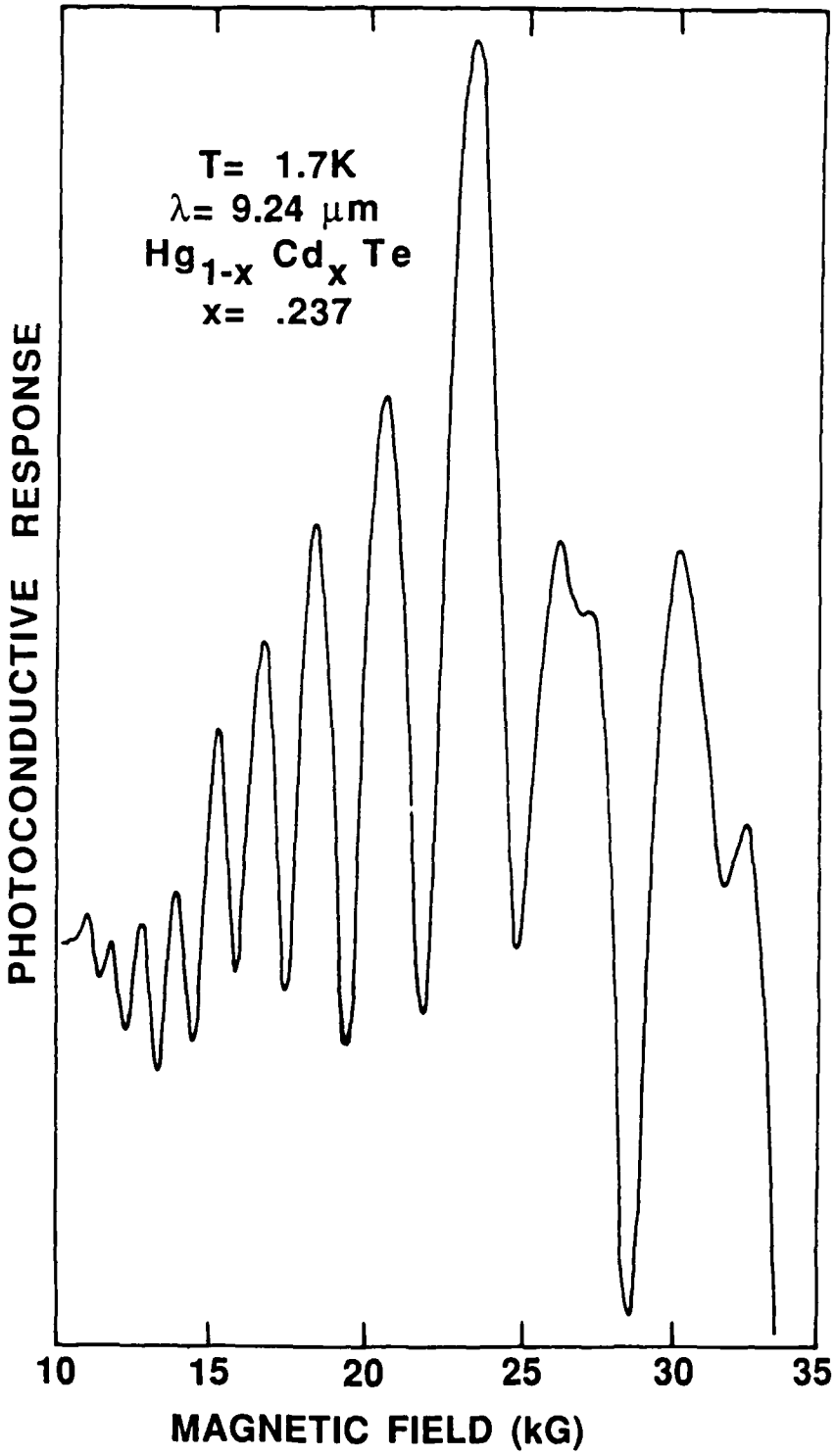

were examined. In the magneto-impurity model resonant scattering of carriers between impurity levels and Landau levels occurs such that oscillations are observed whenever[47]

$$n\hbar\omega_c = E_2 - E_1 \quad , \tag{6}$$

where E_2 and E_1 are the energies of two impurity states, one of which is usually the ground state, and $\hbar\omega_c$ is the energy separation between Landau levels. Since the impurity that dominates the magnetoabsorption spectra is the shallow acceptor level, the MI oscillations involve resonant scattering between the heavy-hole Landau levels and this shallow acceptor's ground and excited states. Figure 35 shows the result of fitting the data presented in Figure 33 using the MI model. The solid lines represent the energy separation between the lowest lying heavy-hole Landau levels (both + and - spins) and successive heavy hole levels, or, equivalently, the field dependence of $n\hbar\omega_c$, and the solid boxes are the magnetic field positions of the MI resonances. A good fit is clearly obtained when E_2-E_1 = -4.25 meV. This energy corresponds closely to that expected for the energy separation between the first excited state of the shallow acceptor to the valence band continuum.

In order to verify the involvement to the shallow impurity in the observed resonant structure, a temperature dependence of the oscillations was recorded. A example of this is shown in Figure 36. The strength of the oscillations are seen to be strongly temperature dependent, essentially vanishing above 21 K. This would be expected if the energy states of a shallow impurity played a role in the oscillations, since they are rapidly ionized with increasing temperature. The resonant structure also moves to higher magnetic field with increasing temperature, consistent with the model.

In model (4) the oscillatory structure is due to relaxation of photoexcited hot electrons via impact ionization of valence electrons into trap levels. The hot electrons are created by interband absorption of CO_2 laser radiation. The conditions necessary for the impact ionization process to occur are a nonequilibrium electron distribution and whenever relaxation cannot occur by emission of longitudinal optic phonons. For the HgCdTe data shown in Figures 33 - 36 the magnetic field creates the nonequilibrium electron distribution and the phonon energy is less than the Landau level

separation. The proposed process for our HgCdTe data is then the following: (1) Sequential absorption of two photons, creating a population of hot electrons, (2) Auger relaxation of the hot electrons, with subsequent impact ionization of valence electrons to the midgap levels.

Currently, both models can describe the observed data and work is continuing to confirm which model is correct. If Model (4) is correct then this would represent a new type of spectroscopy for impurity and defect levels using near (above) band gap photon energies, thus extending the range of the currently available magneto-optical work.

Task (d) and (e) Work in these tasks has proceeded in two areas: (1) The development of a novel method to determine the true minority carrier lifetime in p-type narrow gap materials, and (2) the investigation of laser-induced impurity absorption processes and carrier dynamics in p-type material. Work in the second area is aimed primarily at determining the individual absorption and recombination coefficients of impurity and defect levels along with their respective concentrations. Progress in these areas is summarized below:

During the first year a novel method was developed to determine minority carrier lifetimes. The basis for the method about to be discussed is a technique recently developed at UNT to obtain information about multi-carrier semiconductor systems (see Applied Physics Letters, Volume 51, p. 1916, 1987; a reprint of this article is also appended). The technique employs the measurement and subsequent analysis of the magnetoconductivity (MC) tensor components σ_{xx} and σ_{xy} of a semiconductor. By analyzing the MC tensor components it was shown that the carrier concentration and mobility of both majority and minority carriers could be easily obtained. Although the method was first applied to multi-carrier analysis in dark, thermal equilibrium conditions, it was shown this year to be applicable to the analysis and study of photo-excited carriers under laser excitation (i.e., nonequilibruim) conditions. This permitted the extraction of "true" minority carrier lifetimes in p-type semiconductors.

To test the concept out, samples of p-InSb were first used. Figure 37 shows the σ_{xy} component of the MC tensor versus magnetic field under dark, thermal equilibrium conditions at four

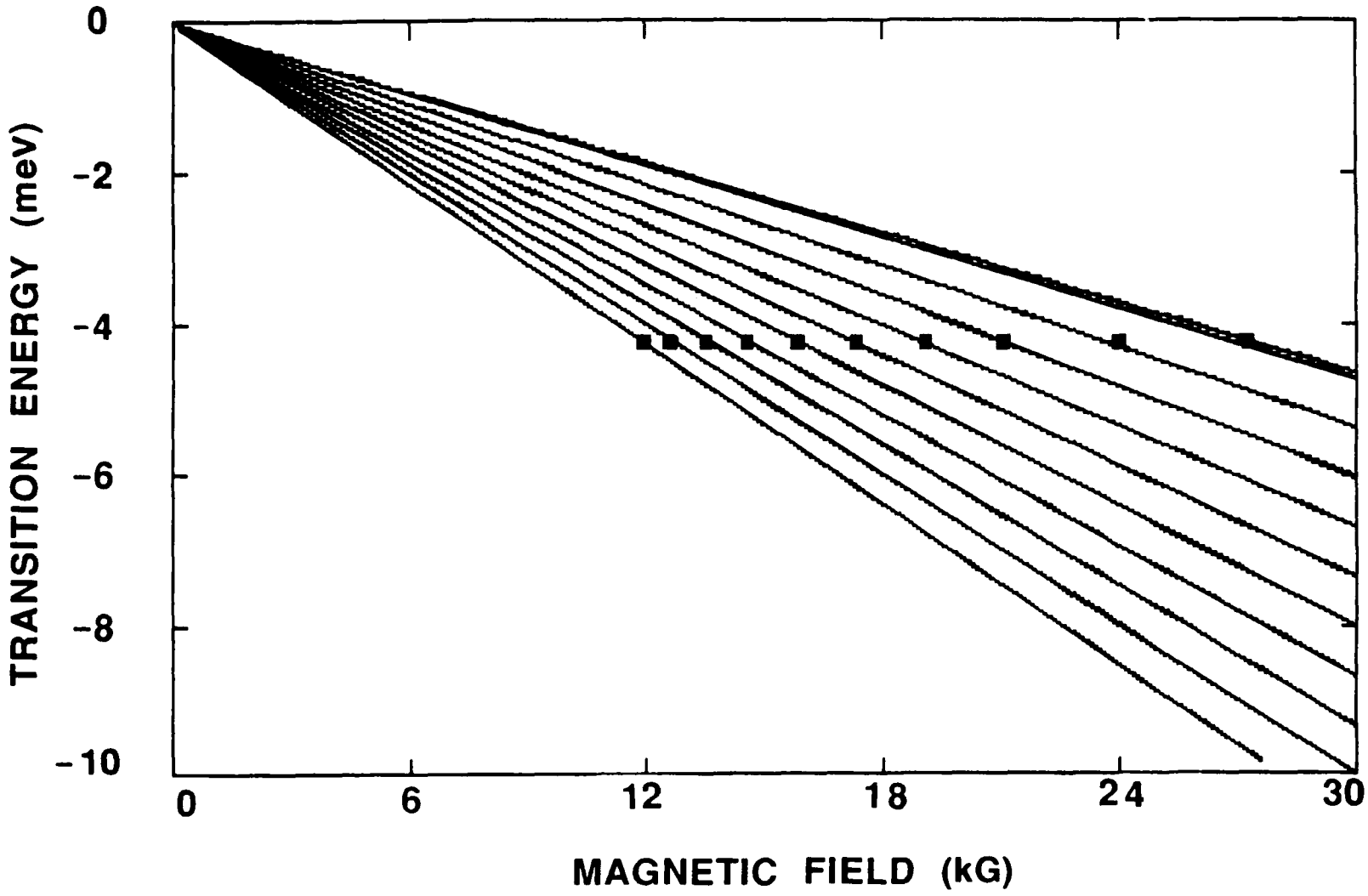

Figure 35. Analysis of MI data. Solid lines represent $n\hbar\omega_c$ energies and open boxes represent the data.

Figure 36. Temperature dependence of the magneto-impurity oscillations.

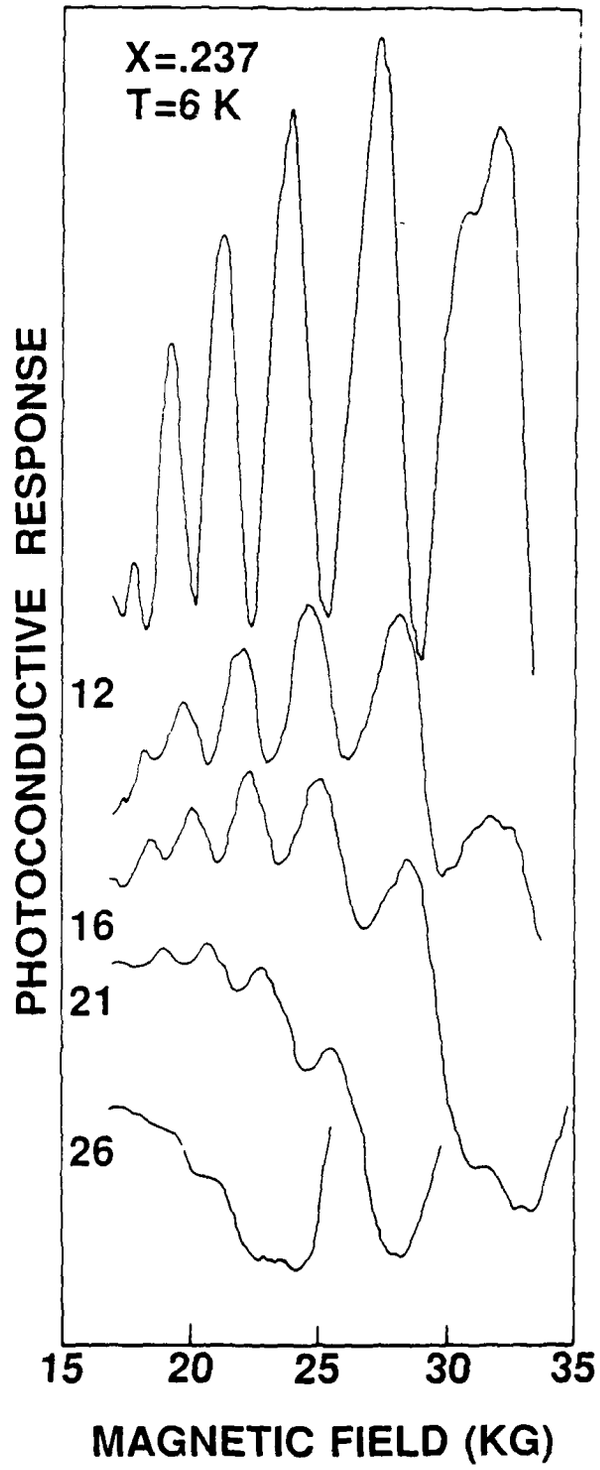

different temperatures. At lower temperatures (77 and 100K), only heavy and light holes can be seen, as expected. However, at 135K, the presence of a relatively small concentration of intrinsic electrons (minority carriers) can be detected. At 160K, however, the number of intrinsic electrons thermally excited across the gap completely dominates the transport of the sample at low magnetic fields. Details of the analysis are given in the appended Applied Physics Letter.

A Tektronix waveform digitizer was used to capture the transient behavior of σ_{xy}, allowing the effect of a CO_2 laser pulse, (98 nsec full width at half maximum) incident on the sample, to be observed. An example of the effect of laser excitation on σ_{xy} is shown in Figure 38. The laser wavelength (9.25 μm) was chosen such that two-photon excitation was present and thus the TPMA-generated minority carriers (electrons) could be observed and studied. Figure 39a shows the following four sets of transient data and corresponding theoretical curves: (1) in the dark, at a time before the laser pulse is incident on the sample, (2) at the peak of the signal, at a time 325 ns after the start of the laser pulse, (3) 435 nsec after, and (4) 515 nsec after. Note from Figure 38 that the peak of the signal occurs approximately at the end of the laser pulse. Figures 39b and 39c show how the MC tensor analysis can be used to extract the time-resolved behavior of the minority carrier concentration. Thus, the magnetophotoconductivity (MPC) technique can provide directly the number of photoexcited minority carriers Δn as a function of time and, as a result, the true minority carrier lifetime.

Figure 40 shows the number of photoexcited electrons Δn as a function of time for T = 100 and 160K obtained using the MPC technique. Note that the technique is extremely sensitive to the number of minority carrier electrons (detection limit $\simeq 4 \times 10^{10}$ cm^{-3} electrons in the presence of $\simeq 2 \times 10^{14}$ cm^{-3} holes at 100K). For comparison purposes, the time variation of the photoconductive (PC) response is also plotted. It is seen that the PC response possesses a single stage decay for T = 100K and a two-stage decay for T = 160K. The electron lifetime at 100K is seen to be much shorter than the lifetime implied by the PC response and follows the first stage of the two-stage PC decay for T = 160K. At 100 K, the PC response is known to be dominated by impurity absorption, creating

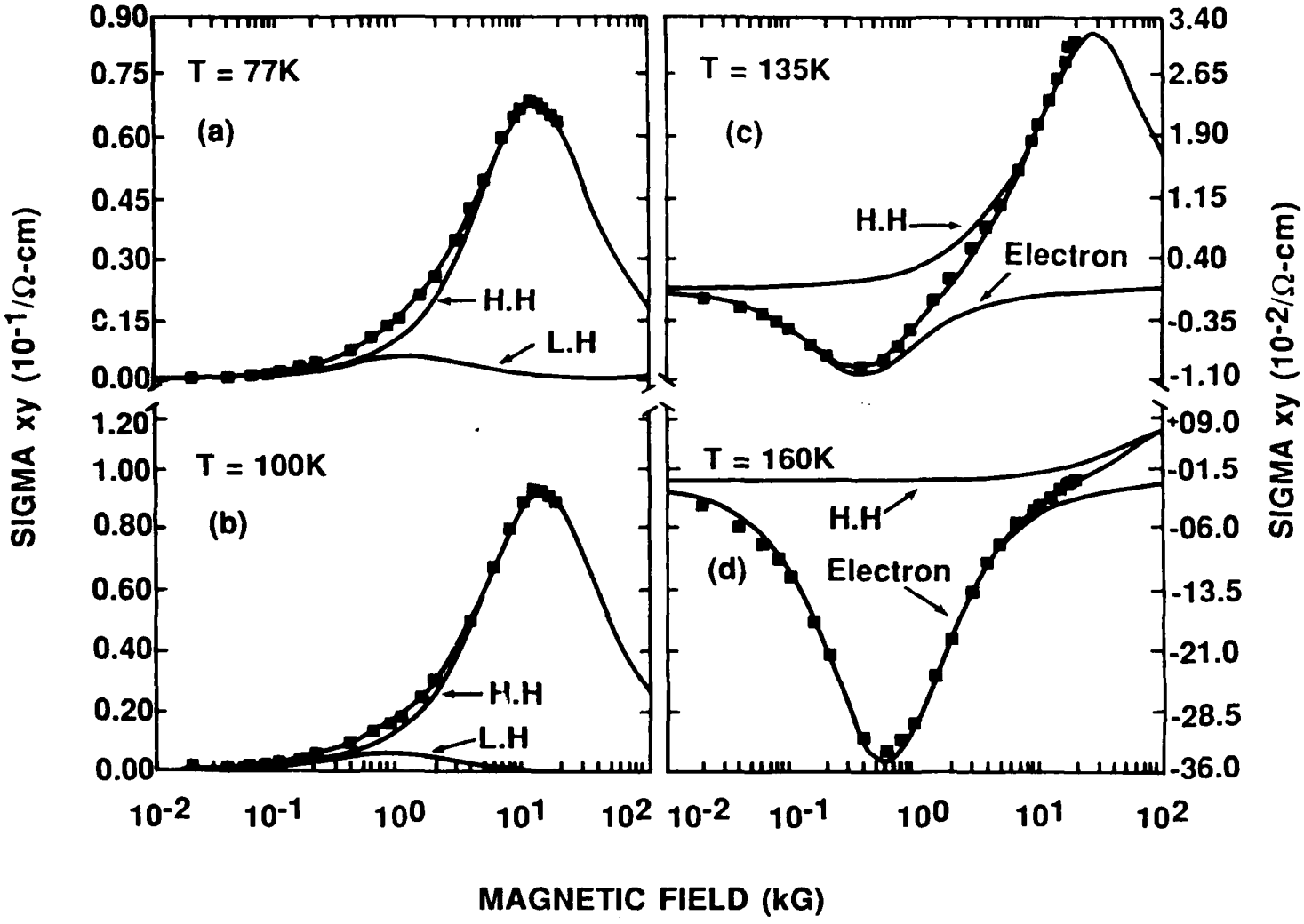

Figure 37. σ_{xy} vs. magnetic field for various temperatures.

Figure 38. Time resolved data:

a) σ_{xy} values in the dark, 325, 435, and 515 nsec after start of laser pulse.
b) Response in the dark, before the laser pulse.
c) Peak signal, corresponding to the peak of the laser pulse.

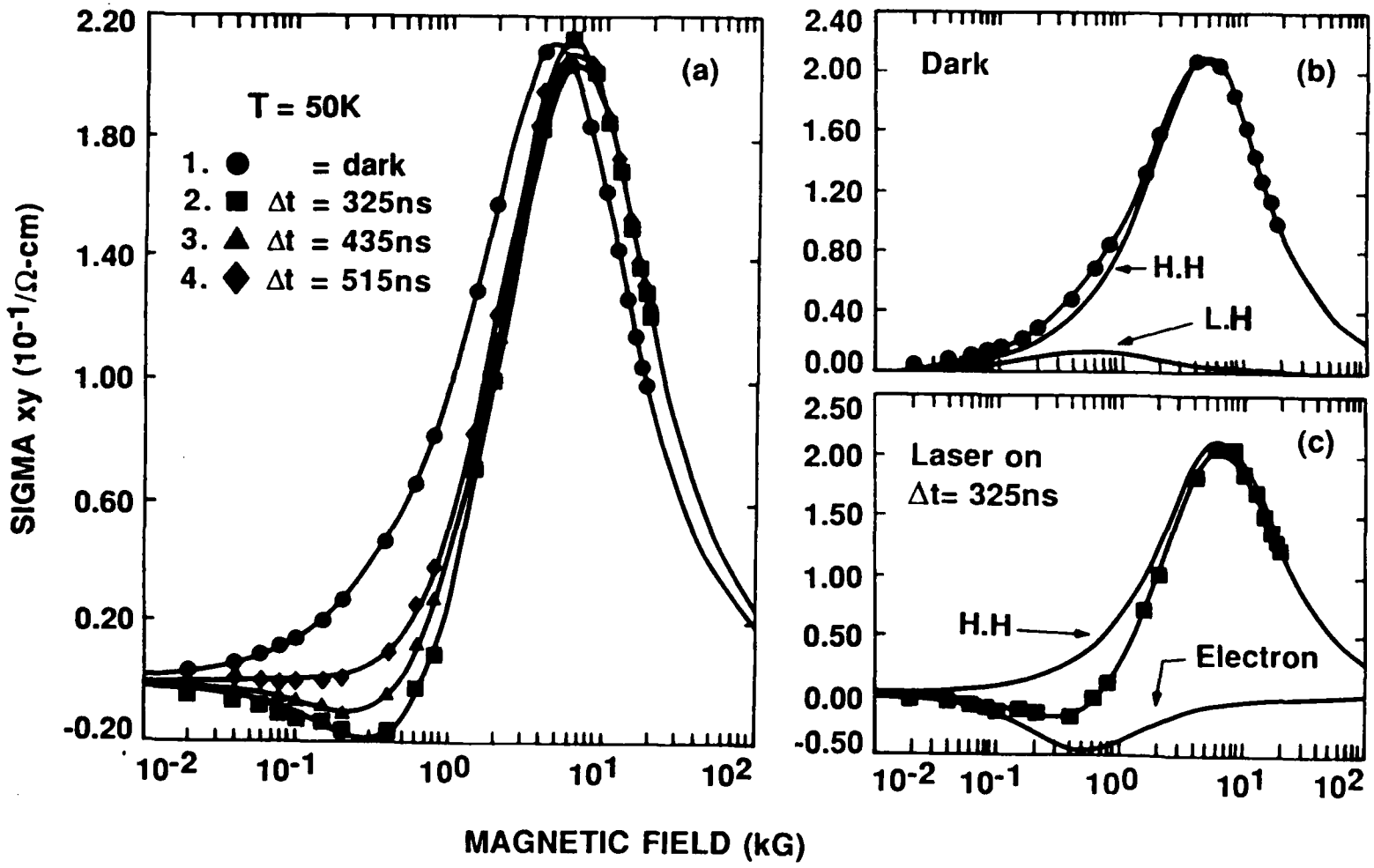

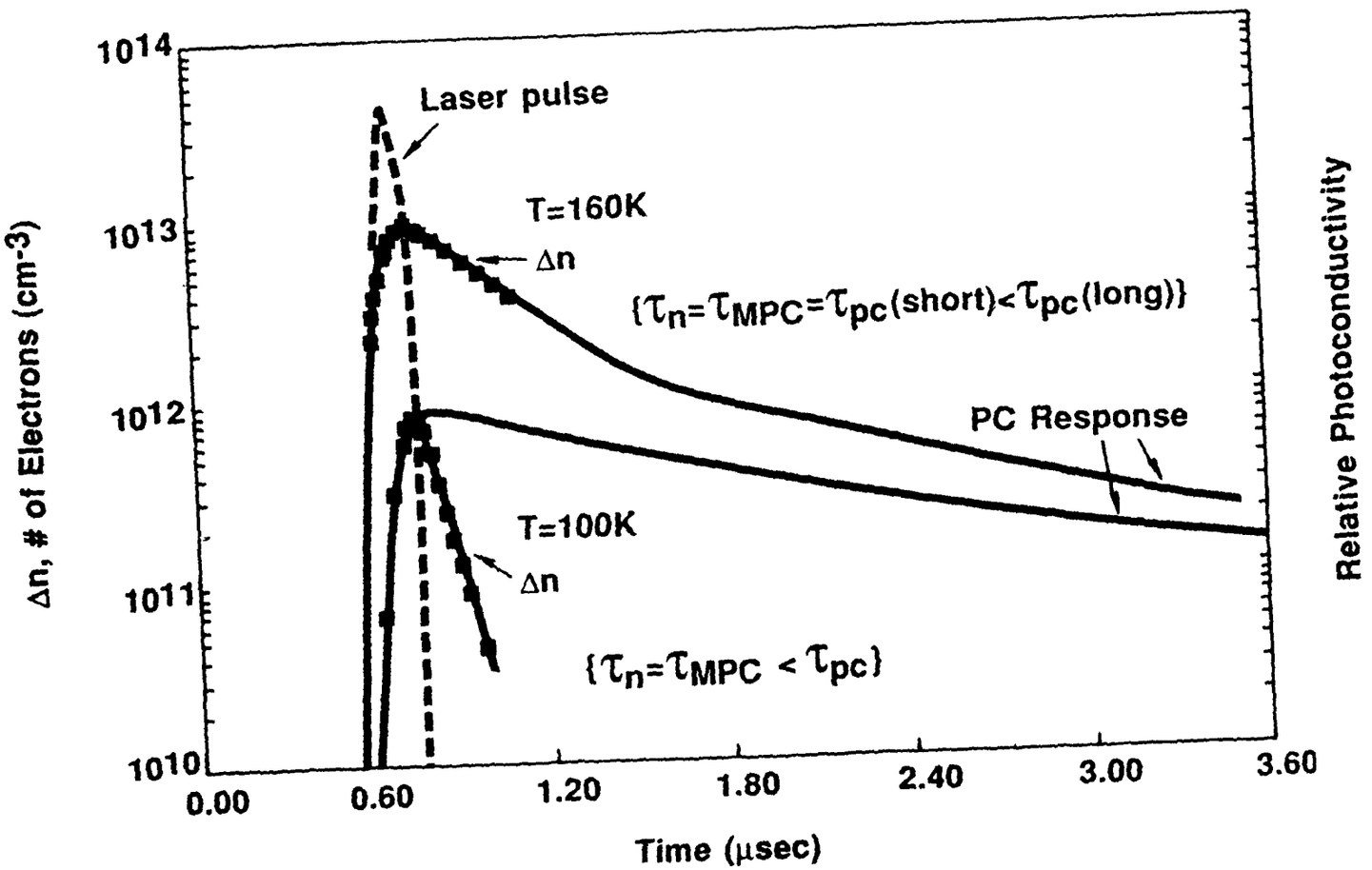

Figure 39. Comparison of the photoconductive and the magneto-photoconductive responses.

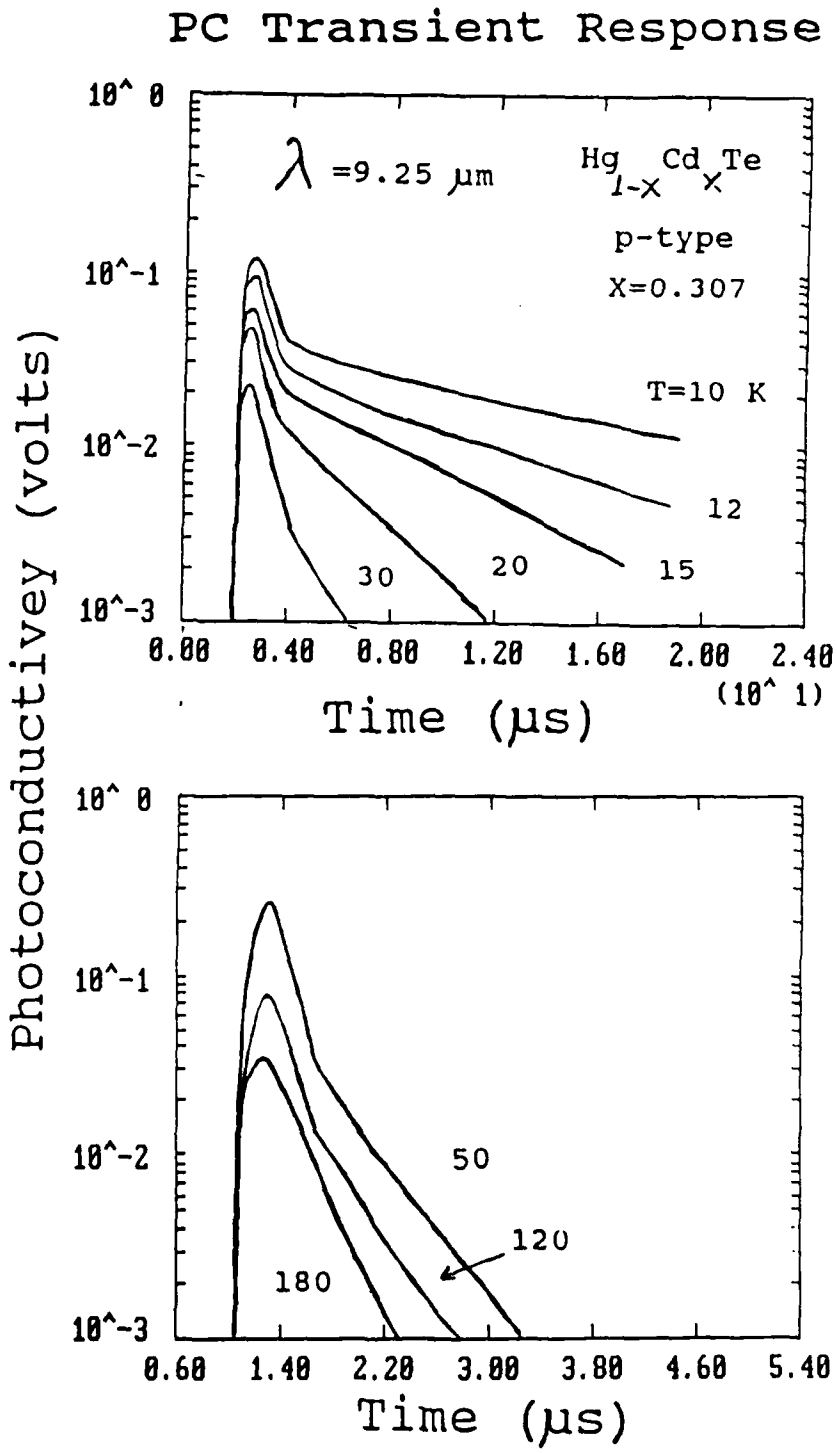

Figure 40. Transient photoconductive response at various temperatures.

only holes with a long lifetime. The presence of the much smaller concentration of two-photon created electrons can only be detected by the more sensitive MPC method. At 160K, intrinsic conduction dominates and hence the first stage decay of the PC response is due to a decrease in the number of minority-carrier electrons, in agreement with the results of the MPC analysis. Further details of this work are given in the Applied Physics Letter appended to this report.

II. Other Areas

Our investigation of p-type samples of HgCdTe have revealed some new magneto-optical effects. One of these which can be at least qualitatively explained at this point in time will be discussed below. Figure 41 shows the photovoltaic response of a sample of x = 0.244 p-type HgCdTe. Clearly seen in the spectra shown are a series of resonances which shift to lower magnetic fields for longer CO_2 laser wavelengths (see arrows). Upon analysis of the magneto-optical results, the only model which could quantitatively explain the transition energy data was a phonon-assisted free carrier absorption process, where energy conservation demands

$$\hbar\omega = E_2 - E_1 + n\hbar\omega_{lo}, \tag{7}$$

where E_1 and E_2 represent Landau level energies and $\hbar\omega_{lo}$ is the longitudinal optical phonon energy. In our case, the best fit to the data (shown in Figure 42) is obtained from harmonics of combined resonance of free holes with the assistance of two optic phonons. This yields a optic phonon energy of $\simeq$ 15 meV, in reasonable agreement with the optic phonon energy in HgCdTe with $x \simeq 0.24$.[48]

The principal goal of this program was to develop two-photon absorption spectroscopy (TPAS) as a tool for characterizing alloys of HgCdTe. This included the the study of the band structure of HgCdTe and the identification of impurity and defect levels in the forbidden energy gap. As a result of this program, magneto-optical spectroscopy (MOS) measurements have provided a new means of studying the electrical and optical properties of (Hg,Cd)Te. Two-photon magnetoabsorption (TPMA)

has been used to accurately determine the temperature dependence of the energy gap of various (Hg, Cd)Te alloys, revealing behavior that deviates from currently accepted models. In addition, magneto-optical techniques have been used to detect the presence of both shallow and deep impurities/defects and accurately determine their activation energies. All of the results shown in this report represent first observations of each type of phenomena in HgCdTe, whether magneto-optical, magnetotransport, or lifetime related. These techniques have, during this program, been developed to the point that they can be used to study specifically "tailored" (i.e., specifically doped, annealed, and/or processed), and provide quantitative information about the impurity or defect levels that most strongly influence infrared device or detector performance. Thus, the TPAS technique has been sufficiently developed to assure its success as a powerful technique for the characterization of HgCdTe alloys.

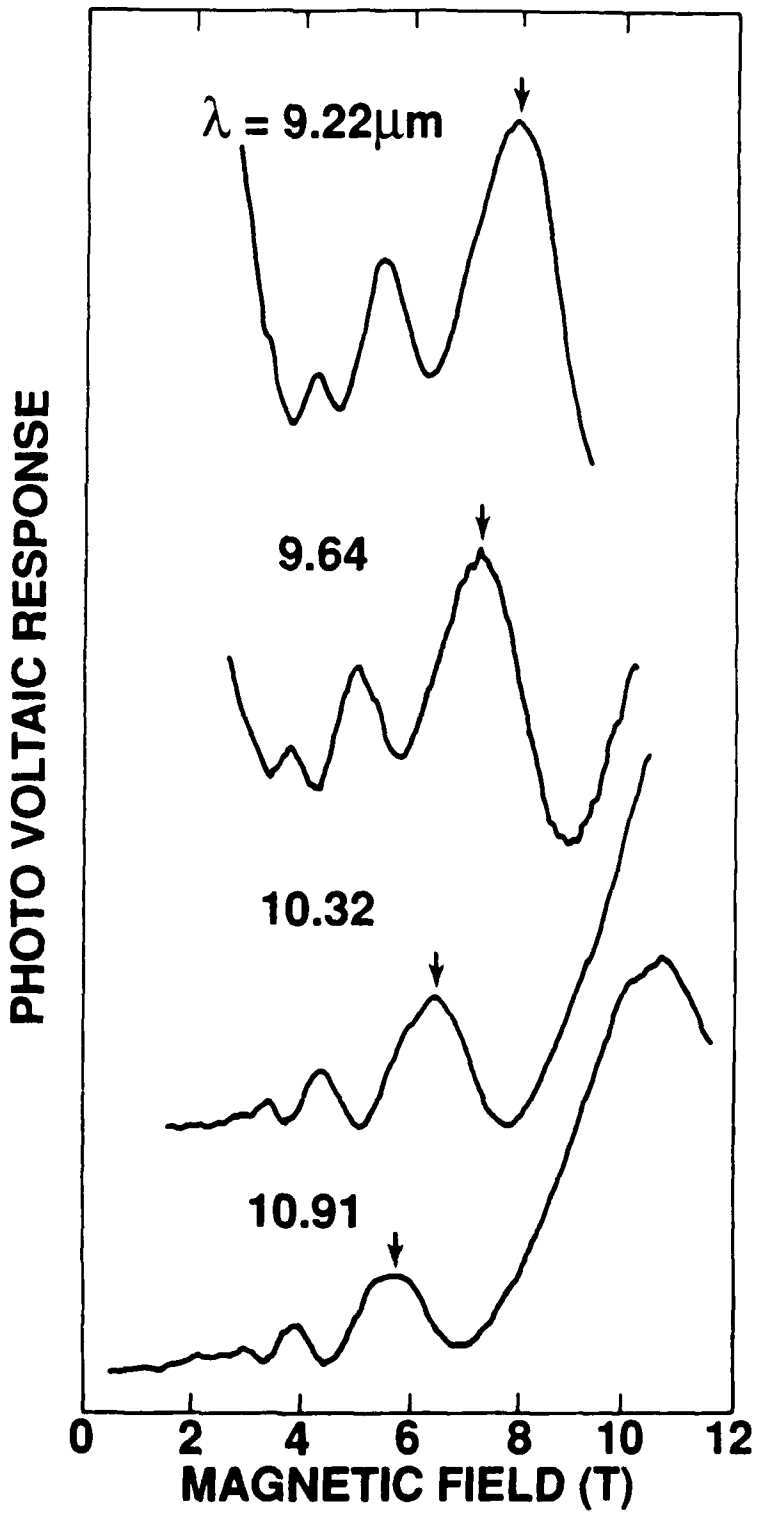

Figure 41. Magneto-optical resonances for a p-type sample with x = 0.244. The arrows indicate how a given resonance tracks with photon energy.

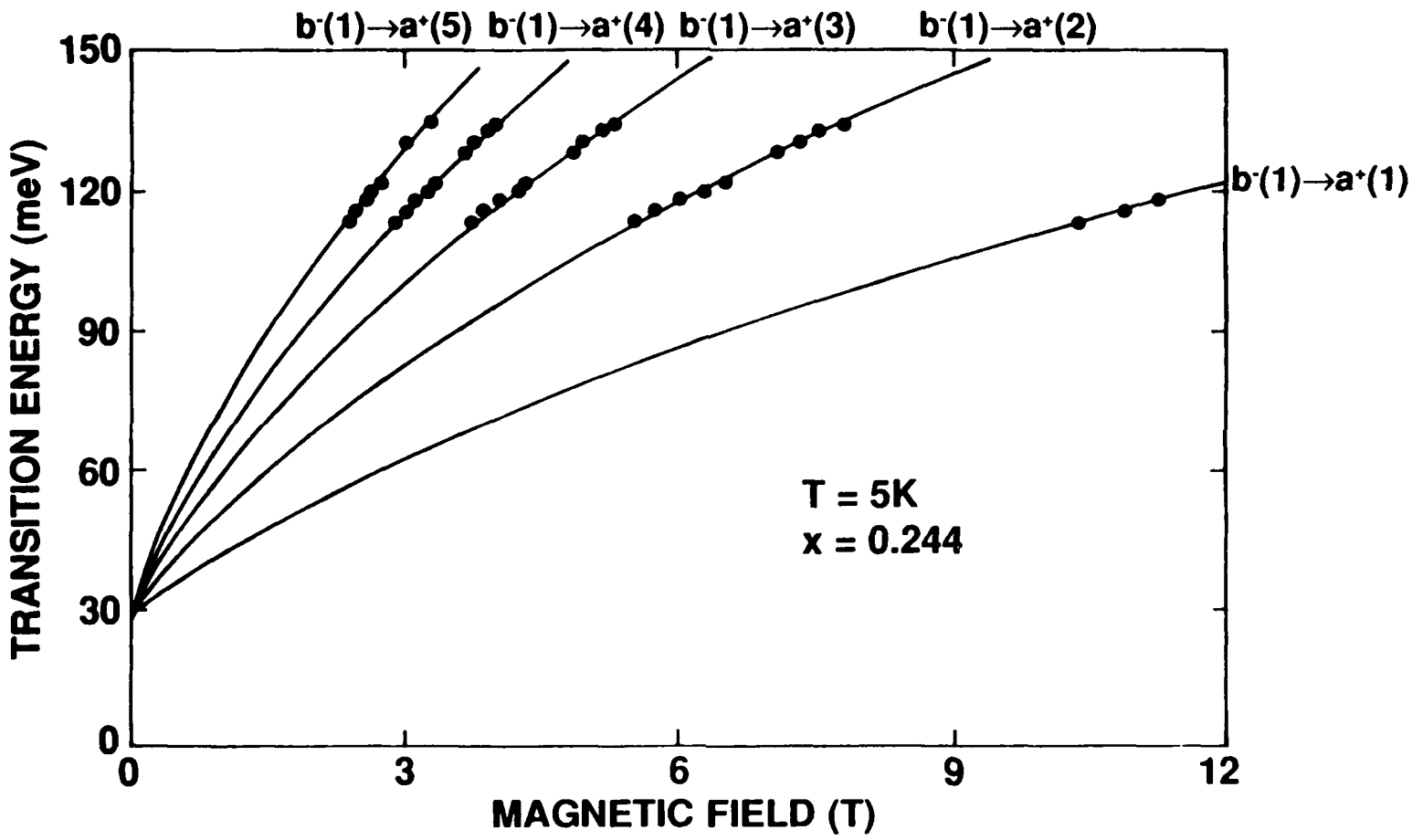

Figure 42. Comparison of experimental data (solid dots) and predictions of theory (solid lines). The zero-field intercept of $\simeq$ 30 meV is equal to twice the optic phonon energy.

References:

1. R. J. Justice, D. G. Seiler, W. Zawadzki, R. J. Koestner, M. W. Goodwin, and M. A. Kinch, J. Vac. Sci. Technol. A6, 2779 (1988).

2. R. J. Justice, D. G. Seiler, W. Zawadzki, R. J. Koestner, and M. W. Goodwin, Appl. Phys. Lett. 52, 1332 (1988).

3. M. H. Weiler, in Semiconductors and Semimetals (Academic Press, New York, 1981), R. K. Willardson and A. C. Beer, editors, Vol. 16, p. 119.

4. M. C. Chen and J. A. Dodge, Solid State Commun. 53, 449 (1986), and J. H. Tregilgas, J. Appl. Phys. 61, 727 (1987).

5. Y. Guldner, C. Rigaux, A. Mycielski and Y. Couder, Phys. Status Sol.(b) 81, 615 (1977).

6. Y. Guldner, C. Rigaux, A. Mycielski and Y. Couder, Phys. Status Sol.(b) 82, 149 (1977).

7. M. Dobrowolska, A. Mycielski, and W. Dobrowolski, Solid State Commun. 27, 1233(1978).

8. B. D. McCombe, R. J. Wagner, and G. A. Prinz, Phys. Rev. Lett. 25, 87 (1970).

9. B. D. McCombe, R. J. Wagner, and G. A. Prinz, Solid State Commun. 8, 1687 (1970).

10. T. J. Bridges, E. G. Burkhardt, and V. T. Nguyen, Optics Commun. 30, 66 (1979).

11. G. L. Hansen, J. L. Schmit and T. N. Casselman, J. Appl. Phys. 53, 7099 (1982).

12. Y. Nemirovsky and E. Finkman, J. Appl. Phys. 50, 8107 (1979).

13. J. Chu, S. Xu, and D. Tang, Appl. Phys. Lett. 43, 1064 (1983).

14. R. Legros and R. Triboulet, J. Crystal Growth 72, 264(1985).

15. J. C. Brice, "Properties of Mercury Cadmium Telluride," in EMIS DATAREVIEWS SERIES, No. 3 (INSPEC, 1987), p. 103.

16. J. L. Schmit and E.L. Stelzer, J. Appl. Phys. 40, 4865 (1969).

17. E. Popko and J.M. Pawlikowski, Phys. Status Sol.(a) 46, K9 (1978).

18. O. Caporaletti and G.M. Graham, Appl. Phys. Lett. 39, 338 (1981).

19. C. D. Thurmond, J. Electrochem. Soc.: Solid-State Science and Technology, 122, 1133 (1975).

20. J. Reif, in Fundamentals of Statistical and Thermal Physics, (McGraw-Hill, New York, 1965).

21. C.T. Elliott, I. Melngailis, T.C. Harman and A.G. Foyt, J. Phys. Chem. Solids. 33, 1527 (1972).

22. M. G. Andrukhiv, V. A. Maltseva, V. I. Ivanov-Omskii, V. K. Ogoroanikov, and T. S. Totieva, Sov. Phys. Semicond. 13, 210 (1979).

23. D. L. Polla and C. E. Jones, Solid-State Commun. **36**, 809 (1980).

24. D. L. Polla and C. E. Jones, J. Appl. Phys. **51**, 6233 (1980).

25. A. T. Hunter, D. L. Smith, and T. C. McGill, Appl. Phys. Lett. **37**, 200 (1980).

26. C. E. Jones, V. Nair, and D. L. Polla, Appl. Phys. Lett. **39**, 248 (1981).

27. D. L. Polla and C.E. Jones, J. Appl. Phys. **52**, 5118 (1981).

28. D. L. Polla, M. B. Reine, and C. E. Jones, J. Appl. Phys. **52**, 5132 (1981).

29. D. L. Polla, S. P. Tobin, M. B. Reine, and A. K. Sood J. Appl.Phys. **52**, 5182 (1981).

30. B. L. Gelmont, V. I. Ivanov-Omskii, V. A. Maltseva, and V. A. Smirnov, Sov. Phys. Semicond. **15**, 638 (1981).

31. C. E. Jones, V. Nair, J. Lindquist, and D. L. Polla, J. Vac. Sci. Technol. **21**, 187 (1982).

32. A. T. Hunter and T. C. McGill, J. Vac. Sci. Technol. **21**, 205 (1982).

33. R. G. Pratt, J. Hewett, P. Capper, C. L. Jones, and M. J. Quelch, J. Appl. Phys. **54**, 5152 (1983).

34. C. A. Merilainen and C. E. Jones, J. Vac. Sci. Technol. **A1**, 1637 (1983).

35. D. L. Polla and R. J. Aggarwal, Appl. Phys. Lett. **44**775 (1984).

36. C. E. Jones, K. James, J. Merz, R. Braunstein, M. Burd, M. Eetemadi, S. Hutton, and J. Drumheller, J. Vac. Sci. Technol. **A3**, 131 (1985).

37. S. E. Schacham and E. Finkman, J. Appl. Phys. **57**, 2001 (1985).

38. V. A. Cotton, J. A. Wilson, and C. E. Jones, J. Appl. Phys. **58**, 2208 (1985).

39. E. Finkman and Y. Nemirovsky, J. Appl. Phys. **59**, 1205 (1986).

40. F. J. Bartoli, C. A. Hoffman, and J. R. Meyer, J. Vac. Sci. Technol. **A4**, 2047 (1986).

41. R. G. Pratt, J. Hewett, P. Capper, C. L. Jones, and N. Judd, J. Appl. Phys. **60**, 2377 (1986).

42. M. C. Chen and J. A. Dodge, Solid State Commun. **53**, 449 (1986).

43. D. E. Lacklison, and P. Capper, Semiconductor Sci. Technol. **2**, 33 (1987).

44. M. C. Chen and J. H. Tregilgas, J. Appl. Phys. **61**, 787 (1987).

45. D. G. Seiler, C. L. Littler, M. R. Loloee, and S. A. Milazzo, J. Vac. Technol. **A7**, 370 (1989).

46. D. G. Seiler, M. R. Loloee, S. A. Milazzo, A. J. Durkin, and C. L. Littler, Solid State Commun. **69**, 757 (1989).

47. L. Eaves and J. C. Portal, J. Phys. C: Solid State Physics 12, 2809 (1979).

48. R. Dornhaus and G. Nimtz, in "Narrow-Gap Semiconductors," edited by G. Höhler (Springer-Verlag, New York, 1985), p. 248.

Table I

Sample Properties and Magneto-Optical Results

Sample	n (77K) (cm^{-3})	μ (77K) (cm^2/V-s)	E_g (7K) (meV)	X-value	E_1 (meV)	E_2 (meV)	E_3 (meV)
1	$\simeq 5x10^{14}$	$\simeq 1x10^5$	80.0	0.217	7.0	-	-
2	$\simeq 5x10^{14}$	$\simeq 1x10^5$	99.0	0.225	-	18.0, 26.0	-
3	$3x10^{14}$	$1.5x10^5$	104.0	0.225	7.0	-	-
4	$1.4x10^{14}$	$1.6x10^5$	122.0	0.239	9.8	-	-
5	$2.8x10^{14}$	$1.2x10^5$	125.0	0.241	10.0	-	60.0
6	$\simeq 5x10^{14}$	$\simeq 1x10^5$	136.0	0.246	-	-	63.0, 68.0
7	$\simeq 5x10^{14}$	$\simeq 1x10^5$	136.0	0.246	10.2	-	-
8	$3.0x10^{14}$	$1.3x10^5$	146.0	0.253	-	-	-
9	$1.0x10^{14}$	$7.6x10^4$	156.0	0.259	-	-	-
10	$1.4x10^{14}$	$6.5x10^4$	188.0	0.278	-	-	90.0, 94.0
11	$3.5x10^{14}$	$4.3x10^5$	222.0	0.296	-		111.5, 116.0
12	$9.9x10^{13}$	$5.3x10^4$	225.0	0.300	-	-	-

Table II

One- and Two-Photon Magnetoabsorption Transition Assignments

Designation	Energy-level transition	Polarization
K_1	$a^-(-1) \rightarrow a^c(0)$	σ_L
K_2	$b^+(-1) \rightarrow b^c(0)$	σ_L
K_3	$a^-(0) \rightarrow a^c(1)$	σ_L
K_4	$b^-(0) \rightarrow b^c(1)$	σ_L
K_5	$a^+(1) \rightarrow a^c(2)$	σ_L
L_1	$a^+(-1) \rightarrow a^c(1)$	σ_L
L_2	$b^+(-1) \rightarrow b^c(1)$	σ_L
L_3	$a^+(0) \rightarrow a^c(2)$	σ_L
L_4	$b^+(0) \rightarrow b^c(2)$	σ_L
L_5	$a^+(1) \rightarrow a^c(3)$	σ_L
L_6	$b^+(1) \rightarrow b^c(3)$	σ_L
R_1	$a^-(2) \rightarrow a^c(0)$	σ_R
R_2	$b^-(2) \rightarrow b^c(0)$	σ_R
R_3	$a^-(3) \rightarrow a^c(1)$	σ_R
R_4	$b^-(3) \rightarrow b^c(1)$	σ_R
R_5	$a^-(4) \rightarrow a^c(2)$	σ_R

Table III. Low Temperature Magneto-Optical Derived Values of $E_g(x)$.

Various magneto-optical techniques used include (1) IMA - interband magnetoabsorption, (2) ESR - electron spin resonance, (3) CCCPR - cyclotron, combined and cyclotron phonon resonances, (4) four-photon mixing, and (5) TPMA - two-photon magnetoabsorption.

x value	E_g (meV)	Magneto-Optical Technique Used	Reference	Comments
0	-299.7 ± 0.5	IMA	Dobrowolska et al (1978)	at 8K
0.01 0.025 0.05 0.105 0.115 0.15 0.185 0.215 0.25 0.28	-285 -261 -207 -110 - 90 - 30 35 86 161 208	IMA	Guldner et al (1977a,b)	at 4K
0.193	56	ESR	McCombe et al (1970)	at 4K
0.203	64 ± 3	CCCPR	McCombe et al (1970)	at 4K
0.234	119	FOUR PHOTON MIXING (ESR)	Bridges et al (1979)	at 4K
0.239 0.259 ± 0.0015 0.277 ± 0.001 0.300 ± 0.0035	122 ± 1 158.5 ± 1 195 ± 1 224 ± 2	TPMA	Present work	at 2-10K

TABLE IV

Summary of Impurity/Defect levels for HgCdTe

Year	Technique	Type	X-value	E_1 (meV) (shallow)	E_2 (meV) ($E_g/4$)	E_3 (meV) ($E_g/2$)	E_4 (meV) ($3E_g/4$)	Reference
1972	Hall,PL	p	0.26	15,16	-	-	-	Elliott (21)
			0.31	22,-	-	-	-	
			0.33	18,13	-	-	-	
			0.34	19,10	-	-	-	
1979	Lifetime,PL	n	0.3	18	70	-	-	Andrukhiv (22)
1980	DLTS	p	0.21	-	-	35,43	-	Polla (23)
1980	AS	diode	0.22	-	-	46	-	Polla (24)
			0.31	-	-	160	-	
1980	PL	n	0.32	14 ± 1.5	-	-	-	Hunter (25)
			0.48	4.5 ± 2, 15.5 ± 2	-	-	-	
1981	DLTS	p	0.21	-	43	-	-	Jones (26)
			0.39	-	118	283	-	
1981	DLTS, AS	p	0.207	-	-	37,44	-	Polla (27)
			0.215	-	-	35,46	-	
			0.271	-	-	70,81 -	-	
			0.285	-	-	81,92	-	
			0.305	-	-	161	208	
			0.320	-	-	-	206,218	
1981	DLTS	p	0.215	-	-	35,43	-	Polla (28)
			0.305	-	-	-	181,208	
			0.320	-	-	-	206,218	
1981	Lifetime	p	0.215	-	-	56	-	Polla (29)
			0.220	-	37	-	-	
			0.326	-	-	150	-	
			0.386	-	-	230	-	
			0.390	-	-	248	-	
1981	PL	n	0.3	10	-	-	-	Gelmont (30)

Year	Technique	Type	X-value	E_1 (meV) (shallow)	E_2 (meV) ($E_g/4$)	E_3 (meV) ($E_g/2$)	E_4 (meV) ($3E_g/4$)	Reference
1982	DLTS	n	0.27	-	-	136	-	Jones (31)
		p	0.39	-	70	150	-	
1982	PL	n	0.32	14 ± 1	-	-	-	Hunter (32)
			0.48	15.5 ± 2	-	-	-	
1983	Lifetime	n	0.307	-	-	-	223	Pratt (33)
			0.332	-	-	-	271	
			0.344	-	-	-	284	
			0.352	12	-	-	-	
			0.335	30	-	-	-	
1983	DLTS	p	0.48	-	140	200 230		Merilainen (34)
1984	PL	p	0.320	-	-	$.4E_g$	-	Polla (35)
		n	0.340	-	-	$.4E_g$	-	
1985	EPR	p	0.3	10	50	-	-	Jones (36)
1985	Lifetime	p	0.215	15	-	- -		Schacham (37)
			0.225	15	-	-		
			0.29	20	-	-		
1985	DLTS	n	.3	-	79	120	172	Cotton (38)
1986	Halldata	p	0.22	5,12.5	-	-	-	Finkman (39)
1986	PhotoHall	p	0.224	7	-	$E_g/2$	-	Bartoli (40)
1986	Lifetime	n	0.230	10 ± 2	-	-	-	Pratt (41)
			0.234	-	-	65 ± 5	-	
			0.245	-	-	-	124	
			0.31	-	-	-	200,232	
			0.32	-	-	-	233,253	
			0.33	15 ± 5	70 ± 7	-	-	
1986	Halldata	p	0.22	11	-	-	-	Chen (42)
1987	Lifetime	p	0.24	-	-	-	92	Lacklison (43)
1987	Halldata	p	0.2	11.5	-	-	-	Chen (44)
1988	MOS	n	0.23	10	-	-	-	Seiler(45,46)
			0.25	9.8	-	-	-	
			0.28	-	-	94,100	-	

APPENDIX

Reprints of publications from the work produced for this CCNVEO contract. They are appended in the following order.

1. "New Methods of Characterizing Majority and Minority Carriers in Semiconductors," Applied Physics Letters 51, 1916 (1987).

2. "Determination of Minority-Carrier Lifetimes in p-type Narrow Band-Gap Semiconductors with Two-Photon Absorption Excitation," Applied Physics Letters 53, 2188 (1988).

3. "New Laser-Based Magneto-Optical Studies of HgCdTe Alloys," Solid State Communications 69 (1989).

4. "Non-Linear Magneto-Optical Spectroscopy of HgCdTe by Two-Photon Absorption Techniques," Journal of Vacuum Science and Technology A7, 370 (1989).

5. "Magneto-Optical Investigation of Impurity and Defect Levels in HgCdTe Alloys," Journal of Vacuun Science and Technology A8, 1133 (1990).

6. "Temperature and Composition Dependence of the Energy Gap of HgCdTe by Two-Photon Magnetoabsorption Techniques," Journal of Vacuum Science and Technology A8, 1237 (1990).

New method of characterizing majority and minority carriers in semiconductors

D. L. Leslie-Pelecky, D. G. Seiler, and M. R. Loloee
Center for Applied Quantum Electronics, Department of Physics, North Texas State University, Denton, Texas 76203

C. L. Littler
Central Research Laboratories, Texas Instruments, Inc., Dallas, Texas 75265

(Received 13 July 1987; accepted for publication 5 October 1987)

A novel characterization method using magnetoconductivity tensor components to determine the carrier concentration and mobility of majority and minority carriers is presented. Results are given for bulk n-HgCdTe (one carrier), liquid phase epitaxial n-HgCdTe (two carriers), and p-InSb (two or three carriers). Advantages of this method over the standard Hall coefficient analysis are discussed.

Advances in the improvement and application of new semiconducting materials (the use of HgCdTe in infrared detectors, for example) have necessitated an increased interest in the properties of minority carriers. Although Hall coefficient (R_H) and magnetoresistance measurements have historically been used to characterize semiconductors by determining the carrier concentration (n), mobility (μ), and relaxation time (τ) of the majority carriers, the form of the multicarrier Hall coefficient makes detailed information about minority carriers difficult to obtain. In this letter, we show that the complete magnetic field dependence of the magnetoconductivity provides more information than the traditional R_H measurement and analysis, allowing us to determine n, μ, and τ for all carriers. Magnetoconductivity tensor components, which have the distinct advantage of being additive in the case of more than one carrier, have previously been used to characterize metals.[1-3] We demonstrate the power and ease of this method through application to bulk n-type $Hg_{1-x}Cd_xTe$ (one carrier conduction), n-type liquid phase epitaxial (LPE) HgCdTe (two carriers), and p-type InSb (two-carrier conduction at low temperatures and three-carrier conduction at temperatures $\simeq 125$–140 K).

The solution of the Boltzmann equation using a relaxation time approximation (RTA) has been detailed by Beer and others.[4-6] By finding the current density in terms of the electric field, the conductivity tensor may be identified. For a sample in the standard Hall configuration ($\mathbf{H} = H\hat{z}$), the conductivity tensor components may be written:

$$\sigma_{xx} = \frac{\rho_{xx}}{\rho_{xx}^2 + R_H^2 H^2} \simeq \sum_{i=1}^{M} \frac{n_i |e| H_i}{H_i^2 + H^2}, \tag{1a}$$

$$\sigma_{xy} = \frac{R_H H}{\rho_{xx}^2 + R_H^2 H^2} \simeq \sum_{i=1}^{M} \frac{n_i e H}{H_i^2 + H^2}, \tag{1b}$$

where ρ_{xx} and R_H are the standard measured quantities of transverse magnetoresistance and Hall coefficient, respectively, M is the number of carrier types, the critical magnetic field $H_i \simeq 1/\mu_i = m^*/\tau_i e$, in which μ_i and τ_i are average quantities.[7] n_i is the concentration of carriers of type i and $e < 0$ for electrons. The applicability of the relaxation time approximation (RTA) to our mobility considerations might be questioned, since optical phonon scattering (inherently inelastic) is one of the dominant modes in compound semiconductors.[8] However, as shown by Pfeffer and Zawadzki[9] for InSb at room temperature, the variational mobility calculation for optic phonon scattering gives almost the same result as the RTA. As the temperature is lowered, the RTA becomes progressively less and less valid, but also the optic phonon contribution to the mobility becomes less important. For example, at 77 K and an electron concentration of 10^{16} cm^{-3}, the experimental mobility of electrons in n-InSb is 10^5 cm^2/V s, (Ref. 8) while the optic phonon contribution is 1.5×10^6 cm^2/V s.[9] The elastic modes of scattering by ionized impurity and acoustic phonons can be treated by RTA. Thus, within the above approximations, the calculated individual relaxation times have physical meaning.

Note that σ_{xx} is positive for all carriers, while σ_{xy} will be negative for electron conduction and positive for hole conduction. Because of the differences in sign, we choose to fit σ_{xy} data, as differences in types of carriers become obvious upon plotting the experimental data. For σ_{xy}, the maximum value occurs when $H = H_i$ and is proportional to n_i ($\sigma_{xy} = n_i e/2H_i$). Because of the simple algebraic form of Eq. (1b) and the ease with which partial derivatives are taken, any nonlinear least-squares fit is sufficient for fitting Eq. (1b) to the experimental σ_{xy} data as determined from the right-hand side of Eq. (1b).

Figure 1 shows σ_{xy} vs ln H at 77 K for a bulk n-type $Hg_{1-x}Cd_xTe$ sample, grown by the solid-state recrystallization method ($x \simeq 0.23$). The negative values of σ_{xy} indicate that conduction occurs by electrons. From the form of Eq. (1b), where $M = 1$, we see that the (x,y) coordinate describing the peak of the curve corresponds to the pair

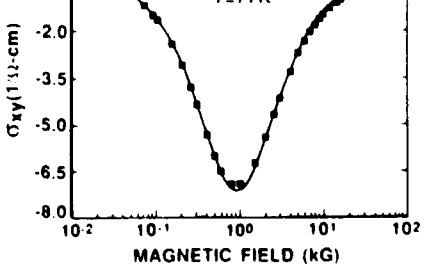

FIG. 1 σ_{xy} vs ln H for n-type HgCdTe at 77 K.

 © 1987 American Institute of Physics

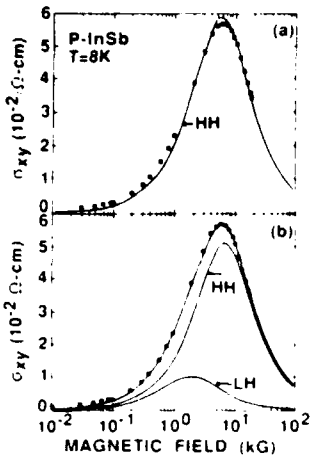

FIG. 2. (a) and (b) p-type InSb at 8 K: A simple, one-carrier Hall coefficient analysis finds 7.04×10^{11} carriers/cm^3 with mobilities of 1.51×10^4 cm^2/V s at $B = 1$ kG and 7.6×10^{11} carriers/cm^3 with mobility of 1.40×10^4 cm^2/V s at $B = 19$ kG. Note that there is negligible magnetic carrier freeze-out at these low fields (see Fig. 3 also).

$[H_t, \sigma_{xy}(\max)]$. The coordinates of the peak therefore provide initial guesses for parameters in the curve fitting program. Using a standard nonlinear least-squares fit to Eq. (1b), we find $n = 8.31\ (\pm 0.11)\times10^{14}$ cm^{-3} and $\mu = 1.08\ (\pm 0.12)\times10^5$ cm^2/V s. Taking $m^* = 0.01m_0$, $\tau = 6.14\ (\pm 0.68)\times10^{-13}$ s. The Hall coefficient (at $B = 1$ kG) yields $n = 8.83\times10^{14}$ cm^{-3}, $\mu = 1.07\times10^5$ cm^2/V s, and $\tau = 6.08\times10^{-13}$ s in good agreement.

Figures 2(a) and 2(b) show σ_{xy} vs $\ln H$ for a p-type InSb sample at 8 K. Figure 2(a) is an attempt to fit the data with a heavy-hole term only. Note that while the fit around the peak is satisfactory, the fit undercuts the data at low magnetic fields. In Fig. 2(b), both heavy- and light-hole carrier terms are included in order to accurately describe the data. By decomposing the fit into its constituent light- and heavy-hole terms, and identifying the peak coordinates, n, μ, and τ may be determined for each type of carrier. Table I summarizes the numerical data found from both fits. In order to calculate τ, the following effective mass values were used: m^*(light holes) $= 0.015m_0$ and m^*(heavy holes) $= 0.45m_0$.[10] Because the terms in the magnetoconductivity are additive, σ_{xy} plots yield much more information in the complex situations often encountered in the laboratory in terms of concentrations and types of carriers than

TABLE I. Summary of numerical data found by one-carrier and two-carrier fits of σ_{xy} data for p-type InSb at 8 K to Eq. (1b).

		Fig. 2(a) One-carrier fit	Fig. 2(b) Two-carrier fit
Light holes	p(cm^{-3})		$2.82(\pm0.06)\times10^{12}$
	μ(cm^2/V s)		$5.08(\pm0.46)\times10^4$
	τ(s)		$4.32(\pm0.39)\times10^{-13}$
Heavy holes	p(cm^{-3})	$4.23(\pm0.09)\times10^{11}$	$4.28(\pm0.05)\times10^{11}$
	μ(cm^2/V s)	$1.81(\pm0.36)\times10^4$	$1.48(\pm0.01)\times10^4$
	τ(s)	$4.62(\pm0.92)\times10^{-12}$	$3.79(\pm0.03)\times10^{-12}$
Standard deviation		8.20×10^{-5}	4.57×10^{-6}

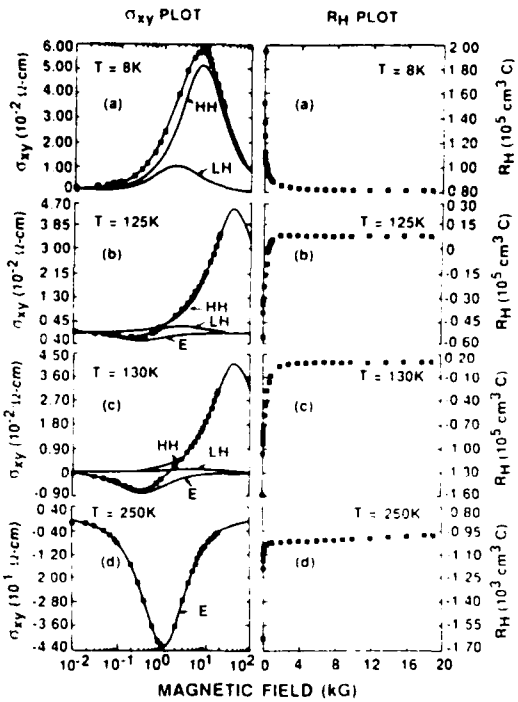

FIG. 3. Comparison of the Hall coefficient and σ_{xy} plots for p-type InSb for various temperatures (a) 8 K, (b) 125 K, (c) 130 K, (d) 250 K. Note the sensitivity of the σ_{xy} plot to small changes in temperature

do standard Hall coefficient plots. An example of this is seen in Fig. 3 where the σ_{xy} plots are compared with their corresponding Hall coefficient plots for a p-InSb sample for $T = 8$–250 K. The σ_{xy} curve at 8 K indicates that there are both light holes and heavy holes present, as discussed previously. In addition to the light and heavy holes already present, electronic contributions to conduction are apparent as σ_{xy} takes on negative values at low fields at 125 K. Note that the small concentrations of electrons present (on the order of 10^{11} cm^{-3}) relative to the concentration of heavy holes present (on the order of 10^{14}) are much more apparent in the σ_{xy} curve than in the corresponding Hall plot. At 130 K, a temperature change of only 5 K, the σ_{xy} curve has changed noticeably in both the height and critical magnetic field of the electron peak. Because of the large concentration of heavy holes and relatively small change in concentration of

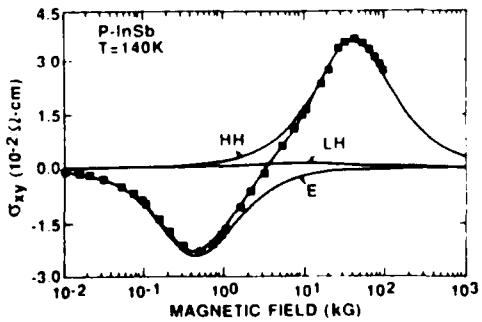

FIG. 4. Three-carrier fit of σ_{xy} data for p-type InSb at 125 K. Data taken at Francis Bitter National Magnet Lab.

TABLE II. Numerical data obtained by a three-carrier fit of σ_{xy} data for p-type InSb at 140 K

	Electrons	Heavy holes	Light holes
$n(\mathrm{cm}^{-3})$	$1.44(\pm 0.02)\times 10^{12}$	$1.75(\pm 0.02)\times 10^{14}$	$1.50(\pm 1.49)\times 10^{12}$
$\mu(\mathrm{cm}^2/\mathrm{V\,s})$	$2.18(\pm 0.28)\times 10^{5}$	$2.52(\pm 0.05)\times 10^{1}$	$1.14(\pm 0.69)\times 10^{4}$
$\tau(\mathrm{s})$	$5.57(\pm 0.72)\times 10^{-11}$	$6.44(\pm 0.13)\times 10^{-13}$	$2.91(\pm 1.76)\times 10^{-10}$

electrons, the Hall coefficient curve is not significantly changed. At 250 K, the conduction is mainly due to electrons as shown by the one carrier band fit. Overall, the σ_{xy} components, which can be easily decomposed, are much more illustrative in their description of transport properties than corresponding Hall coefficient plots.

Because of the low mobility of the predominant heavy holes, peaks in the σ_{xy} plots are not always possible to observe with low magnetic fields, thus making quantitative fitting difficult. Figure 4 shows the results of high field measurements made at the Francis Bitter National Magnet Laboratory on a p-type InSb sample at 140 K that quantitatively demonstrates the sensitivity of our technique. In this sample, we are able to quantitatively characterize light holes, heavy holes, and electrons. Numerical values are summarized in Table II. In calculating τ_i, we have used m^* (light holes) $= 0.015m_0$, m^* (heavy holes) $= 0.45m_0$, and m^*(electrons) $= 0.01m_0$.[10] We find that the value obtained through the fit for the concentration and mobility of light holes is very reasonable compared to the number and mobility of the heavy holes present.

Figures 5(a) and 5(b) show the application of this method to an epitaxially grown n-type LPE $Hg_{1-x}Cd_xTe$ sample ($x \simeq 0.23$) at 15 K. This sample exhibited anomalous transport properties, i.e., a low mobility at low temperatures and peaks in both the Hall coefficient and mobility versus temperature data. Figure 5(a) shows an attempt to describe the σ_{xy} data using one carrier (electron), as would be expected for n-type conduction. It is seen that the conduction mechanisms in this sample are more complicated, as evidenced by the inability of the one-carrier model to adequately describe the σ_{xy} data. Subsequent attempts using combined electron and hole conduction to describe the data were equally unsuccessful. Figure 5(b) shows, however, that the data can be satisfactorily explained by using two electrons of vastly different mobility and concentration. These values are given in the caption of Fig. 5. We note that two-electron conduction has been previously reported by Finkman and Nemirovsky in bulk n-type HgCdTe.[11] In addition, a previous study[12] on LPE HgCdTe invoked a model of p-type inclusions in an n-type matrix to describe the anomalous carrier transport properties. However, our σ_{xy} data show no evidence of holes contributing to conduction in these anomalous samples.

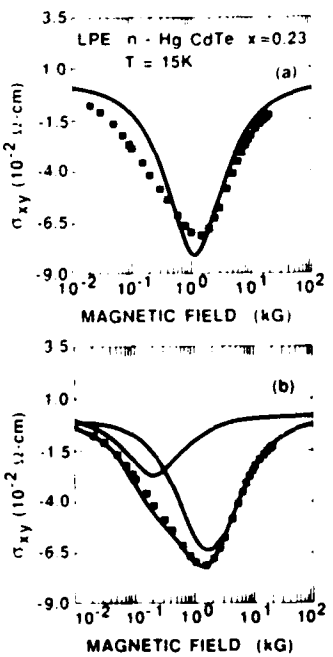

FIG. 5 (a) One-carrier fit. We find $1.16(\pm 0.08)\times 10^{11}$ cm^{-3} electrons with a mobility of $8.90(\pm 0.58)\times 10^4$ cm^2/V s. (b) Two-electron fit. We find $n_1 = 1.35(\pm 0.19)\times 10^{11}$ cm^{-3}, $\mu_1 = 5.98(\pm 0.14)\times 10^4$ cm^2/V s and $n_2 = 8.08(\pm 0.69)\times 10^{11}$ cm^{-3}, $\mu_2 = 4.43(\pm 0.23)\times 10^5$ cm^2/V s. The Hall coefficient finds 5.24×10^{11} carriers cm^{-3} with mobilities of 4.5×10^4 cm^2/V s at $B = 1$ kG and 1.71×10^{14} carriers cm^{-3} with mobilities of 1.4×10^5 cm^2/V s at $B = 10$ kG.

Because of its simplicity and sensitivity to minority carriers, we predict that magnetoconductivity tensor analysis will join Hall coefficient and magnetoresistance analysis as a standard characterization tool in the semiconductor industry, applicable not only to bulk materials, but also to thin films and the new generations of artificially structure materials.

We acknowledge the partial support of this work by Texas Instruments and a Faculty Research Grant from North Texas State University. We thank Dr. D. Weirauch for providing the LPE samples and Professor Wlodek Zawadzki for his helpful comments.

[1] G. G. Grenier, J. M. Reynolds, and J. R. Sybert, Phys. Rev. 132, 58 (1963).
[2] J. R. Sybert, H. J. Mackey, and K. L. Hathcox, Phys. Rev. 166, 710 (1968).
[3] J. W. McClure, Phys. Rev. 112, 715 (1958).
[4] A. C. Beer, *Galvanomagnetic Effects in Semiconductors* (Academic, New York, 1963).
[5] A. H. Wilson, *The Theory of Metals*, 2nd ed. (Cambridge University, Cambridge, 1953).
[6] B. R. Nag, *Electron Transport in Compound Semiconductors* (Springer, New York, 1980).
[7] Z. Dziuba and R. Kowalczyk, Phys. Status Solidi B 119, K11 (1983).
[8] W. Zawadzki, in *Handbook on Semiconductors*, edited by W. Paul (North-Holland, New York, 1982), Vol. 1, p. 713.
[9] P. Pfeffer and W. Zawadzki, Phys. Status Solidi B 88, 247 (1978).
[10] C. L. Littler, D. G. Seiler, R. Kaplan, and R. J. Wagner, Phys. Rev. B 27, 7473 (1983).
[11] E. Finkman and Y. Nemirovsky, J. Appl. Phys. 53, 1052 (1982).
[12] M. C. Chen, S. G. Parker, and D. F. Weirauch, J. Appl. Phys. 58, 3150 (1985).

Determination of minority-carrier lifetimes in p-type narrow band-gap semiconductors with two-photon absorption excitation

M. R. Loloee, D. G. Seiler,[a] and G. B. Ward
Center for Applied Quantum Electronics, Department of Physics, University of North Texas, Denton, Texas 76203

(Received 14 July 1988; accepted for publication 22 September 1988)

A novel method for the direct experimental determination of true minority-carrier (electron) lifetimes in p-type narrow band-gap semiconductors is presented. Specific results are given for p-InSb showing recombination involving a deep level close to midgap as the dominant recombination mechanism.

The minority-carrier lifetime is an important critical parameter in controlling the performance of infrared photodetectors based on narrow gap semiconductors like InSb or $Hg_{1-x}Cd_xTe$ alloys. In many cases, the minority-carrier lifetime τ is limited by deep levels of impurities or defects or traps that are present in the material, and hence a measurement of the temperature dependence of τ gives information about these levels. Determinations of τ usually rely on photoconductivity decay measurements and lasers with photon energies greater than the band gap of the material [e.g., GaAs diode lasers ($\lambda = 0.9\,\mu$m) or a HeNe laser ($\lambda = 3.39\,\mu$m)].[1-3] Unfortunately, the photoconductive decay can be complex showing multistage behavior leading to difficulties in extracting a true value for τ. Also, the large photon energies used means that surface effects can play a dominant and misleading role. In this letter, we show how to overcome these difficulties by using (1) a new method—the magneto-photoconductivity (MPC) tensor component method and (2) two-photon absorption (TPA) techniques. Results for high quality samples of p-InSb are reported here (electrons are the minority carriers) and are in reasonable agreement with earlier photoelectromagnetic effect studies.[4-8]

We have recently reported the development of a novel characterization method to determine the carrier concentration and mobility of majority and minority carriers in multicarrier systems using magnetoconductivity tensor (MCT) components.[9] The magnetoconductivity tensor components may be written as:

$$\sigma_{xx} = \frac{\rho_{xx}}{\rho_{xx}^2 + R_H^2 H^2} \simeq \sum_{i=1}^{M} \frac{n_i |e| H_i}{H_i^2 + H^2} \qquad (1a)$$

and

$$\sigma_{xy} = \frac{R_H H}{\rho_{xx}^2 + R_H^2 H^2} \simeq \sum_{i=1}^{M} \frac{n_i e H}{H_i^2 + H^2}, \qquad (1b)$$

where ρ_{xx} and R_H are the standard measured quantities of transverse magnetoresistance and Hall coefficient, respectively, M is the number of carrier types, $H_i \simeq 1/\mu_i = m^* \tau_i e$ is the critical magnetic field in which μ_i and τ_i are average quantities, and n_i is the concentration of carriers of type i ($e < 0$ for electrons). Although this method was applied to multicarrier analysis of dark thermal equilibrium carriers, it is also applicable to analyzing and studying photoexcited carriers under laser excitation conditions. This permits the extraction of true minority-carrier lifetimes in p-type semiconductors as opposed to the often ambiguous results obtained by photoconductivity techniques.

The samples used were cut from bulk grown p-type InSb having a concentration of 1.7×10^{14} cm^{-3} and a Hall mobility of 1.2×10^4 cm^2/V s at 77 K. The resistivity and Hall contacts were made in a standard configuration to simultaneously measure both the photoconductive (PC) and photo-Hall (PH) responses. CO_2 laser pulses were obtained from a rotating mirror Q-switch arrangement that could provide high intensities (up to 500 kW/cm^2) and had full width at half maximum pulse widths of $\simeq 98$ ns. The laser pulses were focused onto the region of the sample between the potential contacts and a separate pair of Hall contacts. The magneto-photoconductive and photo-Hall transient responses were captured by a Tektronix transient digitizer. Time-resolved PC measurements were taken in order to compare with the results obtained from MPC study. The PC response for different temperatures is shown in Fig. 1 for $\lambda = 9.25\,\mu$m and $I = 50$ kW/cm^2. The PC response has a single exponential decay for $30 < T < 100$ K and two stages of decay at $T < 30$ K or $T > 100$ K. At 9.25 μm ($2\hbar\omega = 267.9$ meV), TPA effects occur at all temperatures since $2\hbar\omega > E_g$, the energy gap; however, the recombination mechanisms controlling the PC response are very complex, as seen in Fig. 1. In Fig. 2 we

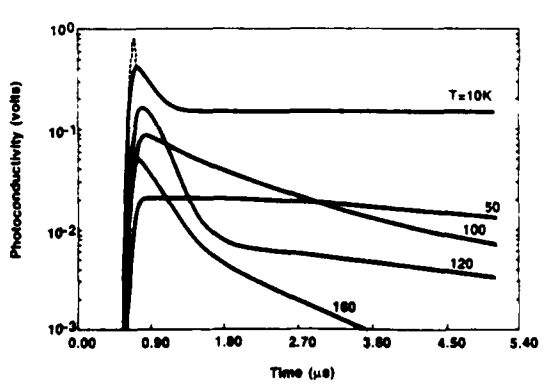

FIG. 1. Temperature dependence of the ac photoconductive response obtained for $\lambda = 9.25\,\mu$m and $I = 50$ kW/cm^2. The waveforms have two stages of decay for $T < 30$ K and $T > 110$ K. The dashed line represents the laser pulse.

[a] Current address: National Institute of Standards and Technology, Materials Technology Group, Semiconductor Electronics Division, Center for Electronics and Electrical Engineering, Gaithersburg, MD 20899.

 © 1988 American Institute of Physics

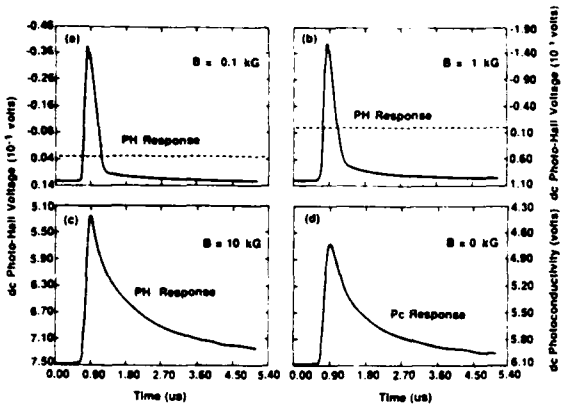

FIG. 2. Time-resolved dc PH and PC responses for $T = 100$ K. (a) and (b) show the PH response at $B = 0.1$ and 1 kG, whereas (c) and (d) show the similarity of the PH response at $B = 10$ kG with the PC response at $B = 0$.

show that at low magnetic field strengths the PH response behaves differently from the PC response and thus contains additional information about recombination mechanisms, if it can be properly analyzed. In Figs. 2(a) and 2(b) the dc PH response is plotted for $B = 0.1$ and 1 kG. Note that for this low field region, the PH response has negative values over part of the waveform when the laser pulse is incident on the sample. Since $R_H > 0$ implies hole domination and $R_H < 0$ electron domination, the switch over from positive R_H values in the dark to negative R_H values (as seen by the negative Hall voltages) when laser light is incident on the sample implies photoexcited electrons are observed. Figures 2(c) and 2(d) show the similarity of the PH response at $B = 10$ kG and the PC response, respectively, where no negative voltage (photoexcited electron contribution) was observed in the PH response. In order to unravel this complex behavior, we now show how the MCT component method can be used to great advantage. The dark σ_{xy} data in Fig. 3 were obtained for four different temperatures by our recently reported method.[9] By using a standard nonlinear least-squares fitting method with Eq. (1b), we are able to separate multicarrier components as well as collecting numerical data on individual carrier concentrations and mobilities. Fc 77 and 100 K, only heavy holes and light holes are present, while for $T = 135$ K, the presence of as few as 5.3×10^{11} cm⁻³ minority-carrier electrons (thermally excited across th band gap) can be seen. For $T = 160$ K, 2.6×10^{13} cm⁻³ intrinsic electrons thermally excited across the gap totally dominate the transport at low magnetic fields.

Laser excitation with a CO_2 laser pulse ($\lambda = 9.25\ \mu$m creates a uniform distribution of electron-hole pairs by TPA processes. Minority-carrier electrons can thus be observe and studied. (Note that for $T > 50$ K, TPA occurs over th 9–10 μm range.) Figure 4 shows the results of our TPA photoexcitation studies. The $T = 50$ K plots of σ_{xy} versus magnetic field in Fig. 4(a) show four sets of data with the retical curves: (1) in the dark, at a time before the laser puls is incident on the sample, (2) at the peak of the signal, 325 ns after the start of the laser pulse, (3) 435 ns after, and (4) 51 ns after. The peak of the signal occurs at the end of the lase pulse. Figures 4(b) and 4(c) are the results of nonlinear least-squares fitting in which we find, in the dark, $p(\text{heavy}) = 1.2 \times 10^{14}$ cm⁻³ with $\mu = 2.2 \times 10^4$ cm²/V and $p(\text{light}) = 1.1 \times 10^{12}$ cm⁻³ with $\mu = 1.7 \times 10^5$ cm²/V Under irradiation of intensity $I = 50$ kW/cm², the number of photoexcited electron minority carriers is $n = 3.7 \times 10$ cm⁻³ with $\mu = 1.6 \times 10^4$ cm²/V s. These novel measur ments and analysis thus provide directly the number of photoexcited minority carriers (electrons in the conduction band) Δn as a function of time. In Fig. 5 we show the numb of photoexcited electrons Δn versus time for $T = 100$ an 160 K by using the MPC technique. Note that the technique is extremely sensitive to the number of minority-carrier ele trons $= 4.5 \times 10^{10}$ cm⁻³ photoexcited electrons on a back ground of 1.7×10^{14} cm⁻³ holes at $T = 100$ K. For comparison purposes, we also plot the time variation of the PC response which possesses a single-stage decay for $T = 100$ I and a two-stage decay for $T = 160$ K. This semilog plot a. lows the extraction of an electron lifetime $\tau_n = 88$ ns at $T = 100$, which is much shorter than the lifetime implied b the PC response. At $T = 160$ K, $\tau_n = 356$ ns and the tim dependence of the photoexcited minority-carrier concentration follows the first (short) stage of the PC response. We

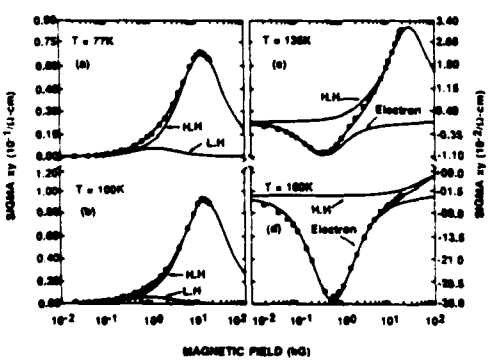

FIG. 3. σ_{xy} vs ln H plots in the dark for various temperatures: (a) 77 K, (b) 110 K, (c) 135 K, and (d) 160 K. The sensitivity of the σ_{xy} component to small changes in temperature is readily apparent in the figures.

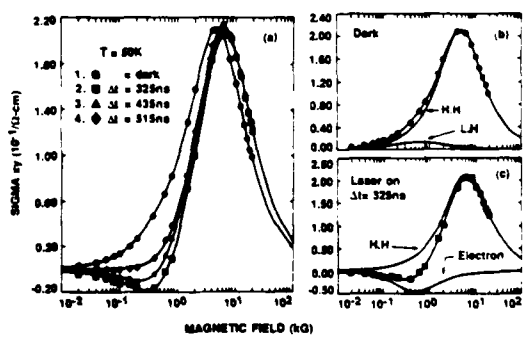

FIG. 4. (a) Time-resolved σ_{xy} data for $T = 50$ K showing the creation photoexcited electrons in the conduction band via TPA processes. (Dark, (2) 325 ns after the start of the laser pulse, (3) 435 ns after and (4) 515 ns after. (b) and (c) show two-carrier fits of σ_{xy} data in the dark and 325 ns after the start of the laser pulse.

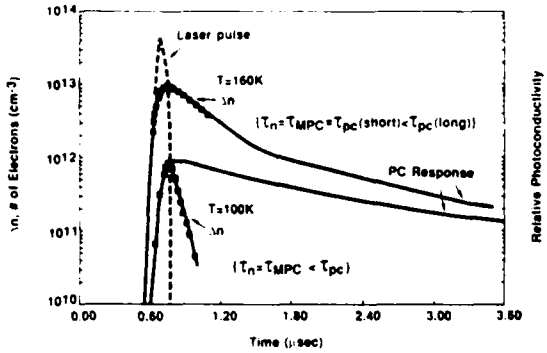

FIG. 5. Time dependence of minority electron concentration (Δn) obtained by the MPC technique for $T = 100$ and 160 K. For comparison purposes, solid lines show the actual PC response for each temperature.

also note that the magnitude of the PC response is much larger at 100 K than at 160 K. At 100 K, the PC response is dominated by impurity/defect absorption which creates only holes, which have a long lifetime. The presence of the much smaller quantity of minority-carrier electrons produced by TPA processes can only be detected by the much more sensitive MPC method presented here. At 160 K, impurity/defect absorption no longer dominates, $\Delta n \simeq \Delta p$, $\mu_e \gg \mu_p$, and hence the first-stage decay of the PC response is due to the decrease in the number of minority-carrier electrons, in agreement with the MPC method. For both cases at long times, all minority-carrier electrons are trapped, and the PC response is then controlled by hole recombination.

Comparison of the temperature dependence of the minority-carrier lifetime obtained from the MPC method and the lifetime obtained from the first-decay stage of the PC response is shown in Fig. 6. Assuming a single defect level in the energy gap, the minority-carrier lifetime dependence on temperature can be explained by a Shockley–Read lifetime dependence as[10]

$$\tau_{SR} = \tau_{p_0} \frac{(n_0 + n_1 + \delta_n)}{n_0 + p_0 + \delta_n} + \tau_{n_0} \frac{(p_0 + p_1 + \delta_p)}{n_0 + p_0 + \delta_n}, \quad (2)$$

where $\tau_{n_0} = (C_n N_t)^{-1}$ and $\tau_{p_0} = (C_p N_t)^{-1}$, N_t is the trap density, C_n and C_p are the electron and the hole capture coefficient, respectively, n_1 and p_1 are the carrier concentrations for a Fermi level coincident with the trap level and defined as

$$n_1 = n_0 \exp[(E_t - E_f)/kT], \quad (3a)$$

$$p_1 = p_0 \exp[(E_f - E_t)/kT]. \quad (3b)$$

In the simple case where $p_0 \gg n_0 \gg n_1$, $\tau_{p_0} \gg \tau_{n_0}$, $p_1 \gg p_0$, and small δ_n, δ_p one can write[1,2]

$$\tau_{SR} = \tau_{n_0}\left(1 + \frac{p_1}{p_0}\right) = \tau_{n_0}\left[1 + \exp\left(\frac{E_f - E_t}{kT}\right)\right]. \quad (4)$$

If the Fermi level falls below the level of the trap (at low temperatures), the lifetime is constant and equal to τ_{n_0}. However, for $E_f > E_t$, the lifetime increases exponentially with increasing temperature. The energy of the Shockley–Read defect level extracted from the data using Eq. (4), is 106 meV above the valence band for a midgap level which agrees closely with the results tabulated by Seiler and Goodwin in Table I.[11] In the absence of the trap level, $\tau_{MPC} = \tau_n = \tau_{pc}$, but the experimental inequality of τ_{MPC} and τ_{pc} for $T < 160$ K in Fig. 6 indicates that the analysis of the PC response cannot provide detailed information about minority-carrier electrons in p-type semiconductors.

In summary, we have shown that the magnetophotoconductivity tensor component method is appropriate for studying minority-carrier lifetimes and determining carrier concentrations and mobilities of minority and majority carriers in narrow gap semiconductors. Use of different lasers will, of course, allow wider band-gap semiconductors also to be investigated by this method. Our future work will concentrate on samples of $Hg_{1-x}Cd_xTe$.

We acknowledge the partial support of this work by the U.S. Army Center for Night Vision and Electro-Optics, contract DAAB07-87-C-F094, and a faculty research grant from the University of North Texas.

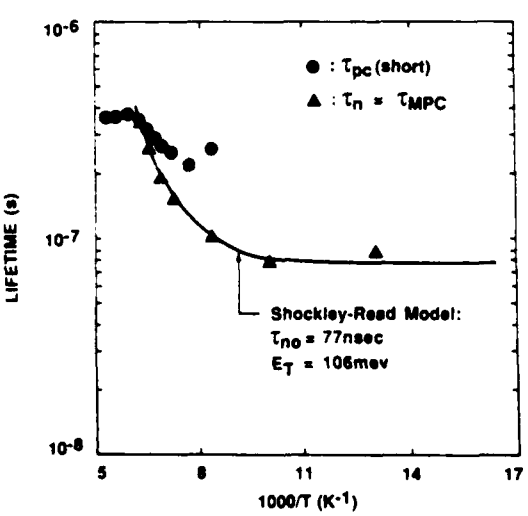

FIG. 6. Lifetime of minority electrons τ_n, and the first stage of the PC response τ_{pc} (short) for $T > 110$ K vs temperature. A trap energy of 106 meV is indicated by the fit to the Shockley–Read theory.

[1] D. L. Polla, S. P. Tobin, M. B. Reine, and A. K. Sood, J. Appl. Phys. 52, 5182 (1981).
[2] D. E. Lacklison and P. Capper, Semicond. Sci. Technol. 2, 33 (1987)
[3] S. E. Schacham and E. Finkman, J. Appl. Phys. 57, 2001 (1985).
[4] R. N. Zitter, A. J. Strauss, and A. e. Attard, Phys. Rev. 115, 266 (1959).
[5] R. A. Laff and H. Y. Fan, Phys. Rev. 121, 53 (1961).
[6] D. N. Nasledov and Yu S. Smetannikova, Sov. Phys. Solid State 4, 78 (1962).
[7] J. E. L. Hollis, S. C. Choo, and E. L. Heasell, J. Appl. Phys. 38, 1626 (1967).
[8] A. S. Volkov and V. V. Galavanov, Sov. Phys. Semicond. 1, 129 (1967).
[9] D. L. Leslie-Pelecky, D. G. Seiler, M. R. Loloee, and C. L. Littler, Appl. Phys. Lett. 51, 1916 (1987).
[10] W. Shockley and W. T. Read, Jr., Phys. Rev. 87, 835 (1952).
[11] D. G. Seiler and M. W. Goodwin, J. Appl. Phys. 53, 7505 (1982).

Solid State Communications, Vol. 69, No. 7, pp. 757–760, 1989.
Printed in Great Britain.

0038-1098 89 $3.00 + .00
Pergamon Press plc

NEW LASER-BASED MAGNETO-OPTICAL STUDIES OF $Hg_{1-x}Cd_xTe$ ALLOYS*

D.G. Seiler,† M.R. Loloee, S.A. Milazzo and A.J. Durkin

Center for Applied Quantum Electronics, Department of Physics, University of North Texas, P.O. Box 5368, Denton, Texas 76203, USA

and

C.L. Littler

Central Research Laboratories, Texas Instruments, Dallas, Texas 75265, USA

(*Received* 21 *October* 1988 *by J. Tauc*)

Several magneto-optical effects are observed for the first time in a number of $Hg_{1-x}Cd_xTe$ alloys. These include two-photon magneto-absorption and optical transitions from both shallow acceptor levels and midgap levels to the conduction band. These effects yield accurate information about the energy band structure, the temperature dependence of the energy gap, and the activation energies of impurity and defect states present in the $Hg_{1-x}Cd_xTe$ alloys.

DETECTORS fabricated using mercury cadmium telluride ($Hg_{1-x}Cd_xTe$) alloys serve as extremely important components of modern infrared systems. Improvements in the sensitivity and performance of these detectors require a better understanding of the detector material's optical and electronic properties, along with improved sample characterization techniques. Specifically, information about the energy band structure and impurity or defect levels present in $Hg_{1-x}Cd_xTe$ is essential to understanding and improving the performance of current infrared detectors. Consequently, it is highly desirable to develop and use new, sensitive techniques to aid in the characterization of these alloys.

In this paper we present new and important results on $Hg_{1-x}Cd_xTe$ alloys using CO_2 laser-based magneto-optical methods that include: (1) the first observation and analysis of two-photon magneto absorption (TPMA) spectra; (2) the first observation of magneto-optical transitions of electrons from both midgap levels and shallow acceptor levels to the conduction band; and (3) the first observation of magneto-impurity spectra. In addition, analysis of two-photon spectra obtained at low temperatures reveals a nonlinear variation of the energy gap versus temperature not previously reported. The laser based magneto-optical techniques we present here for $Hg_{1-x}Cd_xTe$ are generic and can easily be applied to other semiconductor or superlattice systems by using an appropriate combination of laser sources and magnetic fields.

The experiments reported here were carried out on single crystal, bulk grown *n*-type samples of $Hg_{1-x}Cd_xTe$ with $x = 0.236$, 0.256 and 0.280. All samples were polished, etched, and had indium contacts. They showed the normal temperature dependence of the Hall coefficient and resistivity. The output of a grating tunable cw CO_2 laser was mechanically chopped into 20 μs wide pulses which were focused onto the samples mounted in a superconducting magnet in a transverse magnetoresistance geometry.

Photoconductivity (PC) measurements were used since they have been shown [1–4] to provide a sensitive means of determining small changes in absorption due to weak magneto-optical transitions. Boxcar averager techniques were used to record the PC response of the samples vs magnetic field. An example of the PC spectra for several wavelengths is shown in Fig. 1 for a sample with $x = 0.236$. All of the observed resonant structure can be understood by a Landau-level and density-of-states model where peaks in the density-of-states occur at energies corresponding to the bottom of each Landau level. These peaks enhance the optical transition rates or the electron scattering rates. Optically created electrons in the conduction band then increase the conductivity or photoconductive response of the samples. Four different types of structure are observed depending upon which combination of laser

* Work at UNT supported in part by the U.S. Army Night Vision and Electro-Optics Center, Contract # DAA B07-87-C-F094.

† *Present address*: National Institute of Standards and Technology, Semiconductor Electronics Division, Gaithersburg, Maryland 20899, USA.

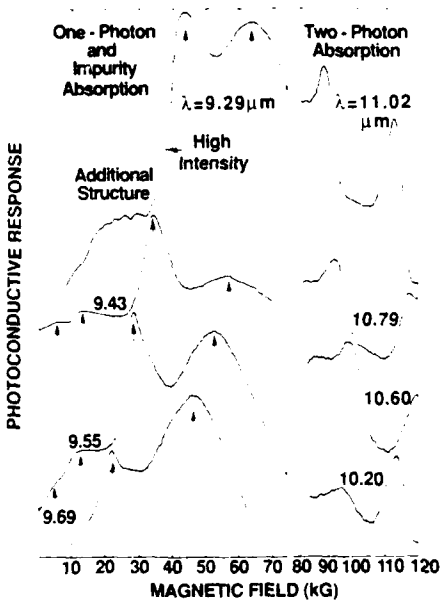

Fig. 1. Magneto optical spectra at various CO_2 laser wavelengths and magnetic fields in a sample of $Hg_{1-x}Cd_xTe$ with $x = 0.236$. At high fields and long wavelengths TPMA resonant structure is seen. At lower fields and lower wavelengths both one-photon magnetoabsorption (short arrows) and a much broader resonance (longer arrows) due to transitions from a shallow acceptor level to the conduction band are seen. Additional structure seen for $\lambda = 9.29\,\mu m$, whose resonant positions do not depend upon photon energy, arises from the magneto-impurity effect.

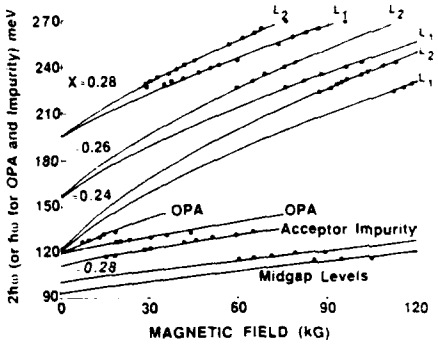

Fig. 2. Fan chart plots of either one-photon ($\hbar\omega$) or two-photon ($2\hbar\omega$) transition energies vs magnetic field for three $Hg_{1-x}Cd_xTe$ samples of different x-values. All lines represent theoretical calculations from a modified Pidgeon–Brown band model. The three pairs of transitions in the upper half arise from two-photon absorption where L_1 represents an $a^+(-1)$ to an $a^c(1)$ and L_2 a $b^+(-1)$ to a $b^c(1)$ transition. Here a, b denote different spin states of the Landau levels, the superscript (+) denotes a (light) hole state, and the superscript c, a conduction band Landau level. In addition to the OPA and TPA transition energies shown, the transition energies vs magnetic field for shallow impurity-to-conduction and midgap level-to-conduction band transitions are shown. The activation energies determined from the zero-field intercepts are 9.8 meV above the valence band for the shallow acceptor level present in the $x \cong 0.24$ sample and 94 and 100 meV below the conduction band for the $x \cong 0.28$ sample.

wavelength, magnetic field, and laser intensity is used. First, at high magnetic fields, long wavelengths, and high intensities, two strong PC resonances are observed. We have identified these resonances as resulting from specific two-photon interband transitions from initial valence band Landau levels to final conduction band Landau levels. Secondly, at shorter CO_2 wavelengths, smaller magnetic fields, and low laser intensities, one-photon interband transitions are seen as indicated by the short upward pointing arrows in Fig. 1. Just to the high field side of the largest one-photon absorption (OPA) peak is a broad resonance indicated by the long arrows. We identify this structure as resulting from electron transitions from a shallow acceptor to the lowest conduction band Landau level. The temperature dependence and time-resolved behavior of the PC response support this identification, as does the binding energy of 9.8 meV determined from the photon energy dependence presented in Fig. 2. We rule out bound excitons as a source of this resonance because the large width of the resonance (bound excitons produce a much narrower linewidth than do free excitons). We also note that the binding energy deduced from these experiments for the residual acceptor level in this n-type sample is consistent with that of either As [5], Cu [6, 7] or Sb [8] residual impurities previously determined in p-type samples. A major significance of the work presented here is that it provides a new means of determining the presence of compensating shallow acceptors in n-type material. Finally, at low fields, shorter wavelengths, and high intensities a new set of structure which is periodic in reciprocal magnetic field and which does not depend upon laser wavelength is observed. This is seen in Fig. 1 on the low field side of the large OPA peak for $\lambda = 9.29\,\mu m$. We attribute this structure to magneto-impurity resonances [9] which arise from inelastic scattering processes whereby free carriers resonantly exchange energy with a second carrier bound to a donor or acceptor impurity in the presence of a magnetic field. Hot-electron conditions are necessary for this observation and these conditions are achieved by the photoexcitation of carriers into the

conduction band by optical excitation across the band gap.

Theoretical calculations of transition energies vs field, shown in Fig. 2 for each magneto-optical effect discussed, are in excellent agreement with the data. The Landau level energies were calculated using a modified Pidgeon–Brown model and the set of band parameters given by Weiler [10]: $E_p = 19\,\text{eV}$, $\Delta = 1\,\text{eV}$, $\gamma_1 = 3.3$, $\gamma_2 = 0.1$, $\gamma_3 = 0.9$, $\kappa = -0.8$, $F = -0.8$, $q = 0.0$, and $N_1 = 0.0$. Using either one or two-photon selection rules the transition energies can be calculated for the pertinent OPA and TPA transitions. The value of E_g is easily determined by fitting theoretical results to the data using E_g as an adjustable parameter. Weiler has shown [10] that exciton corrections are necessary to adequately describe OPA data in $Hg_{1-x}Cd_xTe$. Since exciton corrections are not expected to be significant for TPA, we sought a consistent description of both the TPA and OPA data while correcting only the OPA data for excitonic effects. By using a free exciton binding energy of 2 meV, satisfactory agreement with the OPA data was achieved.

Two-photon magneto-optical methods are the best means for accurately determining the energy gap of a semiconductor. For example, the high quality of the TPMA data shown in Fig. 1 and the corresponding analysis gives $E_g = 121.8 \pm 0.5\,\text{meV}$. Using the Hansen, Schmit, Casselman relation [11] and this value for E_g, we find $x = 0.2360 \pm 0.0003$ for this sample. With this means to accurately determine E_g, we have measured the temperature dependence of E_g and found a nonlinear variation of E_g with T below 15 K, with E_g becoming independent of T.

We have observed TPA structure in a wide variety of samples with other x-values and even in p-type samples. Figure 3 shows results for samples with $x \cong 0.26$ and $x \cong 0.28$. The same two dominant TPA peaks seen in the $x \cong 0.24$ sample are also characteristic features of the spectra. Once again theoretical calculations of $2\hbar\omega$ vs B accurately describe these data as seen also in Fig. 2 with $E_g = 155\,\text{meV}$ and $E_g = 195\,\text{meV}$ for the two samples. In addition, polarization studies have been performed on the samples, verifying the σ_l selection rule dependence of this structure and thus confirming the TPA interpretation. Finally, a new feature is seen for $x \cong 0.28$ sample – at higher fields two new resonances occur which can not theoretically be described by TPA processes. We interpret these resonances as resulting from electron transitions to the conduction band from midgap impurity or defect levels known to be present in samples of $Hg_{1-x}Cd_xTe$ [12]. Electron transitions from the midgap levels to the lowest conduction band

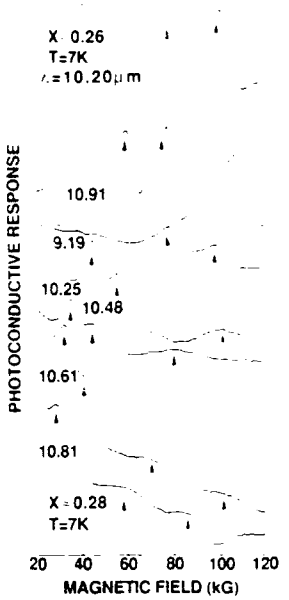

Fig. 3. Magneto-optical spectra in two samples of $Hg_{1-x}Cd_xTe$ with $x \approx 0.26$ and $x \approx 0.28$ showing TPA structure (short arrows) and midgap level to conduction band transitions (long arrows).

Landau level were calculated and plotted in Fig. 2, yielding activation energies of 100 meV and 94 meV below the conduction band edge.

In summary, we report the first observations and analysis of several different types of magneto-optical transitions in samples of $Hg_{1-x}Cd_xTe$. These transitions arise from (1) TPMA processes, (2) shallow acceptor to conduction band absorption, (3) midgap defect or impurity levels to conduction band absorption. This is the first time that these magneto-optical effects have been observed and studied in $Hg_{1-x}Cd_xTe$ alloys. In addition, magneto-impurity oscillations have been observed. The techniques presented here are accurate, convenient to use, and could be developed into routine tools for not only characterizing bulk samples of $Hg_{1-x}Cd_xTe$, but thin films and superlattices as well. These magneto-optical methods are completely general, and with appropriate choices of laser sources and magnetic fields, can be used to study a wide variety of semiconductor materials.

REFERENCES

1. D.G. Seiler, M.W. Goodwin & M.H. Weiler, *Phys. Rev.* **B23**, 6806 (1981).
2. M.W. Goodwin, D.G. Seiler & M.H. Weiler, *Phys. Rev.* **B25**, 6300 (1982).
3. D.G. Seiler & M.W. Goodwin, *J. Appl. Phys.* **53**, 7505 (1982).

4. D.G. Seiler, K.H. Littler & C.L. Littler, *Semicond. Sci. Technol.* **1**, 383 (1986).
5. M.H. Kalisher, *J. Crystal Growth* **70**, 369 (1984).
6. F.J. Bartoli, C.A. Hoffman & J.R. Meyer, *J. Vac. Sci. Technol.* **A4**, 2047 (1986).
7. M.C. Chen & J.H. Tregilgas, *J. Appl. Phys.* **61**, 787 (1987).
8. M.C. Chen & J.A. Dodge, *Solid State Commun.* **59**, 449 (1986).
9. See for example, L. Eaves & J.C. Portal, *J. Phys. C: Solid State Phys.* **12**, 2809 (1979).
10. M.H. Weiler, in *Semiconductors and Semimetals*, Vol. 16, p. 119 (Edited by R.K. Willardson and A.C. Beer), Academic Press, New York (1981).
11. G.L. Hansen, J.L. Schmit & T.N. Casselman, *J. Appl. Phys.* **53**, 7099 (1982).
12. M.C. Chen, M.W. Goodwin & T.L. Polgreen, *J. Crystal Growth* **86**, 484 (1988).

Nonlinear magneto-optical spectroscopy of $Hg_{1-x}Cd_xTe$ by two-photon absorption techniques

D. G. Seiler[a)]
Center for Applied Quantum Electronics, Department of Physics, University of North Texas, Denton, Texas 76203

C. L. Littler
Central Research Laboratories, Texas Instruments, Dallas, Texas 75265

M. R. Loloee and S. A. Milazzo
Center for Applied Quantum Electronics, Department of Physics, University of North Texas, Denton, Texas 76203

(Received 11 October 1988; accepted 8 November 1988)

In this paper we present new and important results on $Hg_{1-x}Cd_xTe$ alloys using CO_2 laser-based magneto-optical methods that include (i) the observation and analysis of two-photon magnetoabsorption spectra in a variety of samples from $x \simeq 0.24$ to 0.30, and (ii) the observation of magneto-optical transitions of electrons from both midgap levels and shallow acceptor levels to the conduction-band Landau levels. These measurements allow the most accurate determination of the energy gap and binding energies associated with impurities and defects. In addition, analysis of the temperature dependence of two-photon spectra obtained on all samples investigated reveals a nonlinear variation of the energy gap versus temperature not previously reported. The temperature dependence of the energy gap below 100 K cannot be explained by any of the currently used empirical relationships. The laser-based magneto-optical techniques we present here for $Hg_{1-x}Cd_xTe$ are generic and can easily be applied to other semiconductor or superlattice systems by using an appropriate combination of laser sources and magnetic fields.

I. INTRODUCTION AND BACKGROUND

Mercury cadmium telluride ($Hg_{1-x}Cd_xTe$) detectors serve as extremely important components of modern infrared detector systems. Improvements in sensitivity and performance require a better understanding of the alloy's optical and electronic properties, along with improved sample characterization techniques. New information about the energy-band structure and impurity or defect levels present in $Hg_{1-x}Cd_xTe$ is therefore essential to understanding and improving the performance of current infrared detectors along with the development of future novel devices. Consequently, it is highly desirable to develop and use new, sensitive techniques such as the magneto-optical ones reported here to aid in the characterization of these alloys.

Over the past several decades magneto-optical studies of semiconductors have proven capable of accurately determining energy-band parameters and impurity level information because of the optical transitions that occur between magnetically quantized electronic or impurity states. The use of lasers has now opened up the realm of nonlinear spectroscopy as a useful method for studying and characterizing semiconductors. Two-photon absorption (TPA) is one of the numerous nonlinear optical effects arising from χ^3, the electric susceptibility tensor of the third order. In a previous study,[1,2] we have shown that two-photon absorption techniques can be used to determine TPA cutoff wavelengths and carrier lifetimes for samples of n-$Hg_{1-x}Cd_xTe$ with $x \simeq 0.31$. In this paper we report extensive nonlinear magneto-optical results on $Hg_{1-x}Cd_xTe$ alloys using TPA techniques. Resonant two-photon magnetoabsorption (TPMA) spectra are observed and studied in various n-type samples (from $x \simeq 0.24$ to 0.30) and a p-type sample ($x \simeq 0.30$). The TPMA results provide the most accurate values of the fundamental energy gap, allowing the first observation of the "flattening" of E_g vs T at temperatures less than 20 K in $Hg_{1-x}Cd_xTe$ alloys, a phenomenon observed in most semiconductors.

The detection and identification of impurities or defects in semiconductor materials has long been a topic of technological importance. Of particular interest is their location within the forbidden energy gap region. Magneto-optical measurements have proven capable of locating both shallow[3] and deep[4-6] levels in n- or p-type InSb. We demonstrate in this paper that magneto-optical measurements can also be used to detect and locate shallow and deep levels in $Hg_{1-x}Cd_xTe$ alloys. Observation of one-photon and/or two-photon interband transitions aids in the identification of these levels.

II. EXPERIMENTAL WORK

The measurements reported here were carried out on single-crystal samples of $Hg_{1-x}Cd_xTe$ grown by solid-state recrystallization. A summary of the sample properties is given in Table I. The samples were rectangular slabs $\simeq 8 \times 1 \times 0.2$ mm, whose surfaces were lapped using alumina grit and then chem-mechanically polished using a 2% bromine–methanol solution. Electrical contacts were made to the samples using pure indium. The samples were electrically characterized prior to the magneto-optical measurements and showed the normal temperature dependence of the Hall coefficient and resistivity.

 © 1989 American Vacuum Society

TABLE I. Sample properties and magneto-optical results.

Sample No.	Manufacturer nominal properties: n(77 K) (cm^{-3})	μ(77 K) (cm^2/V s)	x	TPA data: E_g (meV) at 7 K	x	Impurity or defect levels observed
1	1.4×10^{14}	1.6×10^5	0.2406 ± 0.001	122.0 ± 0.5	0.2364 ± 0.0003	Residual acceptor 9.8 meV above valence-band edge.
2	3.3×10^{14}	8.2×10^4	0.2450 ± 0.0017	136.0 ± 0.5	0.2448 ± 0.0003	Residual acceptor 10.4 meV above valence-band edge
3	2.8×10^{14}	1.2×10^5	...	146.0 ± 0.5	0.2508 ± 0.0003	...
4	1.0×10^{14}	7.6×10^4	0.2595 ± 0.0015	156.0 ± 0.5	0.2567 ± 0.0003	...
5	1.4×10^{14}	6.6×10^4	0.277 ± 0.001	195.0 ± 0.5	0.2801 ± 0.0003	Two closely spaced midgap levels seen at 94 and 100 meV below conduction-band edge.
6	9.9×10^{13}	5.3×10^4	0.2995 ± 0.0035	225.0 ± 0.5	0.2976 ± 0.0003	...
7	*p* type 1.5×10^{15}	480	0.2945 ± 0.0035	222.0 ± 1.0	0.2964 ± 0.0006	...

Figure 1 is a schematic diagram of the experimental apparatus used for the magneto-optical studies presented here. The output of a grating tunable cw CO_2 laser was mechanically chopped into 20-μs-wide pulses with a low duty cycle to prevent lattice heating effects. A zero-order waveplate was used to produce circularly polarized light and experimentally confirm the selection rule dependence of the observed two-photon magneto-optical resonances. The laser light was focused onto a sample placed in the solenoid of a superconducting magnet capable of producing dc magnetic fields as high as 120 kG. The direction of propagation of the laser light was parallel to the magnetic field, while the samples were mounted in a transverse magnetoresistance geometry with $\mathbf{B}\parallel\langle 111\rangle$ crystal direction. The photoconductive (PC) response of the samples versus magnetic field, obtained under constant current, Ohmic conditions, was monitored using a boxcar averager. The resulting magneto-optical spectra were then recorded on an x–y recorder.

III. RESULTS AND ANALYSIS

Figure 2 shows the PC response of sample 2 for several CO_2 laser wavelengths. Several absorption resonances are

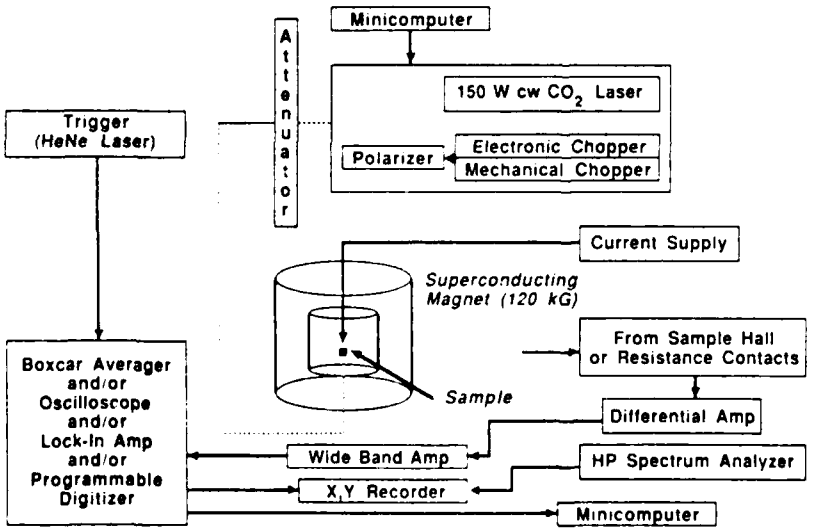

FIG. 1. Schematic diagram of magneto-optical experimental apparatus.

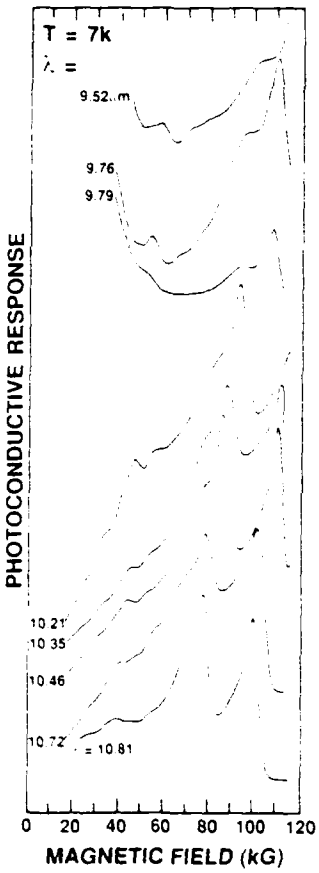

FIG. 2. Wavelength dependence of the photoconductive response for an n-type sample 2 with $x \simeq 0.245$. The two large resonances at high field arise from two-photon absorption processes. Unpolarized light was used.

clearly resolved in the spectra. We identify the structure as arising from two-photon absorption between specific valence-band Landau levels and conduction-band Landau levels. A modified Pidgeon–Brown energy-band model was used to calculate the energies for the two-photon or impurity/defect transitions observed. The transition energies for TPMA are given by

$$2\hbar\omega = E_c^{a,b}(n_c,B) - E_v^{a,b}(n_v,B),$$

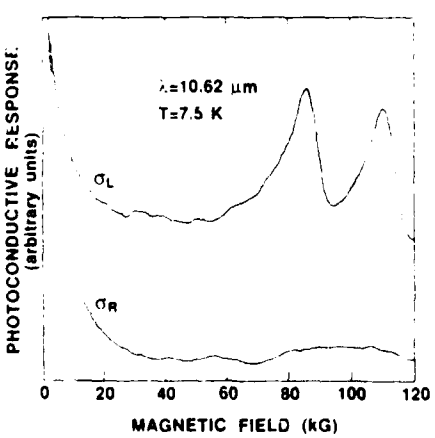

FIG. 3. Polarization dependence of the photoconductive response for sample 2.

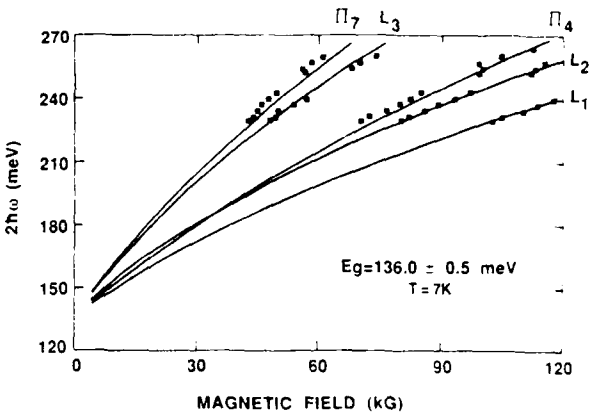

FIG. 4. Transition energy vs magnetic field for sample 2 ($x \simeq 0.245$). The energy gap is 136.0 meV.

where $\hbar\omega$ is the photon energy of the laser, $E_c^{a,b}(n_c,B)$ represents the energies of the conduction-band Landau levels in different spin states a or b, $E_v^{a,b}(n_v,B)$ represents the energies of the valence-band Landau levels, n is the Landau level number, B is the magnetic field, and the zero of energy is at the top of the valence band. The TPMA spherical selection rules are $\Delta n = 0, \pm 2$ where Δn is the change in Landau level quantum number for a given transition.

A strong selection rule dependence of the TPMA transitions was experimentally found using left circularly polarized (σ_L) and right circularly polarized (σ_R) laser light as shown in Fig. 3. Two-photon absorption is strongest for $\Delta n = +2$ using left circularly polarized light. According to second-order perturbation theory, the TPA transition probabilities are proportional to the product of two matrix elements. In the "intra–inter band" scenario, one matrix element represents an intraband transition, while the other, an interband one. Thus the strong resonances for σ_L polarization are not unexpected since the strongest intraband matrix element would be for the σ_L or cyclotron resonance active case.

TABLE II. Two-photon magnetoabsorption transition assignments.

Designation	Energy-level transition	Polarization
π_1	$a^+(0) \to a^c(0)$	σ or π
L_1	$a^+(-1) \to a^c(1)$	σ_L
π_2	$a^-(1) \to a^c(1)$	σ or π
π_3	$b^-(1) \to b^c(1)$	σ or π
L_2	$b^+(-1) \to b^c(1)$	σ_L
π_4	$b^+(0) \to b^c(0)$	σ or π
π_5	$a^-(2) \to a^c(2)$	σ or π
π_6	$b^-(2) \to b^c(2)$	σ or π
L_3	$a^+(0) \to a^c(2)$	σ_L
π_7	$a^+(1) \to a^c(1)$	σ or π
π_8	$a^-(3) \to a^c(3)$	σ or π
L_4	$b^+(0) \to b^c(2)$	σ_L
L_5	$a^-(2) \to a^c(2)$	σ_L
L_6	$b^-(2) \to b^c(2)$	σ_L

Figure 4 shows a comparison of theoretically calculated and experimentally determined two-photon transition energies versus magnetic field B. Various possible TPMA transitions are given in Table II along with the polarization needed for their observation, and symbols designating these transitions. Hereafter we shall use the designations given in Table II to describe the transitions. We obtain excellent agreement between theory and experiment using Weiler's[7] set of energy band parameters: $E_p = 19.0$ eV, $\Delta = 1.0$ eV, $\gamma_1 = 3.3$, $\gamma_2 = 0.1$, $\gamma_3 = 0.9$, $F = -0.8$, $q = 0$, $N_1 = 0$, and $\kappa = -0.8$. The energy gap extracted from Fig. 4 for this sample was $E_g = 136.0 \pm 0.5$ meV, which yields $x = 0.2448$ using the Hansen, Schmit, and Casselman[8] (HSC) relation. We see from Fig. 4 that TPMA provides a very accurate means for measuring the energy gap of $Hg_{1-x}Cd_xTe$; the two strongest transitions L_1 and L_2 are well described by the theoretical model. As a result, we have studied the temperature dependence of E_g for a variety of x-value samples. An example of the temperature dependence of the TPMA spectra for sample 1 is shown in Fig. 5. We see that the magnetic field positions of the two strong TPMA resonances are relatively independent of temperature from 2 to 15 K, and shift to lower magnetic field at higher temperatures. These data were analyzed using the Pidgeon–Brown energy-band model by adjusting only the value of E_g in order to fit the TPMA transition energy versus magnetic field positions. The TPMA results for the energy gap dependence on temperature are shown in Fig. 6, and compared to the predictions of HSC.[8] We see that the energy gap data are relatively independent of temperature between 2 and 15 K, increase more rapidly than predicted from the HSC relation between 20 to 100 K, and finally above 100 K have a slope that can be explained by the HSC relation.

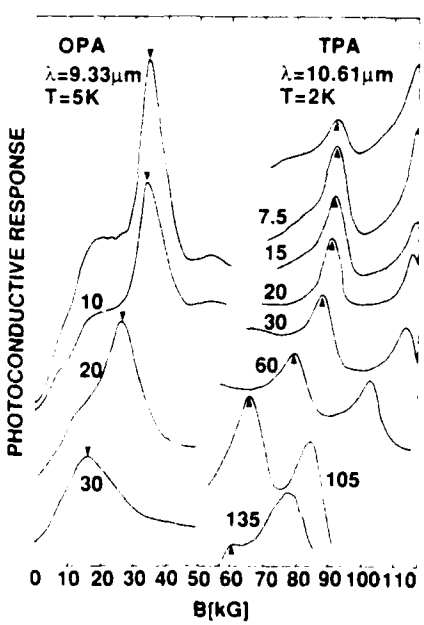

FIG. 5. Temperature dependence of the photoconductive response of sample 1 ($x \simeq 0.236$).

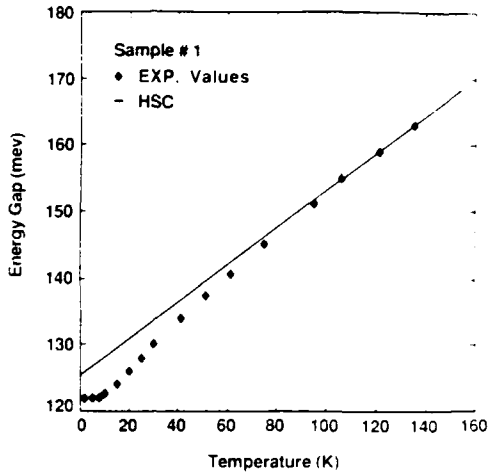

FIG. 6. Energy gap vs temperature for sample 1 ($x \simeq 0.236$). Note the flattening at low temperatures.

Figure 5 also shows one-photon magnetoabsorption (OPMA) spectra at lower magnetic fields obtained with $\lambda = 9.33\,\mu$m. These data also show directly that the OPMA resonance positions are independent of temperature below $\simeq 15$ K, indicating that the E_g vs T dependence becomes independent of temperature. A more detailed calculation and analysis of this OPMA data using a modified Pidgeon–Brown energy-band model and one-photon selection rules to calculate the one-photon transition energies gives quantitative agreement with the TPMA results presented in Fig. 6.

The wavelength dependence of the TPMA structure for sample 1 is shown in Fig. 7. As seen for sample 2 (Fig. 2), two strong resonances at high fields are clearly observed and are related to σ_L transitions L_1 and L_2. The wavelength independent structure is ascribed to magnetoimpurity resonances resulting from inelastic scattering processes involving the TPA produced carriers. A similar sort of wavelength independent structure can also be seen for one-photon excitation conditions as shown in Fig. 8 for shorter wavelengths and lower magnetic fields. In both cases these magnetoimpurity resonances arise from inelastic scattering processes whereby free carriers resonantly exchange energy with a second carrier bound to a donor or acceptor impurity in the presence of a magnetic field. Hot-electron conditions are necessary for the observation of these resonances, which are obtained here by photoexcitation of carriers into the conduction band by optical excitation (either one or two photon) across the band gap. Two other resonances are also seen in Fig. 8: one-photon magnetoabsorption resonances are indicated by the short arrows and a broad absorption peak by the long arrow. In the case of the broad peak, the temperature dependence and time-resolved behavior of the PC response indicate that this absorption peak results from electron transitions from a shallow acceptor or Hg vacancy level to the lowest conduction-band Landau level, as does the activation energy of 9.8[9-12] meV extracted from the calculations presented in Fig. 9. This activation energy is consistent with both shallow acceptor impurities and the lowest Hg vacancy level[10] in $Hg_{1-x}Cd_xTe$. Figure 9 also shows a comparison of

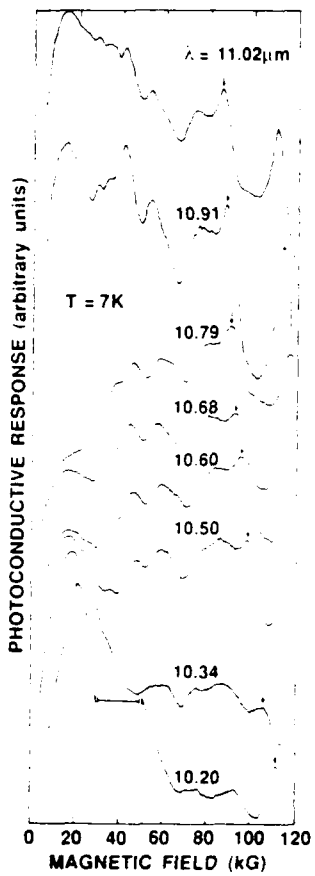

FIG. 7. Photoconductive response at high laser intensities for sample 1 ($x \simeq 0.236$). The arrow shows how a TPMA resonance shifts with photon energy. Note unusual, wavelength independent structure observed for $\lambda = 10.34$–10.79 μm.

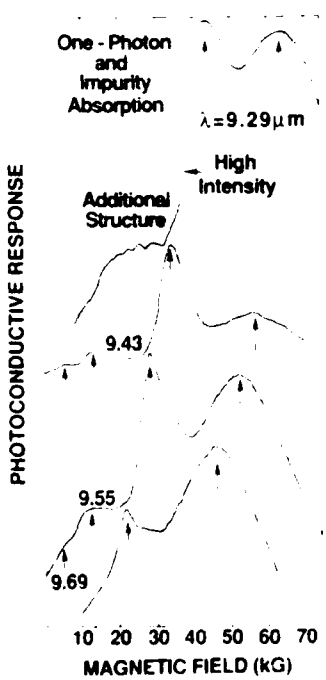

FIG. 8. Intensity dependence of the photoconductive response for sample 1 showing three types of structure: (i) short arrows denote one-photon magnetoabsorption resonances, (ii) long arrows, acceptor level to lowest conduction-band Landau level, and (iii) the additional, high-intensity structure attributed to magnetoimpurity resonances.

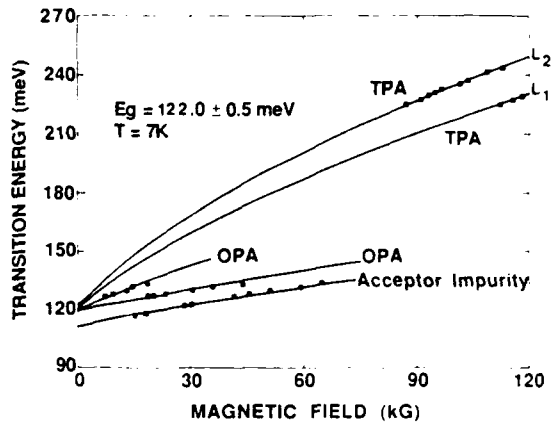

FIG. 9. Transition energy vs magnetic field showing one-photon (OPA), two-photon (TPA), and acceptor impurity behavior for sample 1. The x value is obtained from the Hansen, Schmit, Casselman relation (Ref. 8) at 7 K using the TPMA determined gap.

theoretical calculations for the TPMA (L_1 and L_2 structure) and OPMA transitions versus magnetic field with the data all obtained on sample 1. Excellent agreement between theory and data is clearly seen for both the TPMA and OPMA results. Since exciton corrections have been shown previously[7] to be necessary to describe OPMA data in HgCdTe and are not significant for TPMA, we obtained a consistent description of both sets of data by using a free exciton binding energy of 2 meV to describe the OPMA data.

Figure 10 shows the wavelength dependence of the PC response for sample 5. Again, the two strong σ_L resonances shown earlier for samples 1 and 2 are seen. In addition, at higher fields, weaker and broader resonances are seen which cannot theoretically be described by TPMA processes. Instead, we interpret these resonances as resulting from electron transitions from near-mid-gap levels to the lowest con-

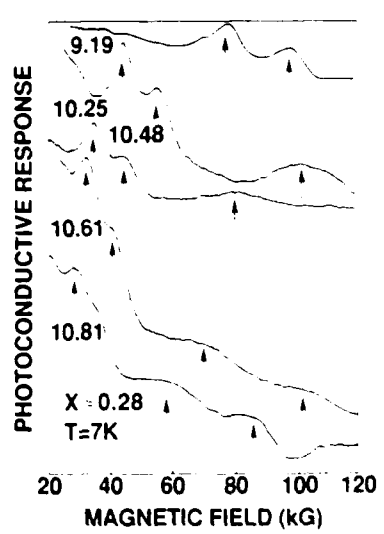

FIG. 10. Wavelength dependence of the photoconductive response for sample 5 ($x \simeq 0.280$).

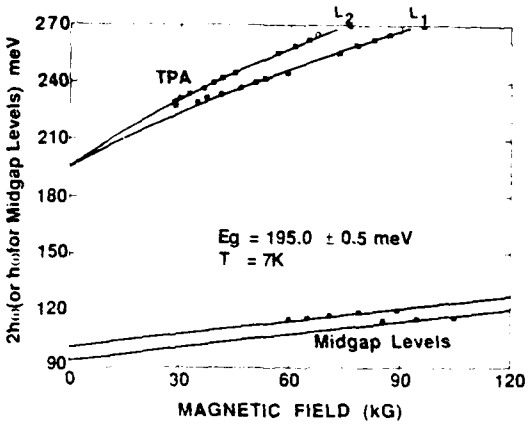

FIG. 11. Transition energy vs magnetic field showing two-photon (TPA) and midgap level transitions for sample 5 ($x \simeq 0.280$).

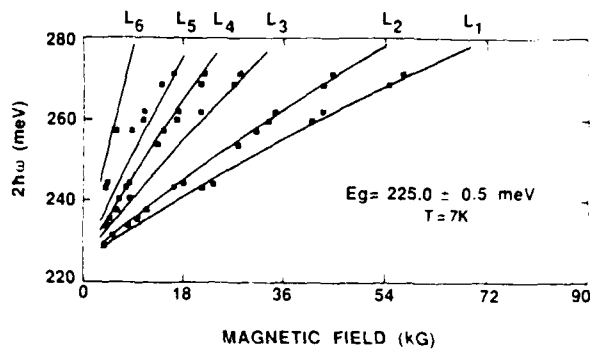

FIG. 13. Transition energy vs magnetic field for sample 6 ($x \simeq 0.300$). The band gap is determined to be 225.0 meV

duction-band Landau level. The transition energy versus magnetic field plots shown in Fig. 11 show excellent agreement between the experimental data and the calculated transition energies, confirming the TPMA and midgap level interpretation of the data. An energy gap of 195.0 ± 0.5 meV is found, along with activation energies of 94 and 100 meV below the conduction-band edge for the two midgap levels. For the activation energy calculations, the transition energies for the one-photon midgap case are described by $\hbar\omega = E_c(0,B) - E_t$, where E_t is the energy of a midgap level above the valence band. As $B \to 0$, $E_c(0,B) \to E_g$ and hence $\hbar\omega \to E_g - E_t$, the $B = 0$ intercept.

Finally, in Fig. 12, we show the photoconductive response of sample 6 for various CO_2 laser wavelengths using left circular polarized light σ_L. Once again, two strong σ_L TPMA transitions are observed as in the other samples. Other TPMA resonances are also seen at lower fields and are also attributed to transitions with selection rules associated with the σ_L polarization. Figure 13 shows the transition energy data and theoretical calculations giving good agreement with $E_g = 225.0 \pm 0.5$ meV. TPMA spectra have also been seen in a p-type sample with $x \simeq 0.30$ that look quantitatively the same as the data shown in Fig. 12 for n-type samples.

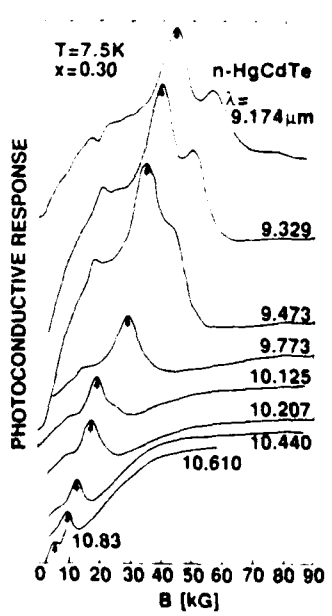

FIG. 12. Wavelength dependence of the photoconductive response for sample 6 ($x \simeq 0.300$) using σ_L (left circular polarized) laser light.

IV. SUMMARY

Two-photon magnetoabsorption structure has been observed and studied in a wide variety of samples of both n- and p-type HgCdTe. Our studies demonstrate the uniqueness and importance of TPMA methods as tools to characterize HgCdTe. For example, we have accurately determined the temperature dependence of the band gap and found distinct deviations from the Hansen, Schmit, Casselman relation with $dE_g/dT \to 0$ below 20 K.

Finally, these laser-based studies have allowed the observation of impurity(or defect)-to-conduction-band transitions from midgap levels and transitions from shallow acceptors to the conduction band.

ACKNOWLEDGMENTS

We acknowledge the support of this work by the U.S. Army Center for Night Vision and Electro-Optics, Contract No. DAAB07-87-C-FO94.

[a] Current address: National Institute of Standards and Technology, Materials Technology Group, Semiconductor Electronics Division, Center for Electronics and Electrical Engineering, Gaithersburg, MD 20899.

[1] D. G. Seiler, S. W. McClure, R. J. Justice, M. R. Loloee, and D. A. Nelson, Appl. Phys. Lett. 48, 1159 (1986).
[2] D. G. Seiler, S. W. McClure, R. J. Justice, M. R. Loloee, and D. A. Nelson, J. Vac. Sci. Technol. A 4, 2034 (1986).
[3] C. L. Littler, D. G. Seiler, R. Kaplan, and R. J. Wagner, Phys. Rev. B 27, 7473 (1983).

[4]D. G. Seiler and M. W. Goodwin, J. Appl. Phys. **53**, 7505 (1982).
[5]C. L. Littler, D. G. Seiler, R. Kaplan, and R. J. Wagner, Appl. Phys. Lett. **41**, 880 (1982).
[6]D. G. Seiler, K. H. Littler, and C. L. Littler, Semicond. Sci. Technol. **1**, 383 (1986).
[7]M. H. Weiler, in *Semiconductors and Semimetals*, edited by R. K. Willardson and A. C. Beer (Academic, New York, 1981), Vol. 16, p. 119.
[8]G. L. Hansen, J. L. Schmit, and T. N. Casselman, J. Appl. Phys. **53**, 7099 (1982).
[9]M. H. Kalisher, J. Cryst. Growth **70**, 369 (1984).
[10]F. J. Bartoli, C. A. Hoffman, and J. R. Meyer, J. Vac. Sci. Technol. A **4**, 2047 (1986).
[11]M. C. Chen and J. H. Tregilgas, J. Appl. Phys. **61**, 787 (1987).
[12]M. C. Chen and J. A. Dodge, Solid State Commun. **53**, 449 (1986).

Magneto-optical investigation of impurity and defect levels in HgCdTe alloys

C. L. Littler
Department of Physics, University of North Texas, Denton, Texas 76203

D. G. Seiler
Semiconductor Electronics Division, National Institute of Standards and Technology, Gaithersburg, Maryland 20899

M. R. Loloee
Department of Physics and Astronomy, Center for Fundamental Material Research, Michigan State University, East Lansing, Michigan 48824

(Received 4 October 1989; accepted 29 October 1989)

We have observed and described magneto-optical transitions between impurity/defect levels and conduction band Landau levels for a variety of n-type HgCdTe samples with $0.2 < x < 0.3$. The activation energies of these levels fall into two categories: (1) 10–12 meV above the valence band edge, independent of E_g and (2) two close spaced levels at $\simeq 0.5\ E_g$. In addition, the spectra of several narrow gap ($E_g < 100$ meV) samples exhibit shallower and deeper acceptor-like levels.

I. INTRODUCTION

The ternary compound semiconductor mercury cadmium telluride (MCT) has been, for the last two decades, the material of choice for use in infrared detection systems. Since impurities and defects, even in low concentrations, are usually responsible for limiting detector performance, it is desirable to develop and use sensitive techniques for the detection of these "flaws" or imperfections. Specifically, detailed information about the energy band structure and the levels created by the presence of impurities and defects is crucial to understanding and improving the performance of current infrared detectors. In order to characterize impurities and defects present in a semiconductor, one prefers a technique that is sensitive, rapid, and straightforward to analyze. In the past, a variety of techniques—deep level transient spectroscopy (DLTS), thermally stimulated current (TSC), diode pulse recovery, etc.—have been used to study impurities and defects in MCT.[1–26] In addition, a need has been expressed[11] for characterization techniques that can identify different electrically active shallow-level impurities and optical techniques that can be used to identify these centers. These techniques would then provide a means to guide future development of MCT growth.

In this paper we employ magneto-optics to detect the presence of impurities and defects in samples of MCT with $0.215 < x < 0.300$. These techniques have already been used with considerable success to detect and study both shallow[27] and deep[28–30] levels in n- and p-type InSb. We show that these magneto-optical methods can be used to detect the presence of shallow compensating acceptors in alloys of MCT as well as near midgap impurity/defect levels in the same material. Thus, magneto-optical methods provide a powerful tool for the study of impurity and defect levels in MCT.

II. EXPERIMENTAL WORK

The samples used in this study were grown by solid-state recrystallization and the traveling heater method. The samples, cut into rectangular slabs $\simeq 8 \times 1 \times 0.2$ mm,[3] were lapped using alumina grit and chem-mechanically polished using a 2% bromine-methanol solution. Contacts were made to the sample using pure indium. A schematic diagram of the experimental apparatus has been presented in a previous paper.[25] The output of a grating tunable cw CO_2 laser was focused onto samples placed in a 12 T superconducting magnet/variable temperature dewar system. The magneto-optical spectra were obtained by monitoring the photoconductive response of each sample using boxcar averaging techniques and recording the results on an x–y recorder. In order to verify the origin of all observed magneto-optical resonances, a zero-order waveplate and a zero phase-shift mirror were used as the final two optical elements outside the dewar. These items provided the left- and right-circular light polarization used in our experiments. Unless otherwise indicated, circularly polarized light was used to study the impurity/defect magneto-optical transitions.

III. RESULTS AND DISCUSSION

The origin of both the two-photon and impurity/defect level magneto-optical transitions can be understood qualitatively by the simplified Landau-level model schematically presented in Fig. 1. The two-photon magnetoabsorption (TPMA) transitions are indicated by the solid arrows and the impurity/defect-to-conduction band transitions are indicated by the dashed arrows. Resonant absorption occurs whenever the energy separation between these Landau levels equals the energy prescribed by the particular absorption phenomena. For the two-photon interband transitions, magneto-optical resonances will occur whenever $2\hbar\omega$ is equal to the energy difference between particular valence and conduction band Landau levels, in accordance with appropriate selection rules. A sketch of the resulting magneto-optical spectra is shown in the middle of Fig. 1. If, however, the initial state of the magneto-optical transition is a level or state within the forbidden energy gap, then a different magneto-optical spectra will be seen. These resonances will oc-

 © 1990 American Vacuum Society

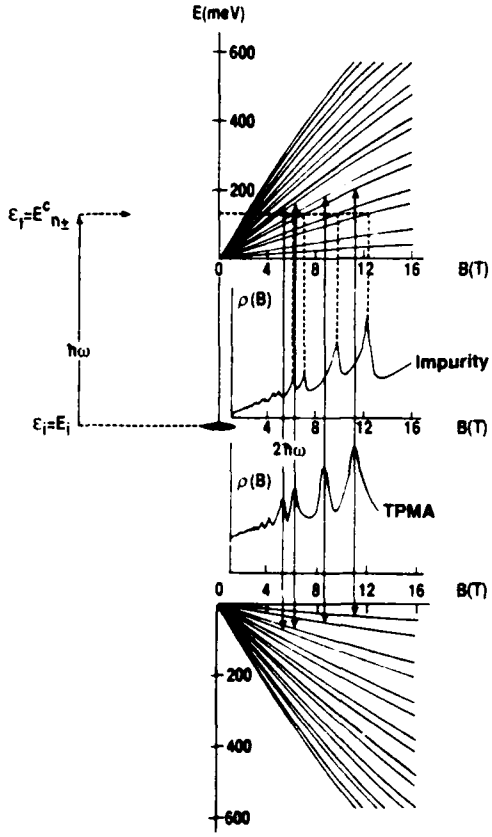

FIG. 1. Schematic representation of the origin of TPMA and impurity/defect-to-band resonant magneto-optical spectra. The two-photon transitions are represented by the solid arrows and the impurity transitions by the dashed lines. It is shown that each absorption process has its own associated spectra and can thus be so identified.

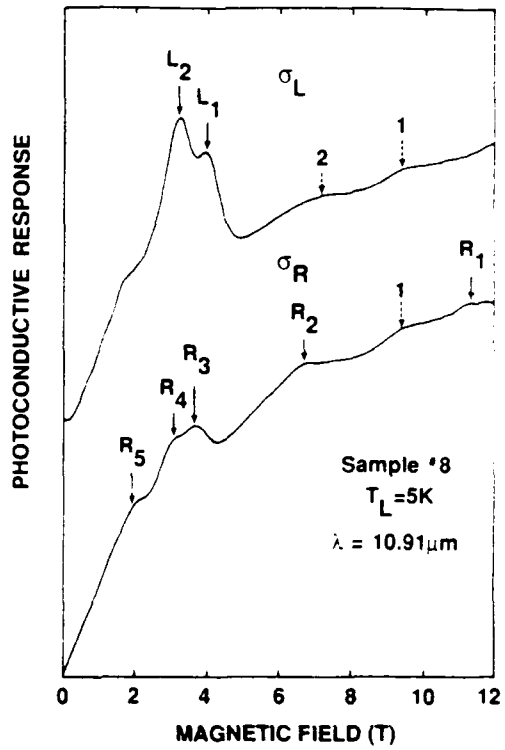

FIG. 2. Polarization dependence of the TPMA and impurity/defect transitions. The impurity resonances can be seen for both polarizations, while the TPMA structure obeys two-photon selection rules.

cur only when $\hbar\omega$ is equal to the energy separation between the impurity/defect level and the conduction band Landau levels, following no particular selection rule. Thus, each absorption process possesses its own characteristic spectra and thus can be so identified.

An example of the TPMA and impurity/defect magneto-optical spectra obtained for left-circularly polarized (σ_L) and right-circularly polarized light (σ_R) is shown in Fig. 2 for sample No. 8. For σ_L we see two strong TPMA resonances labeled by the solid arrows L_1 and L_2. The two broader absorption peaks, labeled 1 and 2, are ascribed to electron transitions from two closely spaced impurity/defect levels located at approximately midgap to the lowest-lying conduction band Landau level. Preliminary results on both of these effects have been reported earlier.[25,26] The magnetic field positions of all arrows indicate the theoretically expected positions of both the TPMA and the impurity/defect resonances. How these positions are calculated will be discussed later. Upon changing the polarization to σ_R, we see that the strong σ_L transitions disappear, being replaced with weaker TPMA resonances labeled by R_1–R_5. It should be noted that R_1 and R_2 are more widely spaced in magnetic field than the impurity/defect transitions 1 and 2, and some features of 1 and 2 appear for both polarizations. Since impurity/defect levels are of mixed s and p character, they should show no dependence on selection rules. Thus, by the use of circular polarization, we are able to separate out the contributions to the magneto-optical spectra from each absorption process mentioned above.

Two-photon interband and impurity-to-band magneto-optical spectra for an n-type sample with $x = 0.296$ (Sample No. 9) is shown in Fig. 3. The wavelength dependence of the photoconductive response, obtained at 5 K, is shown in order of decreasing wavelength or increasing photon energy. The downward-pointing arrows, labeled by the transition assignments L_1, L_2, etc., indicate magneto-optical resonances arising from two-photon magneto-absorption (TPMA), reported earlier.[25,26] A legend for the TPMA transitions is given in Table I. At higher magnetic fields, beyond the last σ_L TPMA resonance, we see two broader absorption peaks, indicated by the upward-pointing arrows. We ascribe these magneto-optical resonances to electron transitions from two closely spaced impurity/defect levels located at approximately midgap to the lowest-lying conduction band Landau level.

Figure 4 shows a comparison of theoretically calculated and experimentally determined transition energies for both the two-photon and midgap level transitions. A modified Pidgeon–Brown energy band model[31] was used to calculate the energies of both the two-photon and impurity/defect

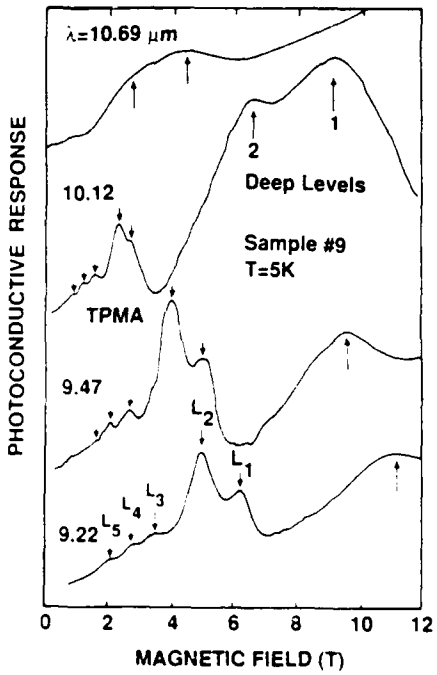

FIG. 5. Wavelength dependence for the photoconductive response for sample No. 9 ($x = 0.296$), showing both TPMA resonant structure and that arising from impurity/defect-to-band transitions. The transition assignments for the resonances labeled L_1–L_5 are given in Table I.

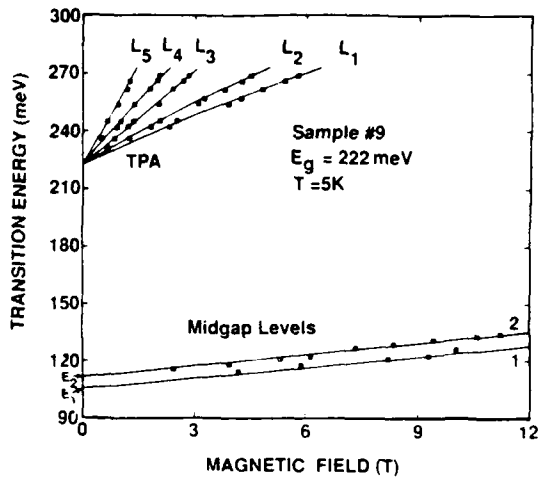

FIG. 4. Transition energy vs magnetic field for sample No. 9. The labels 1 and 2 refer to the near midgap level-to-band transitions $E_1 \rightarrow a^c(0)$ and $E_2 \rightarrow a^c(0)$, where E_1 and E_2 are 111.5 and 116 meV above the valence band edge, respectively.

magneto-optical transitions observed. The transition energies for TPMA are given by

$$2\hbar\omega = E_c^{a,b}(n_c,B) - E_v^{a,b}(n_v,B), \quad (1)$$

where $\hbar\omega$ is the laser photon energy, $E_c^{a,b}(n_c,B)$ represents the energies of the conduction band Landau levels of spin a or b, $E_v^{a,b}(n_v,B)$ represents the energies of the valence band Landau levels, n is the Landau level quantum number, B is the magnetic field strength, and the zero of energy is defined at the zero-field valence band edge. Note that as $B \rightarrow 0$, $2\hbar\omega \rightarrow E_g$. Thus, the value of energy gap can be obtained by fitting the two-photon data using E_g as an adjustable parameter. The same method of analysis can be used for one-photon magneto-absorption (OPMA) data, by substituting $\hbar\omega$ for $2\hbar\omega$ and adding the appropriate exciton correction. In a previous study[25] which compared OPMA and TPMA data obtained on the same sample, we found that it is sufficient to add an exciton correction of 2 meV for samples with $E_g \simeq 100$ meV.

TABLE I. One- and two-photon magnetoabsorption transition assignments.

Designation	Energy-level transition	Polarization
K_1	$a^+(-1) \rightarrow a^c(0)$	σ_L
K_2	$b^+(-1) \rightarrow b^c(0)$	σ_L
K_3	$a^+(0) \rightarrow a^c(1)$	σ_L
K_4	$b^+(0) \rightarrow b^c(1)$	σ_L
K_5	$a^+(1) \rightarrow a^c(2)$	σ_L
L_1	$a^+(-1) \rightarrow a^c(1)$	σ_L
L_2	$b^+(-1) \rightarrow b^c(1)$	σ_L
L_3	$a^+(0) \rightarrow a^c(2)$	σ_L
L_4	$b^+(0) \rightarrow b^c(2)$	σ_L
L_5	$a^+(1) \rightarrow a^c(3)$	σ_L
L_6	$b^+(1) \rightarrow b^c(3)$	σ_L
R_1	$a^-(2) \rightarrow a^c(0)$	σ_R
R_2	$b^-(2) \rightarrow b^c(0)$	σ_R
R_3	$a^-(3) \rightarrow a^c(1)$	σ_R
R_4	$b^-(3) \rightarrow b^c(1)$	σ_R
R_5	$a^-(4) \rightarrow a^c(2)$	σ_R

For each sample discussed in this paper, either TPMA or OPMA was measured and the energy gap extracted. The energy gaps were then used to reference the activation energies of the impurity and defect levels. The transition energies of the midgap level transitions are

$$\hbar\omega = E_c^{a,b}(n_c,B) - E_i, \quad (2)$$

where E_i is the activation energy of the midgap level, as referenced to the valence band edge. Note that as $B \rightarrow 0$, $\hbar\omega \rightarrow E_g - E_i$. The theoretical transition energies shown in Fig. 4 were calculated using Weiler's[32] set of energy band parameters in the modified Pigeon–Brown scheme: $E_p = 19.0$ eV, $\Delta = 1.0$ eV, $\gamma_1 = 3.3$, $\gamma_2 = 0.1$, $\gamma_3 = 0.9$, $\kappa = -0.8$, $F = -0.8$, $q = 0.0$, and $N_1 = 0.0$. From the TPMA data for sample No. 9, we obtain a value of 222.0 ± 0.5 meV for the energy gap of this sample. The analysis of the impurity/defect level data yields activation energies of 111.5 meV and 116.0 meV for the two closely spaced midgap levels. It is currently believed that these midgap states result from the formation of cation vacancy, anion impurity complex.[33]

These near-midgap levels are also seen to be present in the lower x-value samples of MCT. However, for the magnetic fields and photon energies used, these midgap transitions are superimposed on the TPMA background, as shown in Fig. 5 for sample No. 6 ($x = 0.246$). At the highest fields we see

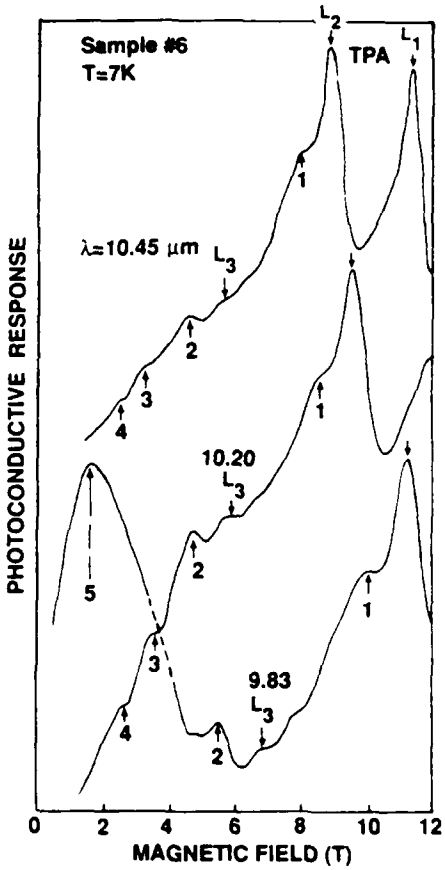

FIG. 5. Wavelength dependence for the photoconductive response for sample No. 6 ($x = 0.246$), showing both TPMA resonant structure and that arising from impurity/defect-to-band transitions. The labels 1–5 refer to the transitions 1: $E_2 \rightarrow a^c(0)$, 2: $E_1 \rightarrow a^c(0)$ 3: $E_2 \rightarrow b^c(0)$, 4: $E_1 \rightarrow b^c(0)$, and 5: $E_3 \rightarrow b^c(0)$, where E_1, E_2 and E_3 are 63, 68, and 20 meV above the valence band edge, respectively.

the strong TPMA resonances labeled by L_1, L_2, and L_3. At th lower magnetic fields weak resonances are seen which do not correspond to the expected values for the TPMA transitions

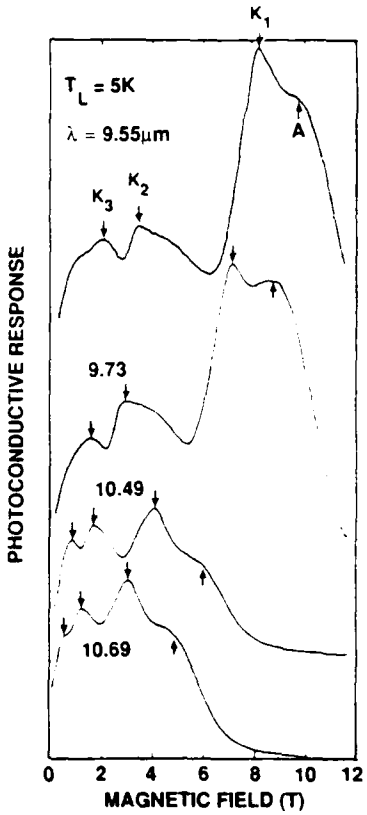

FIG. 7. Wavelength dependence for the photoconductive response for sample No. 3 ($x = 0.225$), showing both OPMA resonant structure labeled K_1–K_5, and that arising from shallow acceptor impurity-to-conduction band transitions labeled 1.

L_4, L_5, and L_6. These resonances are indicated by the upward-pointing arrows labeled 1–5. In addition, these weak resonances appear for both σ_L and σ_R light polarizations, whereas the two-photon resonances show a strong polarization dependence due to TPMA selection rules (see Fig. 3 of Ref. 25). The analysis of the magneto-optical data shown in Fig. 5 is given in Fig. 6. From the TPMA results, an energy

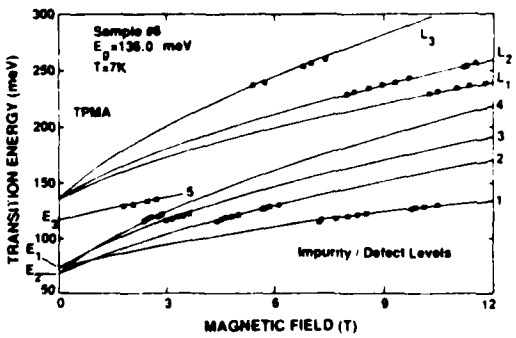

FIG. 6. Transition energy versus magnetic field for sample No. 6. An energy gap of 136.0 meV is obtained from the analysis of the TPMA data, shown by the theoretical lines labeled L_1, L_2 and L_3. The activation energies for the shallow and deep levels E_1, E_2, and E_3 are 63, 68, and 20 meV above the valence band edge, respectively.

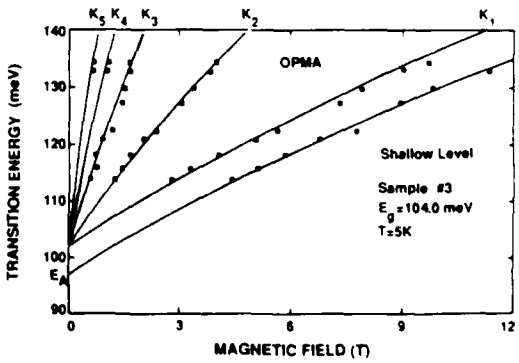

FIG. 8. Transition energy vs magnetic field for sample No. 3. From the fit, a value of 7.0 meV is obtained for the acceptor binding energy E_A.

gap of 136.0 meV is determined. From the remaining resonances, we extract activation energies of 63 meV and 68 meV above the VBE for E_1 and E_2. In addition, analysis of a resonance observed at lower fields (indicated in Fig. 6 by transition assignment No. 5) yield an activation energy of 20.0 meV for E_3.

The results for a very narrow gap sample are shown in Fig. 7. At low magnetic fields, resonant structure (labeled K_1, K_2,

TABLE II. Summary of impurity/defect levels for HgCdTe. PL = photoluminescence, DLTS = deep level transient spectroscopy, AS = admittance spectroscopy, TSC = thermally stimulated current, MOS = magneto optical spectroscopy, EPR = electron paramagnetic resonance.

Year	Technique	Type (dopant)	x-value	E (meV) (shallow)	E (meV) (E_g/4)	E (meV) (E_g 1/2)	E (meV) ($3E_g$/4)	
1972	Hall, PL	p	0.26	15,16	···	···	···	1
			0.33	18,13	···	···	···	
			0.34	19,10	···	···	···	
1979	lifetime, PL	n	0.3	18	70	···	···	2
1980	DLTS	p	0.21	···	···	35,43	···	3
1980	AS	diode	0.22	···	···	46	···	4
			0.31	···	···	160	···	
1980	PL	n	0.32	14 ± 1.5	···	···	···	5
		p (Au)	0.48	4.5 ± 2,				
				15.5 ± 2	···	···	···	
1981	DLTS	p (Hg vac)	0.21	···	43	···	···	6
			0.39	···	118	283	···	
1981	DLTS,	p (Hg vac)	0.207	···	···	37,44	···	7
	AS		0.215	···	···	35,46	···	
			0.271	···	···	70,81	···	
			0.285	···	···	81,92	···	
			0.305	···	···	161	208	
			0.320	···	···	···	206,218	
1981	DLTS	p (Hg vac)	0.215	···	···	35,43	···	8
			0.305	···	···	···	181,208	
			0.320	···	···	···	206,218	
1981	lifetime	p (Hg vac)	0.215	···	···	56	···	9
			0.220	···	37	···	···	
			0.326	···	···	150	···	
			0.386	···	···	230	···	
1981	PL	n	0.3	10	···	···	···	10
1982	DLTS	n	0.27	···	···	136	···	11
		p (Cu)	0.39	···	70	150	···	
1982	PL	n	0.32	14 ± 1	···	···	···	12
			0.48	15.5 ± 2	···	···	···	
1983	lifetime	n	0.307	···	···	···	223	13
			0.332	···	···	···	271	
			0.344	···	···	···	284	
			0.352	12	···	···	···	
			0.335	30	···	···	···	
1983	DLTS	p (Au)	0.48	···	140	200	230	14
1984	PL	n	0.320	···	···	0.4E_g	···	15
			0.340	···	···	0.4E_g	···	
1985	EPR	p (As)	0.3	10	50	···	···	16
1985	lifetime	p (Au)	0.215	15	···	···	···	17
			0.225	15	···	···	···	
			0.29	20	···	···	···	
1985	DLTS	n	0.3	···	79	120	172	18
1986	Hall data	p (Au)	0.22	5,12.5	···	···	···	19
1986	photoHall	p (Cu,Hg V)	0.224	7	···	E_g/2	···	20
1986	lifetime	n (Au,Si,	0.230	10 ± 2	···	···	···	21
		Cl,Fe,In)	0.245	···	···	···	124	
			0.31	···	···	···	200,232	
			0.32	···	···	···	233,253	
			0.33	15 ± 5	70 ± 7	···	···	
1986	Hall data	p (Cu)	0.22	11	···	···	···	22
1987	lifetime	p	0.24	···	···	···	92	23
1987	Hall data	p (Cu)	0.2	11.5	···	···	···	24
1988	MOS	n	0.23	10	···	···	···	25,26
			0.25	9.8	···	···	···	
			0.28	···	···	94,100	···	

TABLE III. Sample properties and magneto-optical results

Sample	n (77 K) (cm^{-3})	μ (77 K) (cm^2/V s)	E_g (7 K) (meV)	X value	E (meV) (shallow)	E (meV) ($E_g/4$)	E (meV) ($E_g/2$)
1	$\simeq 5\times10^{14}$	$\simeq 1\times10^5$	80.0	0.217	7.0	...	...
2	$\simeq 5\times10^{14}$	$\simeq 1\times10^5$	99.0	0.225	...	18.0, 26.0	...
3	3×10^{14}	1.5×10^5	102.0	0.225	7.0	...	...
4	1.4×10^{14}	1.6×10^5	122.0	0.239	9.8	...	...
5	2.8×10^{14}	1.2×10^5	125.0	0.241	10.0	...	60.0
6	$\simeq 5\times10^{14}$	$\simeq 1\times10^5$	136.0	0.246	...	...	63.0, 68.0
7	$\simeq 5\times10^{14}$	$\simeq 1\times10^5$	136.0	0.246	10.2	...	...
8	1.4×10^{14}	6.5×10^4	188.0	0.278	...	...	90.0, 94.0
9	3.5×10^{14}	4.3×10^5	222.0	0.296	...	...	111.5, 116.0
10	9.9×10^{13}	5.3×10^4	224.0	0.300	...	...	...

K_3 etc.) due to OPMA are observed. The transition assignments are given in Table I. At magnetic fields beyond which OPMA can be observed we see a weak magneto-optical resonance originating from a very shallow level. The analysis of the OPMA and shallow level are shown in Fig. 8. From the OPMA data we extract an energy gap of 104.0 meV at 5 K and the analysis of the shallow level data yields an activation or binding energy of 7 meV. This level is somewhat more shallow than the $\simeq 10$ meV level observed in our wider gap samples (see Table III), although levels this shallow have been seen in p-type samples with similar x values (see also Table II, Bartoli, 1986).

A survey of past work on impurities and defects in HgCdTe is given in Table II. This table is not meant to be exhaustive, only representative of past work. From this table, several trends emerge: (1) shallow acceptor-like levels with activation energies between $\simeq 2$ and 20 meV are seen in most samples, (2) near midgap levels are also detected in most samples, and (3) there is evidence for a third level at $\simeq 3/4\ E_g$ above the valence band edge. The results of our magneto-optical studies, given in Table III, are in agreement with these conclusions. Thus, magneto-optical methods provides a direct, sensitive means of detecting the presence of impurities and defects in HgCdTe alloys.

IV. SUMMARY

Magneto-optical methods have been used to detect and study impuriy and defect levels in HgCdTe. We have observed and described magneto-optical transitions for a variety of HgCdTe samples with $0.2 < x < 0.3$. The measurements provide accurate values for the activation energies of the levels observed. These appear to fall into two categories: (1) 10–12 meV above the valence band edge, independent of E_g, and (2) two closely spaced levels at $\simeq 0.5\ E_g$. In addition, the spectra of several narrow gap ($E_g \simeq 100$ meV) samples exhibit shallower and deeper acceptor-like levels. The results of these measurements show that magneto-optics is a useful tool for the investigation of impurity and defect levels in HgCdTe.

ACKNOWLEDGMENTS

This work was supported by the Center for Night Vision and Electro-Optics, Contract DAAB07-87-C-F094, and a grant from Texas Instruments, Inc.

[1]C. T. Elliot, I. Melngailis, T. C. Harman, and A. G. Foyt, J. Phys. Chem. Solids **33**, 1527 (1972).
[2]M. G. Andrukhiv, V. A. Maltseva, V. I. Ivanov-Omskii, V. K. Ogoroanikov, and T. S. Totieva, Sov. Phys. Semicond. **13**, 210 (1979).
[3]D. L. Polla and C. E. Jones, Solid State Commun. **36**, 809 (1980).
[4]D. L. Polla and C. E. Jones, J. Appl. Phys. **51**, 6233 (1980).
[5]A. T. Hunter, D. L. Smith, and T. C. McGill, Appl. Phys. Lett. **37**, 200 (1980).
[6]C. E. Jones, V. Nair, and D. L. Polla, Appl. Phys. Lett. **39**, 248 (1981).
[7]D. L. Polla and C. E. Jones, J. Appl. Phys. **52**, 5118 (1981).
[8]D. L. Polla, M. B. Reine, and C. E. Jones, J. Appl. Phys. **52**, 5132 (1981).
[9]D. L. Polla, S. P. Tobin, M. B. Reine, and A. K. Sood, J. Appl. Phys. **52**, 5182 (1981).
[10]B. L. Gelmont, V. I. Ivanov-Omskii, V. A. Maltseva, and V. A. Smirnov, Sov. Phys. Semicond. **15**, 638 (1981).
[11]C. E. Jones, V. Nair, J. Lindquist, and D. L. Polla, J. Vac. Sci. Technol. **21**, 187 (1982).
[12]A. T. Hunter and T. C. McGill, J. Vac. Sci. Technol. **21**, 205 (1982).
[13]R. G. Pratt, J. Hewett, P. Capper, C. L. Jones, and M. J. Quelch, J. Appl. Phys. **54**, 5152 (1983).
[14]C. A. Merilainen and C. E. Jones, J. Vac. Sci. Technol. A **1**, 1637 (1983).
[15]D. L. Polla and R. J. Aggarwal, Appl. Phys. Lett. **44**, 775 (1984).
[16]C. E. Jones, K. James, J. Merz, R. Braunstein, M. Burd, M. Eetemadi, S. Hutton, and J. Drumheller, J. Vac. Sci. Technol. A **3**, 131 (1985).
[17]S. E. Schacham and E. Finkman, J. Appl. Phys. **57**, 2001 (1985).
[18]V. A. Cotton, J. A. Wilson, and C. E. Jones, J. Appl. Phys. **58**, 2208 (1985).
[19]E. Finkman and Y. Nemirovsky, J. Appl. Phys. **59**, 1205 (1986).
[20]F. J. Bartoli, C. A. Hoffman, and J. R. Meyer, J. Vac. Sci. Technol. A **4**, 2047 (1986).
[21]R. G. Pratt, J. Hewett, P. Capper, C. L. Jones, and N. Judd, J. Appl. Phys. **60**, 2377 (1986).
[22]M. C. Chen and J. A. Dodge, Solid-State Commun. **53**, 449 (1986).
[23]D. E. Lacklison and P. Capper, Semiconductor Sci. Technol. **2**, 33 (1987).
[24]M. C. Chen and J. H. Tregilgas, J. Appl. Phys. **61**, 787 (1987).
[25]D. G. Seiler, C. L. Littler, M. R. Loloee, and S. A. Milazzo, J. Vac. Technol. A **7**, 370 (1989).
[26]D. G. Seiler, M. R. Loloee, S. A. Milazzo, A. J. Durkin, and C. L. Littler, Solid-State Commun. **69**, 757 (1989).
[27]C. L. Littler, D. G. Seiler, R. Kaplan, and R. J. Wagner, Phys. Rev. B **27**, 7473 (1983).
[28]D. G. Seiler and M. W. Goodwin, J. Appl. Phys. **53**, 7505 (1982).
[29]C. L. Littler, D. G. Seiler, R. Kaplan, and R. J. Wagner, Appl. Phys. Lett. **41**, 880 (1982).
[30]D. G. Seiler, K. H. Littler, and C. L. Littler, Semicond. Sci. Technol. **1**, 383 (1986).
[31]M. H. Weiler, R. L. Aggarwal, and B. Lax, Phys. Rev. B **17**, 3269 (1978).
[32]M. H. Weiler, in *Semiconductors and Semimetals*, edited by R. K. Willardson and A. C. Beer (Academic, New York, 1981), Vol. 16, p. 119.
[33]C. W. Myles, P. F. Williams, R. A. Chapman, and E. G. Bylander, J. Appl. Phys. **57**, 5279 (1985).

Temperature and composition dependence of the energy gap of $Hg_{1-x}Cd_xTe$ by two-photon magnetoabsorption techniques

D. G. Seiler and J. R. Lowney
Semiconductor Electronics Division, National Institute of Standards & Technology, Gaithersburg, Maryland 20899

C. L. Littler
Department of Physics, University of North Texas, Denton, Texas 76203

M. R. Loloee
Department of Physics and Astronomy, Center for Fundamental Materials Research, Michigan State University, East Lansing, Michigan 48824

(Received 4 October 1989; accepted 29 October 1989)

Accurate determinations of the energy gap E_g at liquid helium temperatures in alloys of $0.24 \leq x \leq 0.30$ have been made by two-photon magnetoabsorption techniques. They are shown to help verify the use of the Hansen–Schmit–Casselman (HSC) relation over the range $0 < x < 0.30$ at these temperatures. In contrast, the observed temperature dependence of E_g below 77 K is nonlinear and thus cannot be described accurately by the HSC relation. Analysis of $E_g(T)$ data for three samples with $0.24 \leq x \leq 0.26$ has allowed the deduction of a new relationship for $E_g(x,T)$ that more properly accounts for the nonlinear temperature dependence below 77 K and the linear behavior above 77 K, while still accurately describing the x dependence $E_g(x,T) = -0.302 + 1.93x + 5.35(1-2x)(10^{-4})[(-1822 + T^3)/(255.2 + T^2)] - 0.810x^2 + 0.832x^3$, for E_g in eV and T in K. This relation should apply to alloys with $0.2 < x < 0.3$. The maximum change from the HSC relation in this range is 0.004 eV for $x = 0.2$ at ~ 10 K.

I. INTRODUCTION

Infrared detectors fabricated from mercury cadmium telluride (MCT or $Hg_{1-x}Cd_xTe$) alloys are extremely important components of modern infrared systems. The primary parameter controlling the wavelength range for these intrinsic detectors is the fundamental energy gap E_g, defined as the energy difference between the conduction and valence bands. The exact value of E_g depends quite critically upon the value of the mole fraction of cadmium (x) and the lattice temperature T. Numerous studies have thus been carried out by various authors over the last two decades to determine an accurate empirical relationship $E_g(x,T)$ that properly predicts how E_g depends upon the mole fraction and the temperature.[1-11] Unfortunately, there is still considerable disagreement among the many different authors and no universally accepted relationship for $E_g(x,T)$ exists. In this paper we resolve this controversy for $0 \leq x \leq 0.3$ by using the results of two-photon magneto-optical measurements for various values of x. In addition, the nonlinear temperature dependence of E_g observed at low temperatures ($T < 77$ K) is analyzed and incorporated into a new empirical relationship for $E_g(x,T)$. We note that the 8–12 and 3–5 μm wavelength regions are very important since the majority of MCT infrared detectors are based upon material with $x \approx 0.2$ and $x \approx 0.3$.

The most frequent methods for determining the MCT energy gap are based on either detector cutoff wavelength or optical absorption cuton. However, the definition of the energy gap from these types of measurements is ambiguous. The absorption edge is not infinitely sharp because of free carrier and phonon absorption along with band tailing effects. An example of the variability of defining E_g from an optical absorption measurement is (1) using the photon energy value[2] at which $\alpha = 500\ \text{cm}^{-1}$, as opposed to (2) using the energy at the turning point where the sharply rising region of the absorption curve crosses the comparatively smooth region of intrinsic absorption (usually observed for $\alpha = 3000$–$4000\ \text{cm}^{-1}$).[9]

Photoluminescence experiments have also proven difficult to perform in the smaller band gap materials.[12] Other techniques used in the past to determine E_g involve a magnetic field: the analysis of the Hall coefficient in the intrinsic region,[8] the determination of the electron effective mass (and then a calculation of E_g from an $E(k)$ dispersion relation) by the magnetophonon effect,[13] and magneto-optical methods based upon one-photon interband methods,[4,6–16] cyclotron resonance,[17] electron spin resonance,[18] and combined- or cyclotron-phonon resonance.[19] Nonlinear optical methods using four-photon mixing[20] and two-photon absorption (TPA) techniques with a CO_2 laser[21,22] have also been successfully used to determine E_g. Recently, it has been shown that TPA methods using a CO_2 laser can be used to accurately determine E_g for samples with $0.24 \leq x \leq 0.30$ by applying external magnetic fields.[23,24]

In this paper we will (1) show how two-photon magnetoabsorption (TPMA) methods are used to determine E_g, (2) review magneto-optically obtained liquid helium temperature data which, along with our new TPMA values for E_g, are used to confirm which empirical relationship for $E_g(x,T)$ most accurately fits the data for the region $0 \leq x \leq 0.3$, and (3) present and analyze the nonlinear variation of E_g with temperature to determine a new functional

 © 1990 American Vacuum Society

relationship that can be used to describe the observed temperature nonlinearities.

II. EXPERIMENTAL WORK

The experiments reported here were carried out on single crystal, bulk grown samples (both *n*- and *p*-type) with x values ranging from ≈ 0.24 to 0.30. All samples were polished, etched, and had contacts made with pure indium. A summary of the sample properties is given in Table I. For samples #3–5, the value of x and its uncertainty were supplied by Cominco and are tied to x values determined by wet chemistry.[25] Sample #1 was supplied by Honeywell with its x value derived by infrared cutoff measurements, and sample no. 2 was supplied by Texas Instruments. For sample no. 2 we have determined x by first measuring E_g and then using an $E_g(x,T)$ relationship.[7] For the purpose of determining the x dependence of E_g, sample no. 2 was not used since x was not independently measured.

The monochromatic output of a grating tunable continuous wave (cw) CO_2 laser was focused onto a sample placed in the solenoid of a superconducting magnet capable of producing dc magnetic fields as high as 12 T (or 120 kG). The direction of propagation of the linearly polarized laser light was parallel to the magnetic field, while the samples were mounted in a transverse magnetoresistance geometry. A zero-order wave plate could be used to produce circularly polarized light. Lattice heating effects are important to eliminate since most of the sample properties are temperature dependent. This was accomplished in two ways: (1) the laser beam was mechanically chopped into 20 μs wide pulses with a low duty cycle ($<1\%$), and (2) the beam was significantly attenuated by a commercial attenuator. Photoconductivity (PC) measurements were used to detect and record the small changes in absorption due to weak two-photon magneto-optical transitions. The resulting magneto-optical spectra, obtained by boxcar-averaging techniques, were then recorded on an x–y recorder.

The sample temperature was measured using a calibrated carbon-glass resistor placed close to the sample. The accuracy of the temperature measurements is estimated to be ± 0.5 K at low temperatures and about ± 1 to 2 K at higher temperatures. The calibration constant of the superconducting magnet (tesla/amp) was verified by utilizing the Shubnikov–de Haas (SdH) effect in GaSb samples. The SdH effect is an oscillatory magnetoresistance effect which is periodic in inverse magnetic field and is observable over the entire magnetic field range of the magnet (0.3 to >12 T). Comparison of these results with those obtained with a dc electromagnet (0–2 T) calibrated with nuclear magnetic resonance techniques allowed us to establish a 1% absolute field accuracy.

TABLE I. Sample electrical properties and x values.

Sample number	n (77 K) (cm^{-3})	μ(77 K) (cm^2/Vs)	x value
1	1.4×10^{14}	1.6×10^5	0.239
2	2.8×10^{14}	1.2×10^5	0.253
3	1.0×10^{14}	7.6×10^4	0.259 ± 0.0015
4	1.4×10^{14}	6.6×10^4	0.277 ± 0.001
5	9.9×10^{11}	5.3×10^4	0.300 ± 0.0035

III. RESULTS

A. Determination of E_g by TPMA techniques

In this section of the paper we illustrate how E_g can be accurately determined from TPMA spectra. Figure 1 shows the PC response versus magnetic field for sample no. 2 for various CO_2 laser wavelengths. As pointed out previously,[23,24] the dominant TPMA structure for HgCdTe alloys consists of two peaks in the PC response caused by two-photon absorption between specific valence band Landau levels and conduction band Landau levels. The TPMA transition energies can be written

$$2\hbar\omega = E_c^{a,b}(n_c,B) - E_v^{a,b}(n_v,B), \quad (1)$$

where $\hbar\omega$ is the laser photon energy, $E_c^{a,b}(n_c,B)$ $[E_v^{a,b}(n_v,B)]$ represents the energies of the conduction band [valence band] Landau levels in different spin states a or b as calculated by a modified Pidgeon–Brown band model,[6] n is the Landau level number, and B is the magnetic field. Polarization studies show that the two peaks arise for the left circularly polarized TPMA transitions $a^+(-1)\rightarrow a^c(1)$ [L_1 transition, at highest fields and $n_v=-1$, $n_c=+1$] and $b^+(-1)\rightarrow b^c(1)$ [L_2 transition], where the plus sign

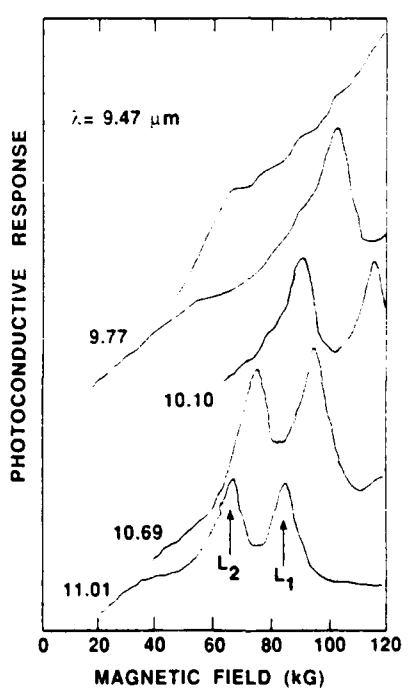

FIG. 1. Photoconductive response of sample no. 2 ($x=0.253$) for various CO_2 laser wavelengths at 7 K. The two large broad peaks, identified as L_1 and L_2, arise from resonant two-photon absorption processes identified in the text.

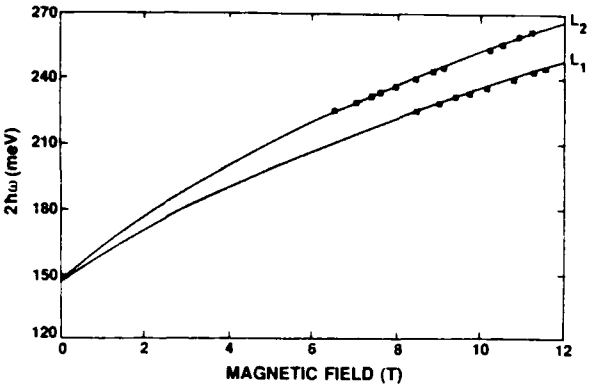

FIG. 2. Two-photon transition energies vs magnetic field for sample no. 2. The solid lines represent the best fit of the transition energies calculated from Eq. (1) to the data giving $E_g = 146.5$ meV ± 1.0 meV. The data points are restricted by the $2\hbar\omega$ values that can be obtained from the CO_2 laser. $T = 7$ K.

refers to light hole Landau levels. Note that as $B \to 0$, $2\hbar\omega \to E_g$.

Figure 2 shows a plot of the experimental data shown in Fig. 1 of the values of $2\hbar\omega$ versus resonant B field. Theoretical results for the dependence of $2\hbar\omega$ on B are calculated from Eq. 1 by using a modified Pidgeon–Brown energy band model.[6] The Landau level energies were calculated by using Weiler's set of band parameters[6]: $E_p = 19$ eV, $\Delta = 1$ eV, $\gamma_1 = 3.3$, $\gamma_2 = 0.1$, $\gamma_3 = 0.9$, $\kappa = -0.8$, $F = -0.8$, $q = 0.0$, and $N_1 = 0.0$. The value of E_g is then easily determined by fitting the theoretical calculations to the data with E_g as an adjustable parameter. The result for sample no. 2 is $E_g = 146.5 \pm 1.0$ meV at $T = 7$ K. These two-photon magneto-optical techniques are the best method for accurately determining the energy gap of a semiconductor in part because resonant optical absorption processes occur between Landau levels. One key advantage of TPMA is that it takes place in the bulk of the sample and is thus much less sensitive to surface preparation than one-photon techniques.

In addition, exciton corrections are much smaller for TPMA than for one-photon absorption and thus do not significantly impact the observed transitions. We note that although samples no. 3–5 are compensated, TPMA effects can still be easily observed and thus used to determine accurate values for E_g.

B. Dependence of $E_g(x,T)$ on x value (for $0<x<0.3$)

A number[1-11] of $E_g(x,T)$ relationships exist in the literature and various researchers use different ones in their day-to-day applications. No consensus exists as to which actually describes the real variation of E_g with x. In this section we show that our TPMA-derived E_g values verify the Hansen, Schmit, and Casselman (HSC)[7] relationship for $E_g(x,T)$ $(0<x<0.3)$. We also review various $E_g(x,T)$ relationships[5-7,9,10] and the magneto-optical data[15,16,18-20,26] that can be used as a basis to derive the $E_g(x,T)$ dependence. Magneto-optical studies have proven capable of accurately determining energy band parameters (e.g., E_g values) of semiconductors because of the resonant optical transitions that occur between magnetically quantitized electronic states. For this reason we concentrate on magneto-optical determinations of E_g. We note that our calculations of the two-photon transition energies show negligible dependence on the crystallographic orientation of the magnetic field direction because of the particular set of band parameters that describe MCT. Unoriented samples can thus be used because anisotropic effects need not be considered.

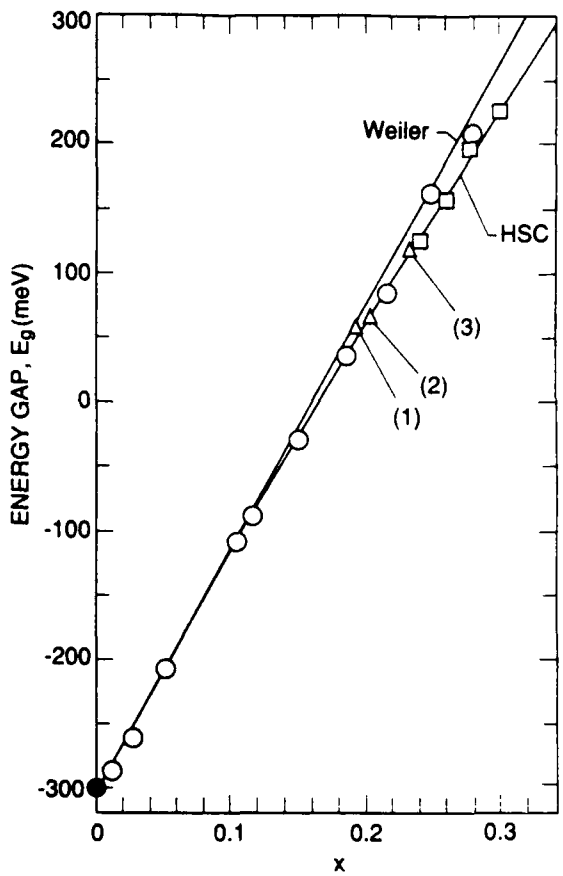

FIG. 3. The low-temperature (≈ 4 K) x dependence of the energy gap for alloys with $0<x<0.3$ selected magneto-optical data are presented as identified by the various symbols. The two solid lines represent extremes of the published $E_g(x,T)$ relationship: Weiler (Ref. 6) and HSC (Ref. 7). ● Ref. 26, IMA; ○ Refs. 15, 16, IMA; △ (1) Ref. 18 ESR; △ (2) Ref. 19, CCCPR; △ (3) Ref. 20, four photon mixing (ESR); □ present work, TPMA.

Figure 3 shows a plot of $E_g(x,T)$ for several sets of magneto-optically derived E_g values for very low temperatures (<10 K),[15,16,18-20,26] along with our TPMA-deduced values of E_g. Table II gives the values of E_g and x used in the graphs of Figs. 3 and 4 along with the magneto-optical technique used to obtain them. To the authors' knowledge, these are the most reliable data to use. The variations of two empirical relationships that represent the most extreme behavior are also shown in Fig. 3 by the solid lines (Weiler's[6] and the HSC relationship[7]). It is immediately clear that the biggest differ-

TABLE II. Low temperature magneto-optical derived values of $E_g(x)$. Various magneto-optical techniques used include (1) IMA—interband magnetoabsorption, (2) ESR—electron spin resonance, (3) CCCPR—cyclotron, combined and cyclotron phonon resonances, (4) four-photon mixing, and (5) TPMA—two-photon magnetoabsorption. These values are used in Fig. 3 and/or Fig. 4.

x value	E_g (meV)	Magneto-optical technique used	Reference	Comments
0	-299.7 ± 0.5	IMA	26	at 8 K
0.01	-285	IMA	15,16	at 4 K
0.025	-261			
0.05	-207			
0.105	-110			
0.115	-90			
0.15	-30			
0.185	35			
0.215	86			
0.25	161			
0.28	208			
0.193	56	ESR	18	at 4 K
0.203	64 ± 3	CCCPR	19	at 4 K
0.234	119	Four-photon mixing (ESR)	20	at 4 K
0.239	122 ± 1	TPMA	present work	at 2–10 K
0.259 ± 0.0015	158.5 ± 1			
0.277 ± 0.001	195 ± 1			
0.300 ± 0.0035	224 ± 2			

ences in these two relationships occur in the 0.2–0.3 x-value region. Thus, in order to test which relationship is most accurate, we replot the magneto-optical data in the range 0.2–0.3 in Fig. 4. For completeness we also include the variations of three additional empirical relationships that have also been reported in the literature: Nemirovsky and Finkman (NF),[5] Chu, Xu, and Tang (CXT),[9] and Legros and Triboulet (LT).[10] In addition we have added two values from the recent EMIS Datareviews Series No. 3.[11] The Schmit and Stelzer[3] relationship was not included because the low value of E_g (-250 meV) obtained from it at $x = 0$ is in major disagreement with the low x-value MCT data of Guldner *et al.*[15,16] and the HgTe results from Dobrowolska *et al.*[26] The extremely wide variation in predicted E_g values from these relationships is apparent. The important observation to note is that the present TPMA work verifies the use of the HSC relationship as representing the best value of $E_g(x,T)$ in the range 0.0–0.3 at very low temperatures (< 10 K). Unless the good fit is fortuitous, it implies the validity of the gap determination using detector cutoff energy and $\alpha = 500\ \mathrm{cm}^{-1}$ absorption edge data.

C. Dependence of E_g on T (for $0.24 < x < 0.26$)

Most workers have ignored the fact the $E_g(T)$ should vary nonlinearly with T at low temperatures (see the thermodynamic arguments presented later). Accurate low temperature $E_g(T)$ data simply did not exist. Now, however, the accuracy of determining $E_g(T)$ by TPMA techniques allows an empirical expression for $E_g(T)$ to be determined. Figure 5 shows how the TPMA spectra obtained at $\lambda = 10.24\ \mu\mathrm{m}$ depend upon lattice temperature T. A shift in magnetic field positions of the resonant L_1 and L_2 structure is seen to be small for $T < 15$ K, but quite noticeable for $T > 15$ K. The shift of the resonant structure to lower magnetic fields for increasing temperatures is a direct consequence of the increasing energy gap, since as E_g becomes larger, the valence and conduction band Landau levels become further apart in energy. Thus, smaller values of magnetic field are required to meet the TPMA resonant condition for a given two-photon energy. At each temperature, multiple wavelengths were then used to determine values of E_g in the manner described in Sec. III A.

We propose to replace the linear temperature term T in the HSC relation by the term $(A + T^3)/(B + T^2)$. This functional relationship agrees with the HSC relationship at high temperatures, while allowing for an offset from the HSC relationship at 0 K. It also agrees with the fact that $dE_g/dT = 0$ at 0 K. The size of the 0 K offset is determined by A/B, while the temperature above which agreement with HSC occurs is determined from the inequalities $T \gg \sqrt[3]{A}$ and $T \gg \sqrt{B}$.

We have simultaneously fitted a composite of three sets of E_g versus T data for the samples with $x = 0.239$, $x = 0.253$,

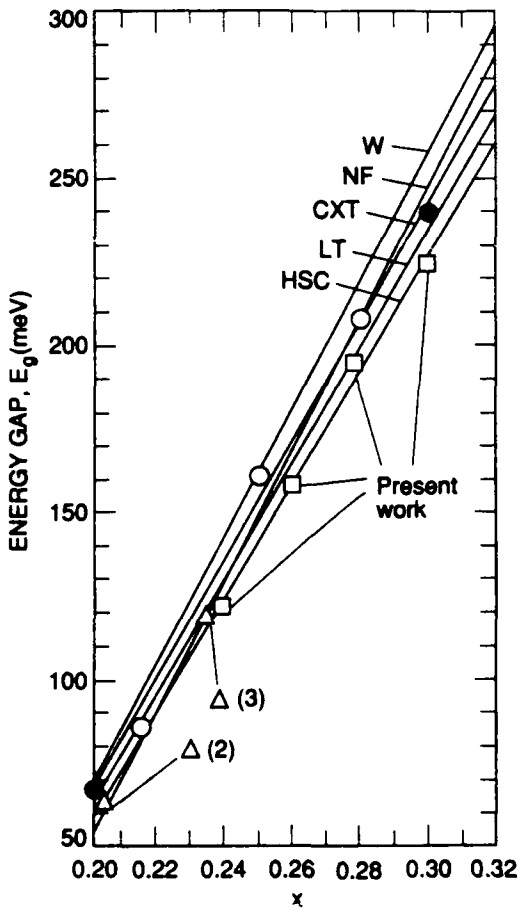

FIG. 4. The low-temperature (≈ 4 K) x-dependence of the energy gap for $0.2 < x < 0.3$. This is the most technologically interesting region for infrared detectors and is the region where the various $E_g(x,T)$ relationships differ the most. Again, various magneto-optical data are presented as well as the numbers given in the recent EMIS Datareviews Series (Ref. 11). The solid lines represent various published relationships describing $E_g(x,T)$: W (Ref. 6), NF (Ref. 5), CXT (Ref. 9), LT (Ref. 10), and HSC (Ref. 7). Note that the TPMA data from the present work agrees best with the HSC relationship. ○ Refs. 15 and 16; ● EMIS Datareviews Series no. 3 (1987).

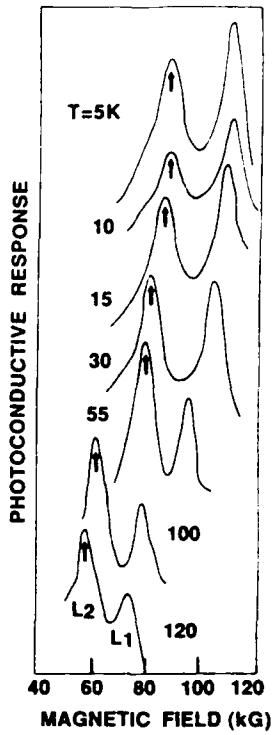

FIG. 5. Temperature dependence of the photoconductive TPMA spectra for sample no. 2. Note the (1) TPMA structure can clearly be seen up to 120 K and beyond, and (2) the peaks do not shift with temperature from 5 to 10 K. $\lambda = 10.24\ \mu$m.

and $x = 0.259$ by the nonlinearly least squares routine contained in DATAPLOT.[27] The first and third values were obtained from Cominco, while the second was chosen to be consistent with the HSC relationship at high temperatures.

Our data merge smoothly with the HSC relationship above 100 K. Below 100 K the data lie below the HSC relationship, and become constant before 10 K. Figure 6 shows the composite data rationalized for comparison by subtracting the 0 K energy gap obtained from HSC and dividing by $0.535(1-2x)$. Rationalized HSC values are used at high temperature so that a fit was obtained between 0 and 300 K. The constants A and B that best fit all the data are: $A = -1822$ K^3 and $B = 255.2$ K^2. Although A and B can vary with x, no trend was observed by fitting the data individually for each sample, and thus we obtain the A and B values which best fit all the data. The offsets between our fit and HSC at 0 K are on the order of 2 meV, which is comparable to the value implied by the uncertainty in x values. Even though at 0 K the offsets are small, the differences predicted by our new relationship and associated with the nonlinear temperature dependence of E_g are on the order of 3–4 meV at 10–12 K and should be taken into account in experiments requiring high accuracy.

Figures 7(a)–(c) show the data for the energy gap as a function of temperature for each sample along with the result of the composite fit. In each case the fit is adequate relative to the ± 2 meV uncertainty that arises mainly from the uncertainty in x. Figure 8(a) shows dE_g/dT, rationalized as in Fig. 6, determined from the data as well as the fit (represented by the line). It is seen that dE_g/dT rises rapidly at low temperatures, reaches a peak at 10–12 K, and then becomes asymptotic to that of HSC. A peak was predicted by Popko and Pawlikowski[28] from the dilatational part of the temperature dependence of the energy gap. We have revised their calculations by using more recent data obtained by Caporaletti and Graham[29] for the thermal expansion coefficient of $Hg_{1-x}Cd_xTe$ alloys. We have obtained the value for $x = 0.25$ alloys by averaging the values obtained at 0.20 and 0.30 in Ref. 29. The 25% rise in dE_g/dT above unity at 10–12 K seen in Fig. 8(a) is found to agree numerically when the new expansion coefficient value is used in the formula of Ref. 28. Figure 8(b) shows the difference between our new

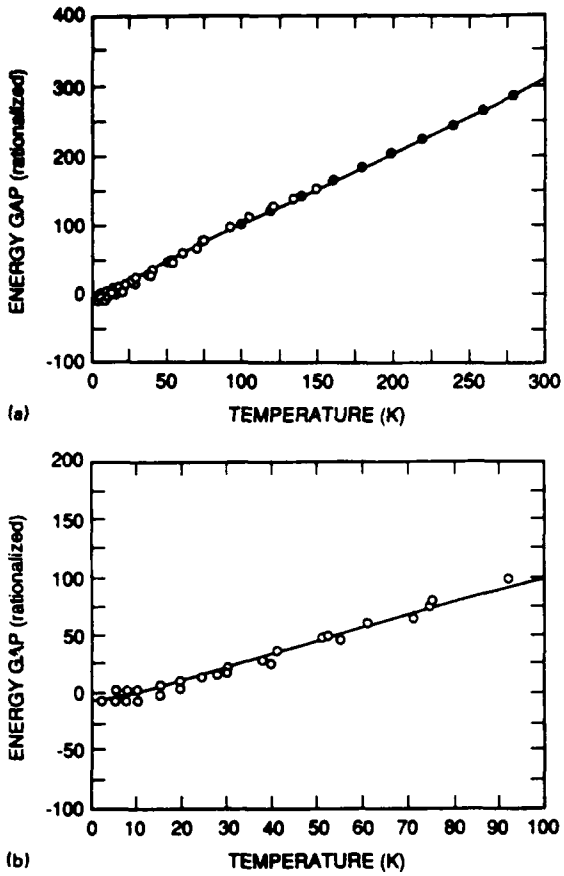

FIG. 6. (a) Rationalized energy gaps as a function of temperature for (○) samples nos. 1 ($x = 0.239$), 2 ($x = 0.253$), and 3 ($x = 0.259$); (●) with HSC at high temp and fit. Rationalized values from HSC are used at temperatures above those reached by the data. Fit by the expression $(A + T^3)/(B + T^2)$ is the solid line. (b) An expansion of (a) between 0 and 100 K. Sample nos. 1–3 and fit.

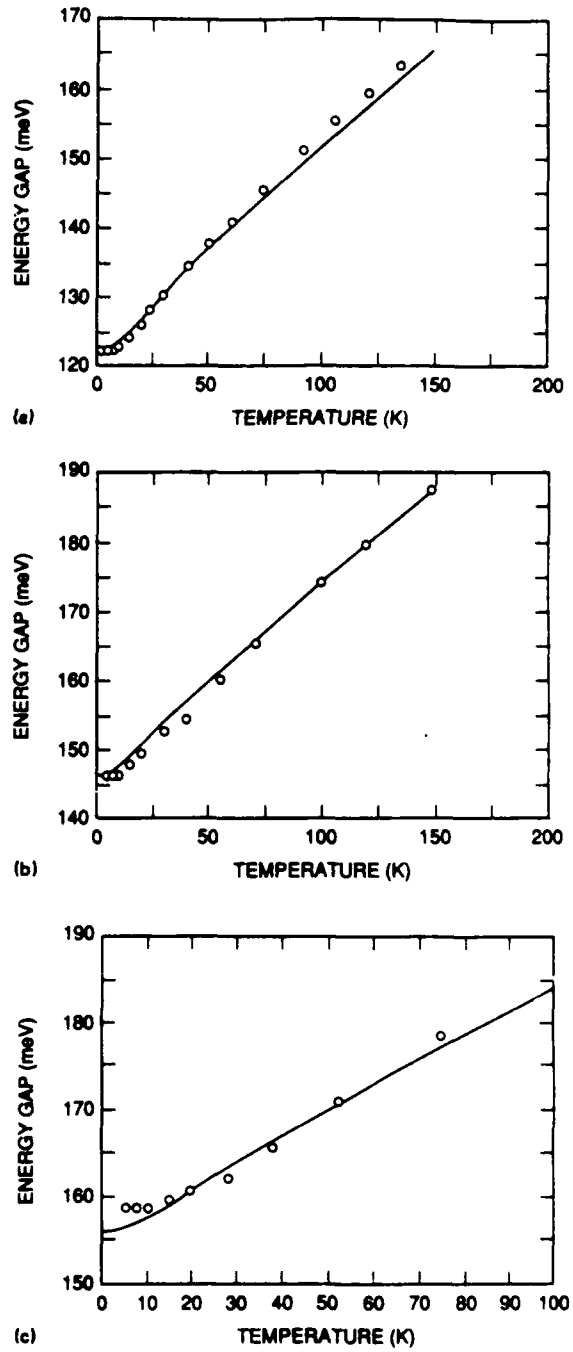

FIG. 7. (a) Energy gaps of sample #1 ($x = 0.239$) as a function of temperature. The fit by our new relationship is the solid line. (b) Same as (a) for sample no. 2 ($x = 0.253$). (c) Same as (a) for sample no. 3 ($x = 0.259$).

relationship and that of HSC as a function of temperature for $x = 0.2$, 0.25, and 0.3. The difference peaks near 10–12 K and becomes negligible above 100 K for each curve.

According to the laws of thermodynamics discussed by Thurmond,[30] the forbidden energy gap, ΔE_{cv}, is the standard Gibbs energy for formation of electrons and holes as a function of temperature. The temperature dependence of ΔE_{cv} may be found from the standard thermodynamic relations[31]:

$$\begin{aligned} d(\Delta E_{cv}) &= d(\Delta H_{cv}) - Td(\Delta S_{cv}) - dT(\Delta S_{cv}) \\ &= Td(\Delta S_{cv}) + (\Delta V_{cv})dp - Td(\Delta S_{cv}) \\ &\quad - dT(\Delta S_{cv}) \\ &= (\Delta V_{cv})dp - dT(\Delta S_{cv}), \end{aligned}$$

$$d(\Delta E_{cv})/dT = -\Delta S_{cv} \text{ if } dp = 0 \text{ (fixed pressure)}$$

where ΔH_{cv} is the enthalpy of formation, ΔS_{cv} is the entropy of formation, ΔV_{cv} is the volume change, T is temperature, and p is pressure. By the third law of thermodynamics, $\Delta S_{cv} \to 0$ as $T \to 0$, so that $d(\Delta E_{cv})/dT \to 0$ as $T \to 0$. The entropy in this case goes to zero physically because all valence states become filled and all conduction states become empty. It is mathematically satisfying that the derivative becomes zero because there is no temperature below absolute zero,

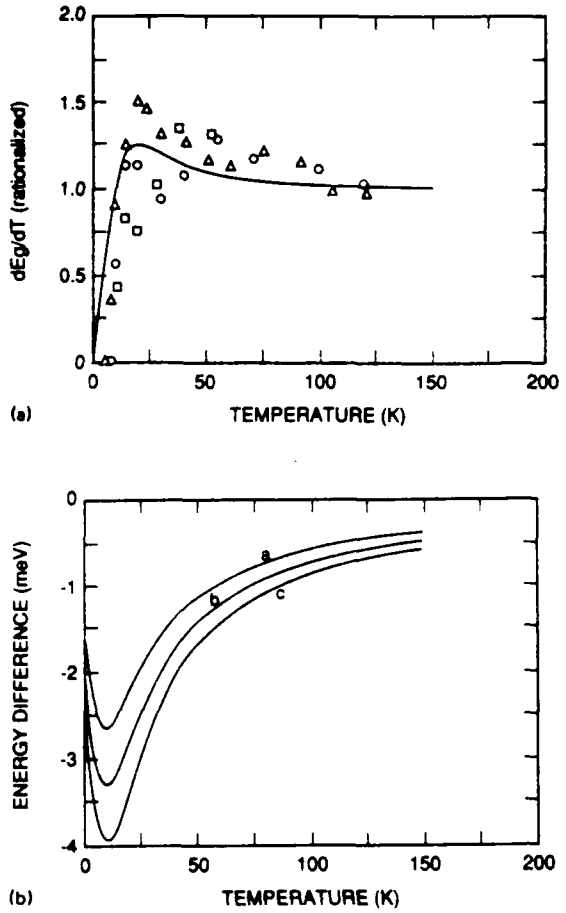

FIG. 8. (a) Rationalized derivative of the energy gap with temperature as a function of temperature for the data of samples nos. 1 (△), 2 (○), and 3 (□) ($x = 0.239$, 0.253, and 0.259) along with that corresponding to the fit, $(A + T^3)/(B + T^2)$. (b) Difference in energy between our relation and HSC as a function of temperature for $x =$ (a) 0.3, (b) 0.25, and (c) 0.2.

which would be needed in the definition of the derivative if it were finite.

IV. SUMMARY AND CONCLUSIONS

Accurate determinations of the energy gap by two-photon magnetoabsorption techniques at liquid helium temperatures in alloys of $0.24 < x < 0.30$ have been made. They are shown to help verify the use of the Hansen–Schmit–Casselman relation, one of many existing, over the range $0 < x < 0.30$ at these temperatures. In contrast, the observed temperature dependence is nonlinear and thus cannot be described accurately (better than 3–4 meV) by the HSC relation below 77 K. Analysis of $E_g(T)$ data for three samples with $0.24 < x < 0.26$ has allowed the deduction of a new relationship for $E_g(x,T)$ that more properly accounts for the nonlinear temperature dependence below 77 K and the nearly linear behavior above 77 K

$$E_g(x,T) = -0.302 + 1.93x + 5.35(1-2x)(10^{-4}) \times [(-1822 + T^3)/(255.2 + T^2)] - 0.810x^2 + 0.832x^3,$$

for E_g in eV and T in K.

This relation should apply to alloys with $0.2 < x < 0.3$.

For samples with 10 μm cutoff wavelengths (i.e., $x \approx 0.2$), the maximum deviation of our new relation from that of HSC is approximately 3–4 meV at ~10–12 K. At lower temperatures, E_g becomes independent of T and for higher temperatures the difference grows smaller, finally becoming negligible at temperatures over 100 K. The major reason for the observed nonlinear behavior of E_g seems to be related to (1) the dilatational part of E_g as predicted earlier by Popko and Pawlikowski and (2) the fact that dE_g/dT must go to zero at $T = 0$ K as predicted by the third law of thermodynamics.

The work in this paper on the nonlinear temperature dependence of E_g at $T < 77$ K is also significant because it provides valuable input for the proper interpretation of low temperature photoluminescence (PL) spectra. For example, low temperature PL spectra for alloys with $x \approx 0.3$ are often composed of multiple lines attributed to recombination originating from band-to-band, band-to-acceptor, donor-to-acceptor, and/or bound exciton transitions.[12,32,33] The identification and interpretation of each particular PL line is usually made by determining the variation in intensity of the line with pump power and the shift in the line energy with lattice temperature. The energy of the PL lines usually shift with temperature and those shifts are then compared with the shifts in band gap energy with temperature. Consequently, accurate knowledge of the nonlinear temperature variation of E_g for $T < 77$ K is important.

ACKNOWLEDGMENTS

We acknowledge the partial support of this work at UNT by the U.S. Army Center for Night Vision and Electro-Optics, Contract No. DAA B07-87-C-F094. Regarding Cominco, Honeywell, and Texas Instruments, reference to material obtained is included for completeness of exposition and constitutes neither an endorsement by NIST nor representation that the material referenced is the best available for the purpose.

[1] J. D. Wiley and R.N. Dexter, Phys. Rev. **181**, 1181 (1969).
[2] M. W. Scott, J. Appl. Phys. **40**, 4077 (1969).
[3] J. L. Schmit and E. L. Stelzer, J. Appl. Phys. **40**, 4865 (1969)
[4] M. H. Weiler, R. L. Aggarwal, and B. Lax, Phys. Rev. B **16**, 3603 (1977)
[5] Y. Nemirovsky and E. Finkman, J. Appl. Phys. **50**, 8107 (1979).
[6] M. H. Weiler, in *Semiconductor and Semimetals*, edited by R. K. Willardson and A. C. Beer (Academic, New York, 1981) Vol. 16, p. 119.
[7] G. L. Hansen, J. L. Schmit, and T. N. Casselman, J. Appl. Phys. **53**, 7099 (1982).
[8] E. Finkman, J. Appl. Phys. **54**, 1883 (1983).
[9] J. Chu, S. Xu, and D. Tang, Appl. Phys. Lett. **43**, 1064 (1983).
[10] R. Legros and R. Triboulet, J. Crystal Growth **72**, 264 (1985).
[11] J. C. Brice, in *EMIS Datareviews Series*, No. 3 (INSPEC, London, 1987), p. 103.
[12] See, for example, A. T. Hunter and T. C. McGill, J. Appl. Phys. **52**, 5779 (1981).

[13]See, for example, S. W. McClure, D. G. Seiler, C. L. Littler, and M. W. Goodwin, J. Vac. Sci. Technol. A **3**, 271 (1985).
[14]S. H. Groves, T. C. Harman, and C. R. Pidgeon, Solid State Commun. **9**, 451 (1971).
[15]Y. Guldner, C. Rigaux, A. Mycielski, and Y. Couder, Phys. Status Solidi B **81**, 615 (1977).
[16]Y. Guldner, C. Rigaux, A. Mycielski, and Y. Couder, Phys. Status Solidi B **82**, 149 (1977).
[17]T. O. Poehler and J. R. Apel, Phys. Lett. **32A**, 268 (1970).
[18]B. D. McCombe, R. J. Wagner, and G. A. Prinz, Phys. Rev. Lett. **25**, 87 (1970).
[19]B. D. McCombe, R. J. Wagner, and G. A. Prinz, Solid State Commun. **8**, 1687 (1970).
[20]T. J. Bridges, E. G. Burkhardt, and V. T. Nguyen, Optics Commun. **30**, 66 (1979).
[21]D. G. Seiler, S. W. McClure, R. J. Justice, M. R. Loloee, and D. A. Nelson, Appl. Phys. Lett. **48**, 1159 (1986).
[22]D. G. Seiler, S. W. McClure, R. J. Justice, M. R. Loloee, and D. A. Nelson, J. Vac. Sci. Technol. A **4**, 2034 (1986).
[23]D. G. Seiler, C. L. Littler, M. R. Loloee, and S. A. Milazzo, J. Vac. Sci. Technol. A **7**, 370 (1989).
[24]D. G. Seiler, M. R. Loloee, S. A. Milazzo, A. J. Durkin, and C. L. Littler, Solid State Commun. **69**, 757 (1989).
[25]W. F. H. Micklethwaite, J. Appl. Phys. **63**, 2382 (1988).
[26]M. Dobrowolska, A. Mycielski, and W. Dobrowolski, Solid State Commun. **27**, 1233 (1978).
[27]DATAPLOT is a software package developed at NIST (formerly NBS) for analyzing and displaying data; see DATAPLOT—*Introduction and Overview*, NBS Special Publication 667 (U.S. GPO, Washington, D. C., 1984).
[28]E. Popko and J. M. Pawlikowski, Phys. Status Solidi A **46**, K9 (1978).
[29]O. Caporaletti and G. M. Graham, Appl. Phys. Lett. **39**, 338 (1981).
[30]C. D. Thurmond, J. Electrochem. Soc. **122**, 1133 (1975).
[31]J. Reif, in *Fundamentals of Statistical and Thermal Physics* (McGraw-Hill, New York, 1965).
[32]A. T. Hunter, D. L. Smith, and T. C. McGill, Appl. Phys. Lett. **37**, 200 (1980).
[33]B. L. Gel'mont, V.I. Ivanov-Omskii, V.A. Mal'tseva, and V.A. Smirnov, Sov. Phys. Semicond. **15**, 638 (1981).